Air Force Institute of Technology

AFIT Scholar

6-8-2006

Blind Deconvolution of Anisoplanatic Images Collected by a Partially Coherent Imaging System

Adam MacDonald

Follow this and additional works at: https://scholar.afit.edu/etd

Part of the Signal Processing Commons

Recommended Citation

BLIND DECONVOLUTION OF ANISOPLANATIC IMAGES COLLECTED BY

A PARTIALLY COHERENT IMAGING SYSTEM

DISSERTATION
Adam MacDonald
Lt Col, USAF

AFIT/DS/ENG/06-04

DEPARTMENT OF THE AIR FORCE

AIR UNIVERSITY

AIR FORCE INSTITUTE OF TECHNOLOGY

Wright-Patterson Air Force Base, Ohio

AFIT/DS/ENG/06-04

BLIND DECONVOLUTION OF ANISOPLANATIC IMAGES COLLECTED BY A PARTIALLY COHERENT IMAGING SYSTEM

DISSERTATION

Presented to the Faculty

Graduate School of Engineering and Management

Air Force Institute of Technology

Air University

Air Education and Training Command

In Partial Fulfillment of the Requirements for the

Degree of Doctor of Philosophy

Adam MacDonald, B.S.E.E., M.S.E.E.
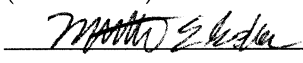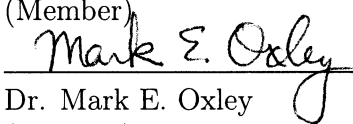
Lt Col, USAF

June 2006
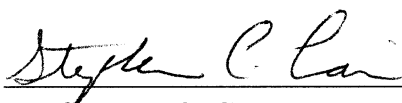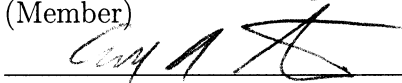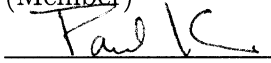
BLIND DECONVOLUTION OF ANISOPLANATIC IMAGES COLLECTED BY A PARTIALLY COHERENT IMAGING SYSTEM

DISSERTATION

Adam MacDonald, B.S.E.E., M.S.E.E.

Lt Col, USAF

Approved:

_____   _____
Dr. Stephen C. Cain   5 June 06
(Chairman)   Date

_____   _____
Lt. Col. Matthew E. Goda   5 JUN 06
(Member)   Date

_____   _____
Dr. Mark E. Oxley   5 Jun 06
(Member)   Date

_____   _____
Dr. Edward A. Watson   5 Jun 06
(Member)   Date

_____   _____
Dr. Paul I. King   6 Jun 06
(Dean's Representative)   Date

Accepted:

_____   _____
Dr. M. U. Thomas   8 Jun 06
Date

Dean, Graduate School of Engineering and Management

AFIT/DS/ENG/06-04

Abstract

Coherent imaging systems offer unique benefits to system operators in terms of resolving power, range gating, selective illumination and utility for applications where passively illuminated targets have limited emissivity or reflectivity. In contrast to incoherent imaging systems, partially coherent illumination causes difficulty during image processing due to high levels of image speckle caused by constructive and destructive interference effects unique to the highly coherent illumination source. Image speckle is caused by the random phase delays that occur due to target roughness and the turbulent atmosphere between the remote target and optical system. To combat such effects, a number of short-exposure images are combined by incoherent averaging to arrive at an image that has greatly decreased levels of speckle. Unfortunately, such average images suffer from decreased spatial resolution due to blur resulting from atmospheric distortion.

Effective image restoration may be realized by inverse filtering the recovered average image with an optical transfer function that describes the overall optical system and atmospheric turbulence. In cases where it is inconvenient or impossible to measure the parameters of this evolving function, blind deconvolution algorithms may be applied to estimate both the unknown remote scene reflectance, as well as the unknown system transfer function. This research proposes a novel blind deconvolution algorithm that is based on a maximum *a posteriori* Bayesian estimator constructed upon a physically-based statistical model for the intensity of the partially coherent light at the imaging detector. The estimator is initially constructed using a shift-invariant system model, and is later extended to the case of a shift-variant optical system by the addition of a transfer function term that quantifies optical blur for given field-of-views and atmospheric conditions. The estimators are evaluated using both synthetically generated imagery, as well as experimentally collected image data from an outdoor optical range.

The research is extended to consider the effects of weighted frame averaging for the individual short-exposure frames collected by the imaging system. Atmospheric distortion and laser speckle effects create difficult challenges for image registration algorithms. In addition, anisoplanatic image warping can cause individual frames to fit poorly to the aggregate frame ensemble. A system is devised where such frames are automatically identified for removal from the average image, and the resulting frame average is compared to the unweighted average. Results are presented to support the new algorithm using both simulated and experimentally collected data.

Acknowledgements

The road to knowledge is littered with obstacles. Many of these are self-imposed, while others arise from nature due to the subject matter under study. Many people have helped me overcome the most stubborn of these impediments. I certainly owe a debt of gratitude to the hardworking folks at the Air Force Research Laboratory, who took the time to carefully collect the experimental data used to reach many of my conclusions in this research. Dr. Steve Cain was a superb advisor and mentor, keeping me focused and motivated to see the fruits of my labors. I'd also like to thank the leadership of the Air Force Institute of Technology for allowing me to spend time on research, rather than the endless details that might otherwise accompany a military officer attending an academic institution. Finally, but certainly most importantly, I thank my loving and kind wife and my two beautiful and creative daughters for their constant support of my thirst for knowledge.

"I often say that when you can measure what you are speaking about, and express it in numbers, you know something about it; but when you cannot express it in numbers, your knowledge is of a meagre and unsatisfactory kind..." Lord W. Kelvin

Adam MacDonald

Table of Contents

List of Figures

List of Tables

List of Abbreviations

BLIND DECONVOLUTION OF ANISOPLANATIC IMAGES COLLECTED BY A PARTIALLY COHERENT IMAGING SYSTEM

I. Introduction

The central focus of this research is to explore the challenging problem of image reconstruction of coherently formed images viewed by an optical system with a field-of-view that often exceeds the isoplanatic viewing angle. The purpose of this chapter is to provide a brief introduction to the field of image reconstruction by way of blind image deconvolution of images obtained through a turbulent atmosphere, and to explain the particular difficulties encountered with systems that approach or exceed the isoplanatic angle.

1.1   Speckle Imaging Through Turbulence

Researchers have shown significant interest towards the general problem of obtaining accurate image estimates of a remotely viewed scene viewed with an optical system imaging though atmospheric turbulence. A significant body of turbulent imaging research has been generated by the astronomical community, e.g. [49, 77]. The images obtained through these optical systems are distorted by several effects. The optical distortions introduced by the telescope components are fixed and relatively easy to quantify. A dramatically more difficult problem is the distortion induced by the random condition of the atmosphere between the telescope and the distant star or planet. Additionally, there may be distortion in the image caused by vibration or motion of the telescope during the integration period over which the image is captured.

Scientists and engineers often seek to deduce the degradation of the imaged scene due to the effects of a turbulent atmosphere. In the case of stellar imaging, the light from extremely distant stars travels undistorted through many light-years of the vacuum of space prior to reaching the Earth's atmosphere. There, pockets

of turbulent eddies of air with varying indices of refraction introduce random phase delays on different portions of the approaching optical plane wave. The net effect is a randomly distorted *speckle image* formed by the constructive and destructive combination of the distorted phase fronts. The effects of this distortion vary dramatically in relation to the length of time allowed for image capture. Long exposure times tend to average the effects of the phase and amplitude variations to produce a blurred image. In this case, the average Optical Transfer Function (OTF) can be described as a low-pass filter, with a cutoff frequency dependent on the severity of the atmospheric turbulence. However, by reducing the exposure time to a period short enough to essentially freeze the motion of the turbulent media through which the plane wave must pass, a dramatically different effect is noted. In such cases, the phase and amplitude distortions of the entire optical path through the atmosphere tend to produce what has come to be known as a speckle image. Figure 1.1 shows a simulated image of a diffraction-limited point source as viewed through the vacuum of space without the effects of a turbulent atmosphere. Figure 1.2 shows the same point viewed over the course of a long integration period of time through turbulent atmosphere. The result is a symmetrically broadened image, and the optical system can essentially be regarded as having a low-pass OTF or broad Point Spread Function (PSF). In contrast, Figure 1.3 shows a simulated image of the same point source as viewed through identical turbulence as in Fig. 1.2. However, this image was obtained over an integration period short enough to capture the instantaneous structure of the phase and amplitude distortions of the turbulent media. The image of Fig. 1.3 clearly contains higher spatial frequency information than that of Fig. 1.2. Also notable is the global shift of the image intensity, often referred to as *image tilt* that results from relatively large linear phase distortion components.

The overall average system OTF may be regarded as the composition of the individual OTFs that arise from the fixed (possibly aberrated) optical system, the turbulent atmosphere for a given exposure time, and the vibration or motion experienced by the optical system over the same exposure period. For the simple case of a
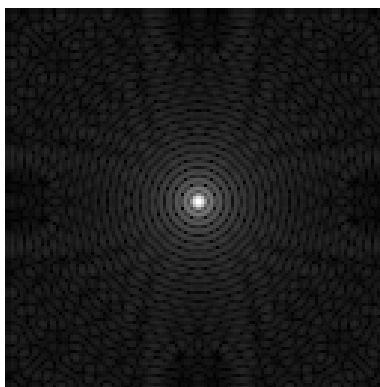
Figure 1.1:   Diffraction limited point source image.
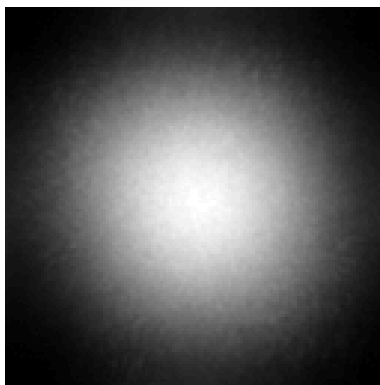
Figure 1.2:   Long exposure average point source image.
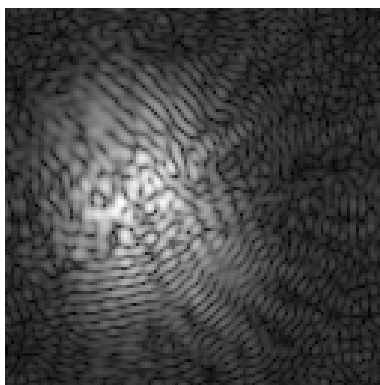
Figure 1.3:   Short exposure instantaneous point source image.

Linear Shift-Invariant (LSI) system, the ensemble average system OTF, $\overline{\mathcal{H}}_{sys}$ can be expressed as the product of the component OTFs,

$$\overline{\mathcal{H}}_{sys}(u,v) = \mathcal{H}_{opt}(u,v)\overline{\mathcal{H}}_{turb}(u,v)\overline{\mathcal{H}}_{reg}(u,v) \qquad (1.1)$$

where $\mathcal{H}_{opt}(u,v)$ is the non-random OTF due to the design of the optical system, $\overline{\mathcal{H}}_{turb}(u,v)$ is the statistically averaged OTF due to the turbulent atmosphere over some fixed integration time, and $\overline{\mathcal{H}}_{reg}(u,v)$ may be thought of as the OTF formed by the combination of registration errors in the image arising from vibration and other linear motion components not produced by the atmosphere. Finally, u and v are variables in the spatial frequency domain of the image space. It is important to note that approximately 87% of the distortion caused by atmospheric turbulence results in linear phase plane *tip* and *tilt*, the effects of which might be indistinguishable from translational motion caused by sensor platform motion and vibration.

1.2   *Blind Deconvolution for Image Reconstruction*

In stark contrast to conventional deconvolution, where accurate knowledge of the system OTF and thus PSF exists, the problem of blind deconvolution assumes that the overall transfer function of the system is unknown. If the system is LSI, then the image formation process may be modeled as

$$d(x,y) = o(x,y) \otimes h(x,y) + n(x,y) \qquad (1.2)$$

where o represents the true remote scene to be estimated, h is the PSF of the overall system, n is additive noise, d is the image captured by the system, and $\otimes$ represents convolution in two dimensions. The variables x and y represent spatial coordinates in the image plane. In many imaging applications, the noise is accurately modeled as signal dependent, often distributed as a Poisson random variable. Despite signal dependence, the noise process may be represented as an additive quantity to each pixel of a formed image [4].

The image model given in Eqn. 1.2 may be strictly applied only to individual frames collected by the imaging system. Many reasons might exist where the system operator requires more than a single frame to form a useful image. For distant remote scenes, low signal levels might require the summation of several image frames to increase the Signal-to-Noise Ratio (SNR). Additionally, coherent fields passing through a turbulent atmosphere often suffer from an objectionable degree of speckle noise due to the constructive and destructive summation of random phase fronts from individual point sources that comprise the remote scene. As demonstrated in Fig. 1.2, the incoherent summation of some quantity of these speckle images results in a less chaotic image, albeit with dramatic attenuation in high spatial frequency detail. For these compelling reasons, some form of image averaging is typically necessary to produce a useable image for the system operator.

This research focuses on remote scenes illuminated by coherent light sources, typified by some realization of a high peak power pulsed laser system. The incoherent summation of many coherent frames results in an optical system that may be effectively modeled as a linear system, thus permitting the inherently linear deconvolution operation in later steps of image processing.

If $h(x, y)$ is well understood and parameterized, the unknown image $o(x, y)$ may be estimated using established methods such as Wiener filtering [10], inverse filtering, recursive Kalman filtering, least-squares filtering, and constrained iterative deconvolution methods [41]. However, in many cases of interest, $h(x, y)$ is also unknown, leading to the body of techniques generally referred to as blind image deconvolution.

The field of blind image deconvolution is well established in the literature [4, 13, 14, 20, 21, 37, 43, 46, 48–51, 56, 64–66, 73, 76]. Other common terms describing the technique include *blind image restoration* and *blind image recovery*. A detailed pair of excellent survey articles on the topic describes the most promising techniques used by image processing researchers [41, 42]. The underlying assumption of this body of knowledge is that of linearity and shift-invariance of the overall optical system. The

problem of linearity was briefly introduced above and is not considered a significant issue given a collection of incoherently averaged short-exposure image frames. The problem of shift invariance becomes apparent when the optical field of view begins to exceed certain proportions, and is discussed in greater detail in the following section.

1.3 Isoplanatic vs. Anisoplanatic Imaging

Section 1.2 presupposes some very important and limiting properties of the optical system used to capture the images. Most importantly, an optical imaging system may only be modeled using the convolution operation described by Eqn. 1.2 if it can be shown that the optical system is linear and spatially invariant. In many practical cases, this assumption of shift invariance is not valid, due, in part, to atmospheric disturbances when viewing points of a remote scene that are separated by sufficient angle, but also due to optical construction in large aperture systems without atmospheric turbulence. The former situation is of primary concern in this research effort.

Tactical sensors designed for use in a battlefield environment are quite different than those used to observe distant astronomical objects. A typical astronomical system has a fairly small field of view (FOV), hence the collected image may be modeled by the convolution of the remote object with a single PSF [61]. This PSF is the Fourier transform of the average system OTF, $\overline{\mathcal{H}}_{sys}(u,v)$, for some choice of long-term integration period. The length of the integration time period and other details of this statistically derived OTF will be deferred to the following sections.

Unfortunately, tactical sensors require a much wider FOV than do astronomical telescopes. Typical geometry constraints of tactical sensors require that the optical paths arising from individual points that comprise an extended remote scene pass through distinct parts of the turbulent atmosphere. The system can no longer be well characterized as a shift-invariant optical system, since no single OTF may be used to describe the transformation of every point in the remote scene to the image plane. An optical system with a FOV that admits optical paths through more than one atmospheric condition is said to exceed the isoplanatic angle.

1-6
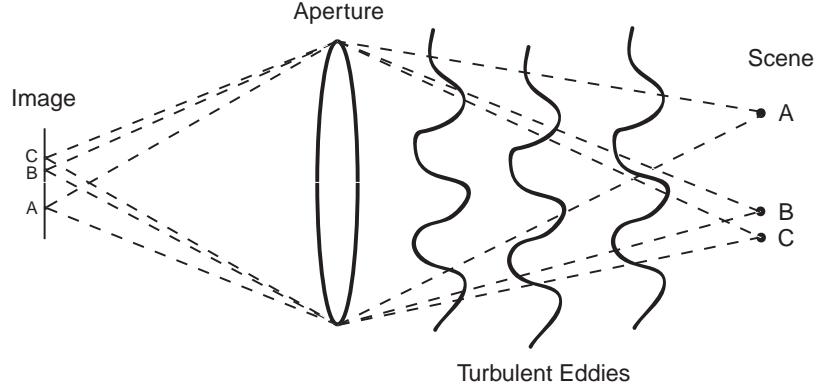
Figure 1.4:   Anisoplanatic imaging of point sources. Image paths through the atmosphere are different depending on the relative scene point separation. The image of point A will be formed through a considerably different atmosphere relative to that of the image of point B. Conversely, images of points B and C will be formed through approximately the same turbulent atmosphere. The angle created from the optical axis to points A and B is said to exceed the isoplanatic angle for some level of average turbulence, while the angle between points B and C lies within the isoplanatic angle.

Figure 1.4 depicts the geometry of a system that experiences anisoplanatic effects. Paths traced from a pair of point sources separated by some distance to the telescope aperture traverse regions of turbulence that possess different indices of refraction and thus tend to delay the optical phase by varying amounts. The atmospheric refractive index inhomogeneities or turbulent eddies [31] are assumed *frozen* according to Taylor's hypothesis during the gating period used to capture the image. The relative size of these refractive eddies causes varying levels of phase delay correlation between the optical paths, thus indicating a particular statistical structure of the atmosphere.

If the distance between scene points is small, the optical paths traced from both points are essentially identical. In this case, the transformation of the remote scene to an image behind the optical aperture may be accurately described by a single OTF, and the system is said to be spatially invariant. However, if the distance between points is increased beyond some limit, the optical paths from each point to the aperture are quite different. In fact, a separate OTF is required to accurately describe the imaging transformation of each point through the optical system.

Consider an extended scene that can be described as a broad collection of points. There exists some combination of scene extent and atmospheric condition, beyond which the system may no longer be accurately modeled with a single OTF. The separation of the extreme points of the scene gives rise to an angular separation of rays traveling to the aperture. The sufficiently turbulent optical condition is said to cause the system to exceed this *isoplanatic* angle, hence the system must be considered spatially variant. A common definition of the isoplanatic angle is "the angle between two points at which their mean-squared wavefront error due to differences in the atmospheric path is one radian squared" [33].

The isoplanatic angle of an arbitrary optical system using spherical wave propagation is given by [61]

$$\theta_0(L) = \left(1.09 \left(\frac{2\pi}{\lambda} \right)^2 L^{8/3} C_n^2 \right)^{-3/5}. \tag{1.3}$$

where C_n^2 is the atmospheric structure constant , λ is the mean optical wavelength and L is the atmospheric path length.

As an example, for a system viewing a scene at 10 Kilometers using a mean optical wavelength of 1.54 microns through a nominal horizontal-path daytime atmosphere with structure constant of $C_n^2 = 10^{-14}$, the calculated isoplanatic angle is 1.1 microradians. The maximum extent of a remote scene is

$$d_{max} = 2L \tan \left(\frac{\theta_0}{2} \right). \tag{1.4}$$

At a range of 10 Kilometers, the maximum spatially-invariant extent of the object under consideration is only 1.1 centimeters. Most target scenes of tactical interest will have an extent that exceeds the isoplanatic angle for moderately turbulent atmospheric conditions.

The ramifications of exceeding the isoplanatic angle are significant. No longer can simple linear deconvolution be applied to the images obtained from a spatially

variant optical system. The relatively simple image model of Eqn. 1.2 does not apply to such a system. Instead, Eqn. 1.2 must be modified to include the effects of a myriad of distinct PSF contributions to the model.

1.4 Previous Anisoplanatic Imaging Research

Several research teams have investigated the difficult problem of imaging through anisoplanatic turbulence. Although much of the research has been conducted with emphasis towards incoherent imaging of celestial bodies and objects within Earth's orbit, there has been limited research intended to solve problems associated with imaging extended scenes across nearly horizontal slant paths through dense regions of the Earth's atmosphere. Of this limited horizontal path imaging research, only a small subset has been devoted to image reconstruction using partially coherent illumination of the remote scene.

Roggermann [61] has effectively applied a block-matching technique that treats a captured incoherent infrared image as a series of *isoplanatic patches*, each of which can be accurately modeled as a portion of the scene transformed by a particular OTF. His research team recognized that the main effect of a turbulent atmosphere is to cause a local linear phase delay or tip and tilt to an isoplanatic image, although other effects such as focus anisoplanatism occur to a lesser extent. In the case of an image comprised of many isoplanatic patches, each patch will undergo a certain level of random displacement due to the linear component of phase distortion specific to each patch. Since the propagation of an image from the aperture to the detector can be approximated by a scaled Fourier transform, this linear phase distortion causes image displacement specific to each patch. The motion of each isoplanatic patch is decorrelated from the motion of other patches in the image to some extent. Given a series of independently realized images, a parallel processing algorithm is then used to estimate the linear shifts experienced by each patch. The shifts are effectively removed by the block-matching algorithm, allowing better reconstruction of the final image while retaining sufficient high spatial frequency. However, such an approach

suffers from the tremendous computational burden of computing the block-match derived motion estimate for each of the patches. Additionally, the algorithm must have some prior knowledge of the turbulence strength in order to decide on the number of patches to match.

A similar approach is employed by several researchers, although the methods used to align the patches across multiple image frames has been varied. Fraser *et al.* investigated the performance of a clever hierarchical implementation of subimage patch correlation registration. Their theories were experimentally validated [75] with a series of well conducted modelboard experiments using local heating elements to cause optical turbulence effects.

Several years later, Clyde [15] realized good reconstruction results using gradient subimage registration techniques and found improvement over correlation-based methods reported in [23]. A fairly comprehensive study was performed in [9] to evaluate the effects of the size of the individiual isoplanatic patches required to achieve acceptable images for application to astronomy and surveillance.

Finally, Bondeau [6] derived a Bayesian estimator to reconstruct images from a series of Gaussian noise corrupted edge contours presented to a multi-frame algorithm, resulting in a reconstructed edge-map of the scene with increased high spatial frequency detail. Essentially, the discrete contour vertices compare to the individual isoplanatic patches described in [9, 15, 23, 75].

Perhaps the most significant impediment of the application of these and similar algorithms to the tactical scenario is their poor performance in low SNR conditions. Given photon-limited individual raw frames that comprise an ensemble, any registration technique that must operate on localized subsets of the entire image suffers from relatively poor performance [23].

An innovative approach to recovering extended scenes in anisoplanatic imaging conditions is offered by Thelen [70], who uses phase diverse speckle images to jointly estimate the image and parameters of several discrete phase screens used to model

1-10

atmospheric turbulence. The incoming light is split to create the conventional image together with an image that has a small but known amount of defocus. Although the estimator is not described, the author claims to construct a system that delivers a maximum likelihood estimate for the image, as well as the Zernike basis coefficients of a small number of phase screens placed at various locations between the remote scene and aperture. In addition to estimating the original image, the algorithm allows estimation of the component phase screens that model the degrading atmosphere. Such detailed atmospheric information is of interest to implementors of adaptive optic (AO) systems, as well as those who seek accurate estimate parameters describing the structure of the turbulence. An interesting result of their research is their conclusion that phase screens more proximate to the aperture were better estimated than those closer to the remote scene.

A multiframe processing algorithm is described in [19] that has been shown to effectively mitigate image degradation from coherent speckle and anisoplanatic viewing conditions by iteratively processing subimage regions of a remote scene. It appears that the independent processing of multiple subimages by the modified Ayers-Dainty blind deconvolution algorithm [2] admits improvement for images formed by a spatially variant imaging process.

A tributary of related research is dedicated to the demonstration of the existence of *super-resolution* effects obtained by an optical system that images scenes that exceed the isoplanatic angle. Charnotskii [12] postulated in 1989 the possibility of achieving optical resolution beyond the diffraction limit of a telescope by exploiting the frequency shifting components of the turbulent optical path between the scene and aperture. He then presented a detailed experimental procedure to observe this effect. Further analysis was conducted several years later by Fried [24].

Gerwe [28] devised an iterative algorithm to reconstruct a remote extended scene using a series of short-exposure images, and demonstrated that Fourier components above and below the diffraction limit were enhanced by the technique [29]. Addition-

ally, studies of the required photon noise level were conducted. He later applied these techniques to the deconvolution of under-sampled images of wide FOV low-Earth orbiting satellites.

Most recently, Lambert provides limited simulation data to support the applicability of this technique under high signal-to-noise (SNR) conditions [44, 45]. Horizontal-path simulations and real-world imagery are used to support the super-resolution hypothesis.

Finally, it is worth noting that Sheppard has developed a multi-frame reconstruction algorithm that apparently achieves resolution beyond the diffraction-limited cutoff for isoplanatic images, and reports simulation data [67,68] to support his claims. Despite the postulated improvements available through super-resolution techniques, the extremely high signal levels required to achieve acceptable imagery restrict this approach to a fairly limited subset of the data collected by tactically employed laser-vision systems.

The approach taken over the course of the following chapters departs from the established body of literature in several aspects. Image reconstruction techniques that rely on subimage alignment suffer three major practical limitations. Perhaps the most fundamental limitation is the high SNR levels required to estimate the spatial displacement of each subimage. While correlation and block match alignment methods have been shown to work well on large images, accurate alignment of small subimages is only practical when the imagery is relatively noise-free. The choice of the number of subimage regions is also quite difficult and must be based on some assumption regarding the current structure of the atmosphere and system FOV. A more turbulent atmosphere would require processing of many more subimage regions than images produced during relatively calm viewing conditions. Finally, the computational burden required to align a large number of subregions is often in excess of that available on limited operational platforms in near real-time, especially under turbulent viewing conditions.

Although the modified Ayers-Dainty blind deconvolution algorithm provided in [19] seems promising, it is not clear that the convolution operator is appropriate for operation on individual frame subimages, since the detected intensity of each image is not linear for coherent illumination sources. In the cases studied by Dayton [19], it appears that the modified Ayers-Dainty blind deconvolution does increase resolution for imagery presented. However, the application of linear convolution to the image restoration process for coherent imagery is not mathematically justified [30]. The approach of the research in the following chapters requires frame averaging of some number of frames to produce an average image. This averaged image may be accurately considered the result of linear processing through the optical system, since the incoherently averaged image intensity at the detector follows a linear relationship with the intensity reflectance of the remote scene.

The image reconstruction approach developed during this research is novel in several important ways. The estimator is developed using Bayesian techniques based on the underlying statistical model of partially coherent illumination. Although considerable literature is devoted to reconstruction of incoherent imagery, the approach presented in this work concentrates on the formulation of reconstruction algorithms specific to partially coherent illumination. The initial estimator is extended to the case where the system FOV becomes so wide as to admit spatially variant effects in the detected image. Rather than partition the image into anisoplanatic patch subregions, a transfer function is developed to model the blur of the entire image. This approach is more applicable to the imaging conditions prevalent for tactical observation of remote targets using a laser vision system, due mainly to the low expected signal levels, but also due to the limited on-board processing capabilities of the carriage platform. Finally, a great deal of emphasis is placed on the accurate recovery of the seeing condition under which the imagery was collected. Such an estimate may be useful when developing imaging systems used for atmospheric measurement where scintillometry techniques become impractical. Although the main goal of the image reconstruction process is the formulation of useful imagery to the system operator,

accurate knowledge of the prevalent seeing condition under anisoplanatic conditions may be very useful in some applications.

1.5   Document Organization

The research described within this document is organized as follows. Chapter II provides the necessary background and mathematical underpinnings required to pose the problem and understand the fundamental models used to describe the statistics of the physical processes that occur in a partially coherent imaging system. That chapter covers the models used to describe the propagation of partially coherent light through a turbulent atmosphere, as well as models to describe the composition and simulation of that medium. A model describing the statistics of the partially coherent illumination source is offered and explored in the context of propagation through a turbulent medium. A maximum likelihood estimator is derived to establish the free parameter of the illumination detection model, which is used in subsequent chapters during the application of a joint estimator for the remotely imaged scene and atmospheric seeing conditions.

Chapters III and IV describe and refine joint estimators based on Baysian estimation techniques that seek a useful solution to the blind estimation problem of joint estimation of the remotely imaged scene together with the seeing conditions under which the data were collected. The derivations begin in Chap. III with a simple, shift-invariant model for the imaging system, and are modified in Chap. IV to include the deleterious effects of imaging through anisoplanatic viewing conditions. Simulated and experimentally gathered data are offered to support the operational utility of the blind estimation routines.

Chapter V moves away from the topic of blind deconvolution in order to better address the issue of multi-frame averaging in the context of partially coherent scene illumination. A probabilistic model is used for the detected images that comprise an ensemble, and this model is extended to form a likelihood metric that describes the admissibility of particular image frames into the aggregate ensemble. The chapter

begins by examining an iterative method that assigns weights to each image within the ensemble and it is found that the resulting weighted average image contains enhanced high spatial frequency content. The research is continued in the later half of the chapter to explore the feasibility of binary frame weighting, whereby selected frames are discarded from the ensemble in order to achieve similar increases in spatial detail. Simulated and experimental results are offered to reinforce the utility of the binary frame weighting algorithm.

The research is concluded in Chap. VI with some remarks that demonstrate the applicability of the research to several areas, as well as recommendations for further work in the field.

II. Coherent Imaging through Turbulence

Illumination of a remote scene by a partially coherent light source introduces interesting possibilities and difficult challenges to the image reconstruction process. The body of literature surveyed in Chap. I is exclusively devoted to scenes illuminated by narrowband incoherent light. The research documented in the following chapters is focused on the study of methods to reconstruct scenes illuminated by light that is highly coherent, as might be produced by a moderately stable, high-power laser. The Air Force and DoD components maintain great interest in such systems. Benefits include higher theoretical resolution due to the shorter wavelengths compared to forward looking infra-red (FLIR) systems, non-reliance on ambient light conditions and thermal contrast ratios, and long range imaging due to higher returned photon-count at the imaging device. The high available power levels from modern tactical targeting/illuminator laser systems, combined with rapid advances in image collection technology have made the long range capability an exciting and physically realizable feature of this technology.

This chapter presents background theory necessary to pose the general problem and conduct research toward restoration of an image of a remote scene illuminated with a coherent light source. Much of this material is derived from the established literature, although several sections represent original contribution to the field and are noted as such. Prior to the development of a maximum *a posteriori* (MAP) estimator for recovery of the remotely imaged scene in Chap. III, several crucial questions must be answered concerning the validity of the models and underlying assumptions used to construct such an estimator. The central tenants of the sections within this chapter are tied to the fundamental problem of reconstructing images formed using coherent illumination methods that have passed through vast distances of turbulent atmosphere. Strong emphasis is placed on the underlying statistics of the physical imaging models, as well as the random processes that govern the turbulence between the target and the *laser vision* system. With a complete understanding of the expected effects of the atmosphere on the propagated coherent target scene, the

reader is provided the tools necessary to construct a joint estimator that recovers MAP estimates of the remotely imaged scene together with the average atmospheric seeing conditions at the time of image collection.

The following sections outline the theory necessary to construct physically and statistically accurate models to represent the propagation of coherent illumination through the realistic atmospheric conditions typically encountered by tactical applications of a coherent vision system. A model that describes partially coherent illumination of, and reflection from a remote scene is presented in Sec. 2.1, followed by a brief treatment of the spatial sampling issues that arise during digital simulation of such a system in Sec. 2.2. The random statistics of a turbulent atmosphere are analyzed in the context of creating accurate digital representations of turbulence for simulation of realistic remote images in Sec. 2.3. The salient details of the experimental imagery system used to collect long-range remote imagery data is covered briefly in Sec. 2.4. The degree of coherence of the optical illumination system used to collect the experimental data was not well established at the time of data collection. Because of this, a maximum likelihood estimator for the speckle parameter of scenes imaged using a partially coherent system is developed in Sec. 2.5. To better understand the statistics of the detected intensity arriving at the detector of the imaging camera, a brief analysis of the statistical transformations that model the turbulent coherent imaging process are presented in Sec. 2.6. Some rather important image intensity scaling and quantization effects on the modeled data are discussed in Sec. 2.7. The effects of registration and frame averaging are used to justify a model for the optical transfer function imposed by the turbulent atmosphere in Sec. 2.8. The chapter concludes with a discussion of the method of knife-edge OTF estimation for application to seeing condition estimation from a series of experimentally collected laser radar images. Such estimates will be used to establish atmospheric truth from experimentally collected coherent imagery.
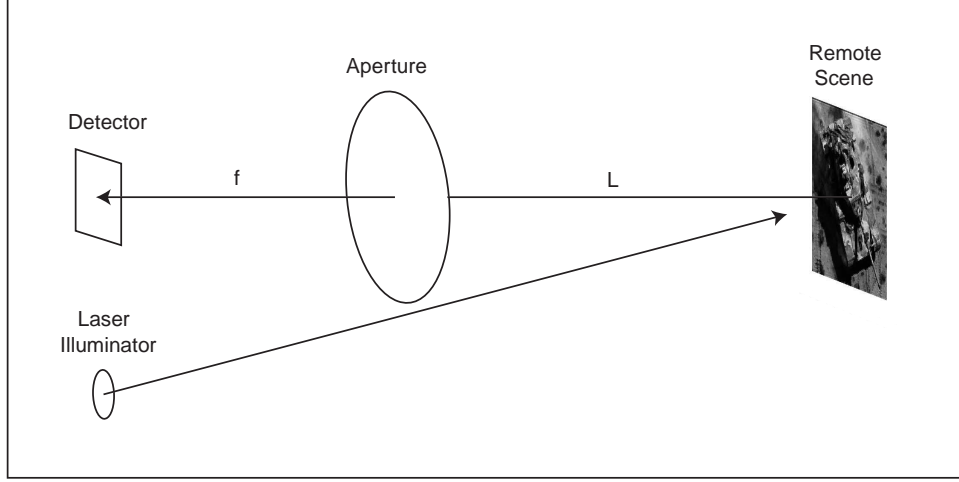
Figure 2.1:   Simplified sketch of the optical path from laser transmitter to optical detector. The remote scene is illuminated by a variable divergence laser illuminator to provide flood illumination of the target scene. Reflected light is propagated a distance of $L = z_t$ to the optical aperture, and propagated again a distance corresponding to the focal length f to the detector plane.

2.1   Coherent Imaging Model

Prior to exploration of the effects of atmospheric turbulence, it is necessary to construct a physical model of the deterministic propagation of coherent light through the atmosphere between the target and laser vision system. Figure 2.1 depicts a simplified sketch of the imaging paths. A model used to describe the formation of the kth image assumes the target is illuminated by a planar field

$$u_b^k(x_n, y_m, z_t) = A_b(x_n, y_m)e^{j\phi_{\tau_k}(x_n, y_m)}, \tag{2.1}$$

with units of volts per meter in the plane of the target a distance z_t meters from the laser imaging system. The amplitude of the beam is described by the function $A_b(x_n, y_m)$ and the phase is $\phi_{\tau_k}(x_n, y_m)$ during the coherence time τ_k. The variables x_n and y_m represent coordinates in the plane of the remote object to be imaged.

Although it is tempting to make a firm distinction between coherent and incoherent illumination, the terms are actually extremes in a continuum. In practice, one may obtain neither perfectly coherent nor perfectly incoherent light. Rather, the

illumination must be quantified using some measure of coherence. A long coherence time indicates a highly coherent optical source, with the phase of the optical waves marching in lock-step over moderate distances. In contrast, a source with a short coherence time will suffer from some decorrelation of the phase front over relatively small distances. Another, perhaps more intuitive way to visualize coherence time is by translation to the frequency domain. A source with infinitely long coherence time will possess a spectrum that appears as a Dirac delta function, while a short coherence time source will appear as a central frequency component, corrupted by noise sidebands. A narrowband filtered incoherent source will have flat power spectral density over some finite bandwidth and will have very short coherence time.

The *incoherent* illumination treated in the literature of Chap. I was actually narrowband filtered incoherent light. Clearly, such illumination has spatial and temporal correlation, however, the correlation is very limited due to the relatively high bandwidth of the light. In contrast, the *coherent* illumination considered within this research effort is sufficiently narrowband that it becomes convenient to use coherence time τ to describe its behavior. At some time longer than the coherence time, the phase relationship of the illumination is expected to depart from that of the reference sinusoidal center carrier frequency. The coherence time of a laser illuminator may be compared to the integration time period of the imaging detector used to collect photons of the illumination that reflect from a scene-of-interest. Detectors with relatively long integration periods or *gate times* will collect photons over many coherence periods. The significance of this phenomenon will be explored further in this section. Note that illuminator coherence over the duration of the round-trip travel time is not required. In fact, such long coherence times are difficult to achieve with operational laser illuminators.

The field reflected from the target, $u_r^k(x_n, y_m, z_t)$ with units of volts, can be computed by multiplying the field transmitted to the target as described by Eqn. 2.1 by the reflectance of the target $r(x_n, y_m)$, times the sample size employed in a digital

representation Δ_s.

$$u_r^k(x_n, y_m, z_t) = \Delta_s u_b^k(x_n, y_m, z_t) r(x_n, y_m) e^{j2\pi\theta(x_n, y_m)/\lambda}, \qquad (2.2)$$

where λ is the mean wavelength of the illuminator source, and $\theta(x_n, y_m)$ is a function describing target surface roughness in meters. The field reflected by the scene $u_r^k(x_n, y_m, z_t)$ is propagated back to the receiver aperture and may be modeled using a modified Rayleigh-Sommerfeld integral designed to propagate radiation from point sources [30]

$$u_a^k(x_{n2}, y_{m2}) = \frac{z_t}{\sqrt{2\pi}} \sum_{n=1}^{N} \sum_{m=1}^{M} \frac{u_r^k(x_n, y_m, z_t) e^{\frac{j2\pi\sqrt{(z_t)^2 + (x_n - x_{n2})^2 + (y_m - y_{m2})^2}}{\lambda}}}{(z_t)^2 + (x_n - x_{n2})^2 + (y_m - y_{m2})^2} e^{j\phi_a(x_n, y_m, x_{n2}, y_{m2})}, \quad (2.3)$$

where $u_a^k(x_{n2}, y_{m2})$ describes the field at the optical aperture, and $\phi_a(x_n, y_m, x_{n2}, y_{m2})$ is the phase delay function caused by the atmosphere, described further in Sec. 2.3. The field at the detector plane of the imaging system $u_d^k(x_{n3}, y_{m3})$ can be computed using one additional Rayleigh-Sommerfeld propagation integral

$$u_d^k(x_{n3}, y_{m3}) = \frac{f\Delta_a^2}{\lambda} \sum_{n2=1}^{N2} \sum_{m2=1}^{M2} \frac{u_a^k(x_{n2}, y_{m2}, 0) \ e^{\frac{j2\pi\sqrt{(f)^2 + (x_{n3} - x_{n2})^2 + (y_{m3} - y_{m2})^2}}{\lambda}}}{(f)^2 + (x_{n3} - x_{n2})^2 + (y_{m3} - y_{m2})^2} e^{j\phi_L(x_{n2}, y_{m2})}, \quad (2.4)$$

where f is the focal length of the system, and Δ_a is the sampling lattice spacing of the optical aperture. The field $u_d^k(x_{n3}, y_{m3})$ is the field in the detector plane in units of volts per meter, while the function $\phi_L(x_{n2}, y_{m2})$ represents the phase transformation of the lens or mirror used to focus the light collected by the aperture into the detector.

Assuming unity pixel fill-factor, the intensity of the kth signal at a pixel of the detector, I_d^k in units of watts, is computed by forming the magnitude squared of the field propagated to the detector, u_d^k

$$I_d^k(x_{n3}, y_{m3}) = \frac{1}{2}\eta\Delta_d^2\epsilon c|u_d^k(x_{n3}, y_{m3})|^2, \qquad (2.5)$$

where c is the speed of light in a vacuum, ϵ is the permittivity of free space, and Δ_d is the sampling lattice spacing of the detector, or pixel pitch. The detector array serves to integrate the signal over some discrete number of coherence times τ, sample the intensity pattern and then convert the signal to electrons.

$$I_e(x_{n3}, y_{m3}) = \sum_{k=1}^{\mathcal{M}} \tau_k \lambda I_d^k(x_{n3}, y_{m3})/(hc), \qquad (2.6)$$

where h is Plank's constant and $\mathcal{M}$ is the parameter that determines the degree of temporal and spatial speckle averaging that occurs due to the limited coherence of the laser source as compared to the duration of the illumination pulse.

The upper limit of the sum in Eqn. 2.6, $\mathcal{M}$ is a parameter that indicates the degree of coherence of the optical source [31]. To provide range gating and allow increased signal-to-noise ratio of the received illumination, coherent detectors are often gated by fairly short pulses. Although short, the length of the gating pulse τ_g is often many time longer than the coherence time of the optical source such that $\mathcal{M} = \tau_g/\tau$. For a fixed gate time, long coherence lasers have very low values for $\mathcal{M}$, while narrowband incoherent light sources have extremely large values of $\mathcal{M}$, with commensurately short coherence times, τ_k. A more complete treatment of the speckle parameter includes averaging effects due to spatial correlation in addition to purely temporal effects as described above. The model introduced in this section uses the simplifying assumption that spatial correlation effects are negligible. The speckle parameter will take on further significance in Sec. 2.5 as the statistics of the illumination are considered in more depth.

2.2 *Image Sampling for Simulation of Coherent Imaging*

The creation of an accurate digital representation of the coherent imaging process from the remote scene to the imaging detector requires that detailed attention be given to the spatial sampling of the detector, optical aperture, and remote target scene. Additional sampling concerns arise when simulating accurate statistical phase

screens necessary to model the turbulent atmosphere, as will be further discussed in Sec. 2.3. This section describes the framework of the digital simulation that is necessary to model the experimentally collected imagery described in Sec. 2.4. Several example calculations are included that use the actual parameters of the collection system used to record coherent imagery for this research effort.

Consider the simple model of an imaging system depicted in Fig. 2.1. Reflected partially coherent light from the target with a mean wavelength of λ is propagated over some distance L to the optical aperture with diameter D. The light is subsequently propagated to the imaging detector over the focal distance f to an imaging detector composed of a discrete array of detection elements. The $N \times N$ array of pixels of the imaging detector are separated by a spacing of Δ_d in both axes.

For a coherent optical system, the spatial sampling lattice period required to satisfy the Nyquist sampling theorem is inversely related to the extent of the optical aperture, and may be found using [30],

$$\Delta_d = \frac{\lambda f}{2D}. \tag{2.7}$$

Using example dimensions from the experimental system described in Sec. 2.4, a 3 meter focal length and 20 cm aperture diameter yield a minimum detector pixel spacing of 11.8 microns given laser illumination with a mean wavelength of 1.57 microns. It should be noted that the experimentally collected data was imaged using a detector with only 13 micron pixel spacing, resulting in slightly undersampled imagery.

Conversely, the Nyquist required sample lattice spacing at the optical aperture is inversely related to the overall extent of the imaging detector based on Fresnel scaling [30],

$$\Delta_a = \frac{\lambda f}{N \Delta_d}, \tag{2.8}$$

under the assumption that the system FOV is arranged such that all pixels of the detector are illuminated by the remote scene image. Using the figures above, the

sample spacing at the aperture is approximately 0.7 millimeters, requiring at least 285 samples per axis to completely sample the 20 centimeter aperture.

A wave-optics simulation was created to adequately model the propagation of coherent light from the target to the imaging detector. A natural choice for a sampling lattice at the aperture is to match the physical sampling of the experimental detector. Unfortunately, using the entire detector grid would yield unacceptably high computational requirements for generation of the thousands of speckle images required to conduct turbulent imagery simulations, given the complexity of the Rayleigh-Sommerfeld propagation integral of Eqn 2.3. Reducing the field of view by a factor of four in each direction results in substantially reduced computational complexity, while yielding an optical FOV that continues to dramatically exceed the corresponding isoplanatic patch size at the detector for all but the very weakest of turbulence simulations. This reduction in FOV yielded a modest 128×128 detector sampling lattice from which simulation parameters were derived in accordance with Eqn. 2.8.

2.3 Atmospheric Turbulence Model

Section 2.1 describes a model that is well suited to imaging through the vacuum of space or completely undisturbed air. However, any fielded *laser vision* system would require optical propagation through regions of atmosphere corrupted by significant levels of turbulence. To simulate the effects of the atmosphere, one well established approach is the treatment of the continuous atmospheric path between target and optical aperture as a series of discrete thin phase screens that act upon the backscattered coherent illumination from the target.

A key research goal is the joint estimation of the scene, together with parameters of the atmosphere that describe the resulting image blur. The estimation of atmospheric blur parameters may be considered merely as a by-product of the scene estimation. From another perspective, atmospheric condition information is of primary value, as it allows system designers and operators to apply this information to other components of the overall system. For this reason, the accurate estimation of

atmospheric parameters is very valuable. Unfortunately, image data collected from a remote scene is not often accompanied by an atmospheric truth source. One remedy is to collect images of the remote scenes in concert with scintillometer data that quantifies the atmospheric turbulence. In practice, such measurements are difficult and expensive due to the very long propagation paths typically encountered. Additionally, the need for such data renders previously collected scene data useless for atmospheric parameter calibration unless other means are employed to extract such information from the collected image data. A useful atmospheric parameter estimation technique that avoids scintillometry measurements is offered in Sec. 2.9.

The accurate construction of a realistic model of the atmospheric turbulence allows parameterized simulation of turbulence degraded imagery that can be processed by the joint image/atmospheric turbulence parameter estimator algorithm described in Chap. III. Additional insight gained from the atmospheric model may be used to understand the relationship of the phase-screen correlation and the effect that the atmosphere has on causing portions of the observed image to shift spatially at the image detector plane. The correlation between these shifts is an important tool used in the derivation of an anisoplanatic optical transfer function, as outlined in Chap. IV.

It is assumed that the variance of the log-amplitude fluctuations σ_χ^2 at the optical aperture is sufficiently small that the effects of turbulence are dominated by phase effects for nominal horizontal path imaging scenarios. This assumption has been shown to be useful in research involving atmospheric turbulence mitigation [61]. The assumption of phase dominated atmospheric conditions is required for the simplification the short exposure average optical transfer functions that describes the statistical response of the system [31]. The assumption allows a further important simplification that eases modeling requirements. By ignoring amplitude scintillation effects at the optical aperture, the distinct and discrete phase screens used to model a volumetric path between the scene and lens may be considered as a single thin phase screen placed immediately before the aperture. Goodman defines the random-phase screen as a screen that "changes the phase of the light transmitted in an unpredictable
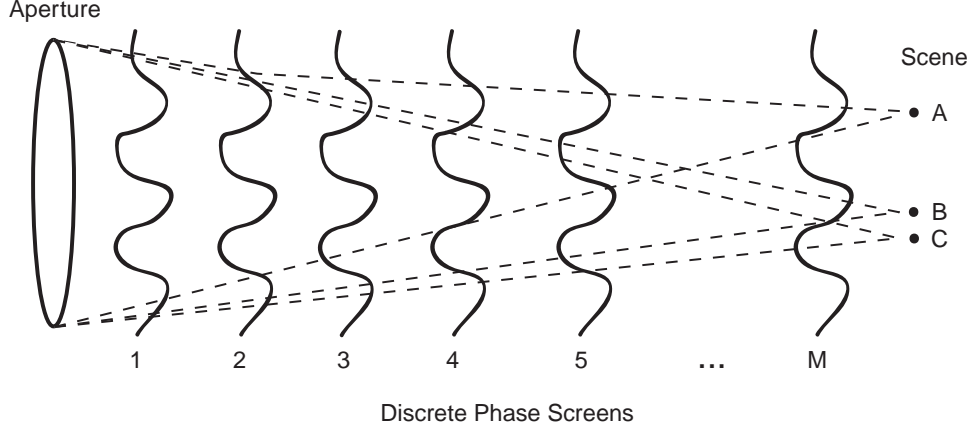
Figure 2.2: Phase screen representation of turbulent atmosphere. The volume of turbulent atmosphere is broken into a finite number of discrete phase volumes. Each of these component volumes is represented by a distinct phase screen. The screens may be collapsed to a single phase screen located at the aperture given assumptions regarding the strength of the turbulence.

fashion but does not appreciably absorb light" [31]. The summed contribution of the individual phase screens must be carefully considered to allow creation of a physically accurate model.

Figure 2.2 depicts the treatment of continuous phase perturbations caused by the atmosphere as a finite number of discrete phase screens, each with spatial correlation properties that are described by atmospheric conditions. Such a simplified model allows the generation of arbitrary images through various levels of random turbulence.

To construct the model, the characteristics of the turbulence must be represented by the individual phase screens. Turbulence is most conveniently modeled by quantifying the statistical distribution of the random turbulent eddies caused by the distributed heating and cooling of the atmosphere. The power spectral density (PSD) of the mth phase screen $\Phi_m(\kappa)$ may be quantified using several useful atmospheric turbulence models, including the Von Karman PSD [60]

$$\Phi_n^V(\kappa, z) = \frac{0.033 C_n^2(z)}{(\kappa^2 + \kappa_0^2)^{11/6}} exp\left\{ -\frac{\kappa^2}{\kappa_m^2} \right\} \tag{2.9}$$

where $\kappa_0 = 2\pi/L_0$ and $\kappa_m = 5.92/l_0$ with L_0 representing the outer scale diameter of the turbulence, and l_0 the inner scale diameter, in meters. $C_n^2(z)$ is the atmospheric structure constant and represents the multiplier of the PSD to account for the overall strength of the turbulence. Typical values for $C_n^2(z)$ might range from 10^{-17} $m^{-2/3}$ under excellent nighttime seeing conditions to 10^{-14} $m^{-2/3}$ under extremely poor daytime atmospheric turbulence conditions [61]. The functional dependence of $C_n^2(z)$ on distance from the aperture z may be dropped if a homogeneous turbulence volume is assumed, as might be encountered for horizontal imaging. In this case,

$$\Phi_n^V(\kappa) = \frac{0.033C_n^2}{(\kappa^2 + \kappa_0^2)^{11/6}} exp\left\{-\frac{\kappa^2}{\kappa_m^2}\right\}. \qquad (2.10)$$

Essentially, the physical model approximates the optical delay contributed by a single layer of the atmosphere as a Gaussian random process with an autocorrelation function that depends only on differences between locations in the aperture of the telescope [31]. Following Roggemann and Welsh [60], if (x_1, y_1) and (x_2, y_2) are spatial locations in a plane containing a random phase-screen, then the relative correlation distance between two parts of the phase-screen is defined by $\rho_m = [|x_2 - x_1|^2 + |y_2 - y_1|^2]^{1/2}$. Let ϕ_m be the optical delay in the pupil plane in radians due to the mth layer of the atmosphere in units of waves. A key quantity in characterizing the statistics of the phase screen is the autocorrelation of ϕ_m, denoted by R_m. Under the assumption of atmospheric isotropy and homogeneity, the function R_m depends only on the relative radial distance, ρ_m, between two locations of the phase-screen, i.e.,

$$R_m(x_1, y_1, x_2, y_2) \equiv E[\phi_m(x_1, y_1)\phi_m(x_2, y_2)] = R_m(\rho_m). \qquad (2.11)$$

The single-layer model described above can be extended to describe the phase distortion induced by the entire atmosphere through a multi-layer model [60]. Because the atmospheric layers are assumed to be statistically independent, the cross-correlation of the optical delay at two points in time and space is the sum of the

cross-correlation of each of the layers [60],

$$R(x_1, y_1, x_2, y_2) \equiv \sum_{m=1}^{M} R_m(\rho_m), \qquad (2.12)$$

where M is the number of layers. If the von Karman power spectral density of Eq. 2.10 is used to describe the spatial distribution of the index of refraction in each of the 2-D phase screens, the expression for the autocorrelation using an M-layer model is then given by [60],

$$R(x_1, y_1, x_2, y_2) = \frac{0.0351(2\pi)^4}{\lambda^2} \sum_{m=1}^{M} C_{n_m}^2 \delta z_m (L_o/4\pi)^{5/6} K_{5/6}[2\pi\rho_m/L_o]\rho_m^{5/6}, \qquad (2.13)$$

where $K_{5/6}$ is a modified Bessel function of the second kind of order 5/6, λ is the wavelength of the light, δz_m is the thickness of each atmospheric volume in the direction of propagation, and L_o is the outer scale of the turbulence.

The size of the random phase screen is determined by the size of the column of atmosphere originating at each point on the target and propagating to the telescope aperture. This is determined by the size of the aperture, the location of the extreme points of the scene under observation and the spatial sample rate in the aperture of the telescope. Additionally, care must be taken to properly size the overall extent of the phase screens due to sampling considerations. The lowest spatial frequency component attainable in simulation is inversely proportional to the overall extent of the phase screen. In order to properly account for low frequency contributions of atmospheric turbulence such as tip and tilt, relatively large phase screens must be constructed at the expense of large computational burden [35].

This autocorrelation model can be used to generate random-phase screens that possess the proper spatial correlations. Given the appropriate spatial autocorrelation function for each layer, individual realizations of turbulence may be generated by producing a matrix of zero mean, unit variance Gaussian random numbers, $G(x_1, y_1)$. Random 2-D uncorrelated phase screens may be appropriately filtered using the ap-

propriate correlation function by pointwise multiplying the Fourier transform of the
the derived autocorrelation function $R(x_1, y_1, x_2, y_2)$ with the spectral domain Gaussian screen [38].

A single realization of the turbulence for a single layer may be produced from the inverse 2-D Fourier transform of the multiplication of $F_G(u, v)$, which is the 2-D Fourier transform of the zero-mean, unit variance Gaussian random matrix $G(x_1, y_1)$, and $F_m(u, v)$ which is the square root of the 2-D Fourier transform of the correlation function $R_m(\rho_m)$,

$$\phi_m(x, y) = \sum_{u=1}^{N_1} \sum_{v=1}^{N_1} F_G(u, v) F_m(u, v) e^{-j2\pi(ux+vy)/N_1}. \tag{2.14}$$

This process yields a phase screen of N_1^2 number of points that statistically possesses a spatial autocorrelation equal to R_m, as long as the matrix containing R_m is constructed to be larger than twice the outer-scale of the turbulence, L_0, and is sampled at less than the period of the inner-scale of the turbulence, l_0. The total phase screen $\phi_a(x_n, y_m, x_{n2}, y_{m2})$ between a point in the target plane (x_n, y_n) and a point (x_{n2}, y_{m2}) in the aperture plane may be computed by summing the contributions along the unique path through individual phase screens in each layer between the target and the aperture. This path-dependent summation necessitates the creation of a new phase screen for each point (x_n, y_n) propagated from the target to the optical aperture. The final result is a collection of random-phase screens that encodes the proper degree of spatial correlation based on the strength and scale of the atmospheric turbulence, for a given optical path from each target point source to the optical aperture.

The creation of an aggregate phase screen allows the inclusion of stochastic turbulence effects by multiplication of the field arriving at the optical aperture given in Eqn. 2.3 with a thin lens transmissivity function described by the phase relationship of Eqn. **??**. The field propagated to the imaging detector plane becomes

$$u_d^k(x_{n3}, y_{m3}) = \frac{f\Delta_a^2}{\lambda} \sum_{n2=1}^{N2} \sum_{m2=1}^{M2} \frac{u_a^k(x_{n2}, y_{m2}, 0)\ e^{\frac{j2\pi\sqrt{(f)^2+(x_{n3}-x_{n2})^2+(y_{m3}-y_{m2})^2}}{\lambda}}}{(f)^2 + (x_{n3}-x_{n2})^2 + (y_{m3}-y_{m2})^2} T_{lens} T_{screen}, \quad (2.15)$$

where $T_{lens} = e^{j\phi_L(x_{n2}, y_{m2})}$ and $T_{screen} = e^{j\phi_a(x_{n2}, y_{m2}, x_{n3}, y_{m3})}$.

Reference to Fig. 2.2 demonstrates that the aggregate summed random-phase screen developed to model the imaging of point A will be considerably different than that employed to image point B or C. This is expected and desired for a model of a system that exceeds the isoplanatic angle described in Sec. 1.3. Rayleigh-Sommerfeld propagation, while computationally expensive, preserves the path-dependent relationships necessary to simulate anisoplanatic turbulence effects for a spatially variant imaging system.

2.4 Experimental Data Collection System

An experimental coherent imaging system was assembled by the Air Force Research Laboratories (AFRL) Sensors Division. Recent advances in the design of electron-bombarded charge-coupled device (EBCCD) imaging microchips has enabled the efficient capture of photons in the near infrared region used by the imaging system. The brassboard system is shown in Fig. 2.3.

The coherent imaging system was used to collect a very extensive set of target images at a variety of ranges between 3 and 27 kilometers. Table 2.1 describes some important operating characteristics of the laser used to illuminate the remote scene, while Table 2.2 describes the optical receiver system [47].

The individual images obtained by the coherent optical system were heavily corrupted by the speckle that is caused by the random variations of surface roughness that are on the order of an optical wavelength or larger, as well as atmospheric turbulence speckle. Figure 2.4 shows a representative speckle image of a target imaged at a range of 10 kilometers. To combat the effects of image speckle, a series of successive images were registered (motion compensated) and averaged. Figure 2.5

Figure 2.3: Brassboard coherent imaging system. A pulsed laser illuminator with relatively long coherence time is aimed along the optical boresight of a small aperture cassegrain telescope. The system was used to collect a large database of coherently illuminated images of various targets surrounding a mountaintop test range.

shows a representative image formed by registering a series of coherent speckle images collected by the laser vision system. For imagery collected at a range of approximately 10 kilometers, the system has an instantaneous field-of-view (FOV) of approximately 2.23 milli-radians (using a three meter focal length lens). This wide FOV is several orders of magnitude larger than the isoplanatic angle for a typical atmospheric profile, as calculated using expressions presented in [60]. This suggests that the isoplanatic patch size of the image detector array ranges from several tens of pixels to as small as a single pixel or less. It is also assumed that the turbulence seen by each frame acquired by the laser vision system will be statistically independent. This assumption is based on Taylor's Frozen Flow hypothesis [60] in conjunction with the relatively small aperture diameter of the system, the 10 Hz frame rate and surface winds usually in excess of 10 Knots during the testing of the sensor.

The required inter-frame period discussed above strictly applies to each intermediate thin phase-screen representations along the path to the target. However the atmosphere closest to the aperture creates the most significant phase aberrations at

Table 2.1: This table describes the parameters of the laser system used to illuminate remote targets at the North Oscura Peak (NOP) site of the White Sands Missile Range, New Mexico.

Parameter	Value
Laser Type	Nd:YAG w/KTP Optical Parametric Oscillator
Wavelength	1.57 micrometers
Pulsewidth	12 nanoseconds
Pulse Repetition Rate	up to 20 Hz (10 Hz limit due to camera)
Output Energy	130 milliJoule/pulse at 1.57 micrometers
Beam Diameter at 1/e	13 millimeters
Beam Divergence at 1/e	15 milliradian at 1.57 micrometers

the imaging plane. For the case of an airborne sensor, this limitation is not severe, as simple calculations reveal that the aperture movement through the atmosphere need not be great for nominal sizes of the outer scale of turbulence, L_0. However, on a ground-based optical range, wind speeds should be sufficiently high to satisfy this requirement. For example, for the case of a 1-meter outer scale turbulence size, a transverse wind speed of 10 m/s would result in completely refreshed (and thus statistically uncorrelated) atmosphere preceding the aperture every 10 ms. A frame rate of 10 Hz would admit this condition. In the case of the experimental collection system, the gated laser detector charge-coupled device (CCD) has a very fast shutter speed of approximately 12 ns and a frame capture rate of 10 Hz. Over the course of the optical testing for the data presented in Chapters III, IV and V, wind speed remained above 35 m/s with gusts much higher than that figure over the duration of the test period. A 10 Hz frame rate would thus permit outer scales of turbulence on the order of 3.5 meters. Such a figure provides a nominal value of expected turbulence outer scale according to the literature [60]. Although there may be a small degree of correlation between screens generated for different frames, the assumption of independence greatly simplifies the turbulence simulation.

Figure 2.4: Sample image collected by the coherent vision system. The image suffers from heavy degradation due to coherent speckle effects caused by target surface roughness.

Figure 2.5: Averaged image collected by the coherent vision system. The image was created by averaging 50 spatially registered frames. Registration and averaging is typically required to remove the objectionable effects of coherently formed speckle that is present in each of the individual frames.

Table 2.2:   This table describes the parameters of the laser vision receiver imaging system used to collect experimental imagery of remote targets at the North Oscura Peak site of the White Sands Missile Range, New Mexico.

Parameter	Value
Imaging Detector	Electron Bombarded Charge Coupled Device
CCD Manufacturer	Intevac, Inc.
CCD Wavelength	1.57 micrometers
CCD Quantum Efficiency	approximately 30%
CCD Output Data	12-bit digital
CCD Array Size	512x512 pixels
CCD Pixel Spacing	13 x 13 micrometers
CCD Active Imaging Area	6.7 x 6.7 millimeters
Optical Filter	1.57 micrometer laser line filter
Optical Aperture	8 inch
Optical Telescope Manufacturer	Celestron
Focal Length	2000 millimeter with 1.5x and 2x extenders
F-number	9.84 basic, 14.76, 19.68, 29.52 with extenders
Frame Capture Rate	10 frames per second

2.5   Image Speckle Parameter Estimation

One of the requirements of scene and atmospheric parameter estimation is to first obtain an estimate of the degree of temporal coherence of the laser source used to illuminate the remote scene. The following section documents a novel estimator developed over the course of this research effort to estimate the speckle parameter, $\mathcal{M}$ from a series of collected images taken at an experimental optical range. The speckle parameter is essentially a free parameter that must be estimated prior to employing the image restoration techniques described in Chapters I and IV.

The photon distribution for individual pixels of images collected by partially coherent imaging systems has been shown to follow a negative binomial random process [31].

$$P\left(K\right) = \frac{\Gamma\left(K + \mathcal{M}\right)}{\Gamma\left(K + 1\right)\Gamma\left(\mathcal{M}\right)}\left[1 + \frac{\mathcal{M}}{\bar{K}}\right]^{-K}\left[1 + \frac{\bar{K}}{\mathcal{M}}\right]^{-\mathcal{M}}, \qquad (2.16)$$
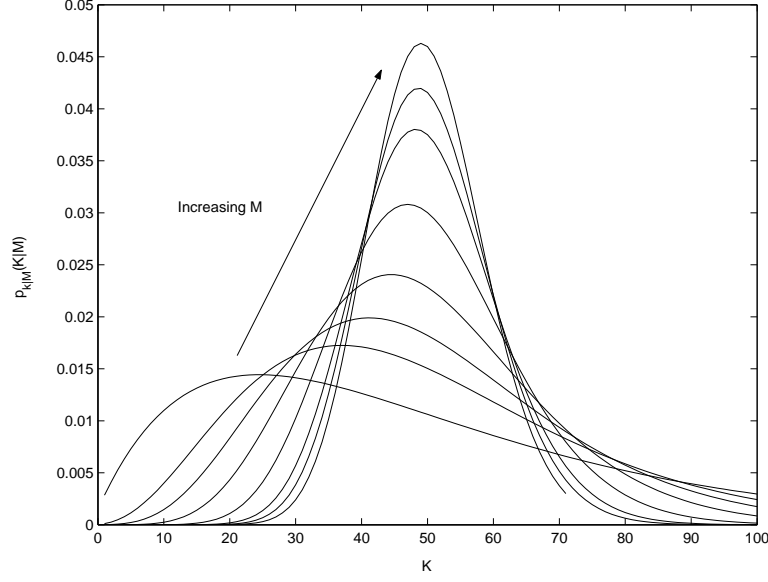
Figure 2.6: Plot of the negative binomial probability mass function with $K_{avg} = 50$. Curves are plotted for values of $\mathcal{M}$ ranging from 2 to 100. Note that in the limit as $\mathcal{M}$ increases without bound, the PMF approaches that of the familiar Poisson distribution.

where the distribution is parameterized by the mean photon count collected within a particular pixel, $\bar{K}$, and the speckle parameter $\mathcal{M}$. The speckle parameter may also be regarded as an indication of the variance of the distribution. Figure 2.6 shows various probability mass functions for differing values of the speckle parameter, given a constant mean of $\bar{K} = 50$ photons. In the limit as $\mathcal{M}$ grows without bound, the variance decreases to approach the mean of the distribution. This behavior is expected, as the negative binomial distribution tends to Poisson as $\mathcal{M}$ grows large.

The derivation of a maximum likelihood estimator for the speckle parameter $\mathcal{M}$ is straightforward [71]. The following development assumes integer values of $\mathcal{M}$ to expedite calculation of a useful estimate. For the case of J observations of a single pixel of an image, one can write the distribution as conditional on the two non-random parameters, $\bar{K}$ and $\mathcal{M}$

$$P\left(K \mid \bar{K}, \mathcal{M}\right) = \prod_{j=1}^{J} \frac{\Gamma\left(K_j + \mathcal{M}\right)}{\Gamma\left(K_j + 1\right)\Gamma\left(\mathcal{M}\right)} \left[1 + \frac{\mathcal{M}}{\bar{K}}\right]^{-K_j} \left[1 + \frac{\bar{K}}{\mathcal{M}}\right]^{-\mathcal{M}}. \qquad (2.17)$$

For convenience, the natural logarithm of the conditional probability may be computed as

$$
\ln\left[P\left(K \mid \bar{K}, \mathcal{M}\right)\right] = \sum_{j=1}^{J} \left\{ \ln\left[\frac{\Gamma\left(K_j + \mathcal{M}\right)}{\Gamma\left(K_j + 1\right)\Gamma\left(\mathcal{M}\right)}\right] - K_j \ln\left[1 + \frac{\mathcal{M}}{\bar{K}}\right] \right.
$$
$$
\left. - \mathcal{M}\ln\left[1 + \frac{\bar{K}}{\mathcal{M}}\right] \right\}. \qquad (2.18)
$$

The derivative of Eqn. 2.18 may be easily shown to be

$$
\frac{d}{d\bar{K}}\left\{\ln\left[P\left(K \mid \bar{K}, \mathcal{M}\right)\right]\right\} = \sum_{j=1}^{J}\left\{K_j\left[\frac{\mathcal{M}}{\mathcal{M}\bar{K} + \bar{K}^2}\right] - \frac{\mathcal{M}}{\bar{K} + \mathcal{M}}\right\}. \qquad (2.19)
$$

Setting Eqn. 2.19 to zero and solving for a zero yields a candidate for the maximum likelihood estimate for the pixel intensity

$$
\hat{K}_{ml} = \frac{1}{J}\sum_{j=1}^{J} K_j. \qquad (2.20)
$$

It is easy to show that $\hat{K}_{ml}$ yields a global maximum for the likelihood. The estimate is not surprising and may easily be shown to be unbiased. A more useful estimator may be found for the speckle parameter $\mathcal{M}$. However, the maximization approach used above is intractable, and a numerical maximization of the log-likelihood equation of Eqn 2.18 is practical.

Since $\Gamma\left(n + 1\right) = n!$ for positive integer n, it follows that

$$
\ln\Gamma\left(k\right) = \ln\left(k - 1\right)! = \sum_{i=1}^{k-1}\ln i \qquad (2.21)
$$

valid for all $k > 1$. Using this relationship, Eqn. 2.18 may be rewritten as

$$\ln\left[P\left(K \mid \bar{K}, \mathcal{M}\right)\right] = \sum_{j=1}^{J} \left\{ \sum_{i=1}^{K_j+\mathcal{M}-1} \ln i - \sum_{i=1}^{K_j} \ln i - \sum_{i=1}^{\mathcal{M}-1} \ln i \right.$$
$$\left. - K_j \ln\left[1 + \frac{\mathcal{M}}{\bar{K}}\right] - \mathcal{M} \ln\left[1 + \frac{\bar{K}}{\mathcal{M}}\right] \right\}. \qquad (2.22)$$

The computational burden of Eqn. 2.22 is reduced by the observation that the first K_j summation terms of the first two terms within brackets cancel, leaving

$$\ln\left[P\left(K \mid \bar{K}, \mathcal{M}\right)\right] = \sum_{j=1}^{J} \left\{ \sum_{i=K_j+1}^{K_j+\mathcal{M}-1} \ln i - \sum_{i=1}^{\mathcal{M}-1} \ln i \right.$$
$$\left. - K_j \ln\left[1 + \frac{\mathcal{M}}{\bar{K}}\right] - \mathcal{M} \ln\left[1 + \frac{\bar{K}}{\mathcal{M}}\right] \right\}. \qquad (2.23)$$

The closed form estimate of the mean intensity found in Eqn. 2.20 may be substituted into Eqn. 2.23 and the result maximized using standard numerical techniques such as steepest decent or Newton's method.

The utility of the estimator described above lies in its application to experimentally collected imagery. For a laser vision system composed of an illuminator with fixed integration period or gating time τ_g and stable coherence time τ, the speckle parameter may be considered unknown but constant over reasonable collection periods, given stable operating temperatures and other system factors. Given a large ensemble of experimentally collected image data, a useful estimate of the system $\mathcal{M}$ may be calculated using the estimator above.

Laser illumination propagated from the platform emitter to a remote scene will undergo some degree of amplitude and phase variation due to atmospheric turbulence effects discussed in Sec. 2.1. It is assumed that this additional variance produces an image ensemble that is also modeled by the negative binomial distribution, despite amplitude correlation effects observed at the target due to the size of the laser aperture or the turbulent seeing conditions.

2.6 Effect of Atmospheric Amplitude and Phase Distortion on Intensity Variation at the Detector

In the vacuum of space, it can be mathematically demonstrated that the intensity variation of the detected image formed under partially coherent illumination closely follows a negative binomial stochastic distribution [31]. A simple model of the coherent illumination of a remote target by a laser beam was presented in Sec. 2.1. It is not clear, however, that this relationship holds for the case of coherent propagation through a large volume of random turbulence, as might be encountered in terrestrial optical imaging applications. The following analysis will demonstrate why such a simple model is adequate for the purposes of this research study. The analysis will begin with a discussion of random phasor sums as required to understand the amplitude and phase fluctuations of a field propagated through random atmospheric turbulence. The discussion will then be extended to the negative binomial distribution discussed in Sec. 2.5 and it will be shown that the resulting distribution arriving at the detector remains negative binomial, despite random amplitude and phase fluctuations that affect the coherent illumination reflected from the target.

2.6.1 Random Phasor Sums. The following analysis describes the statistics of the amplitude and phase of a large sum of random phasors, and closely follows the development of [18]. The discussion is motivated by the Rayleigh-Sommerfeld integrals used for propagation of coherent light from the target to the aperture and detector. For example, referring to Equations 2.2 and 2.3, it is clear that each point on the optical aperture is formed by the summation of many such phasors, each of which has a random amplitude and phase due to target roughness under typical optical imaging conditions. Given a large set of N vectors having random amplitude α_k and random phase ϕ_k, one may construct the normalized random phasor sum

$$\mathbf{a} = ae^{j\theta} = \frac{1}{\sqrt{N}} \sum_{k=1}^{N} \alpha_k e^{j\phi_k}, \qquad (2.24)$$

from which the real and imaginary components may be expressed as

$$r = \Re\{\mathbf{a}\} = \frac{1}{\sqrt{N}} \sum_{k=1}^{N} |\alpha_k| cos(\phi_k)$$

$$i = \Im\{\mathbf{a}\} = \frac{1}{\sqrt{N}} \sum_{k=1}^{N} |\alpha_k| sin(\phi_k). \tag{2.25}$$

The expected value of each component is easily calculated since the expectation of both the sin and cos function is zero for uniform phase,

$$\langle r \rangle = \frac{1}{\sqrt{N}} \sum_{k=1}^{N} \langle |\alpha_k| \rangle \langle cos(\phi_k) \rangle = 0$$

$$\langle i \rangle = \frac{1}{\sqrt{N}} \sum_{k=1}^{N} \langle |\alpha_k| \rangle \langle sin(\phi_k) \rangle = 0. \tag{2.26}$$

Furthermore, the real and imaginary parts of the random phasors are uncorrelated, since $\langle cos(\phi_k) sin(\phi_m) \rangle = 0$,

$$\langle ri \rangle = \frac{1}{N} \sum_{k=1}^{N} \sum_{m=1}^{N} \langle |\alpha_k||\alpha_m| \rangle \langle cos(\phi_k) sin(\phi_m) \rangle = 0. \tag{2.27}$$

The variance of the real and imaginary components is identical,

$$\langle r^2 \rangle = \frac{1}{N} \sum_{k=1}^{N} \sum_{m=1}^{N} \langle |\alpha_k||\alpha_m| \rangle \langle cos(\phi_k) cos(\phi_m) \rangle = \frac{1}{N} \sum_{k=1}^{N} \frac{\langle |\alpha_k|^2 \rangle}{2}$$

$$\langle i^2 \rangle = \frac{1}{N} \sum_{k=1}^{N} \sum_{m=1}^{N} \langle |\alpha_k||\alpha_m| \rangle \langle sin(\phi_k) sin(\phi_m) \rangle = \frac{1}{N} \sum_{k=1}^{N} \frac{\langle |\alpha_k|^2 \rangle}{2}, \tag{2.28}$$

where $\langle |\alpha_k|^2 \rangle$ is the second moment of the amplitude of the phasors and is a property of the target reflectance.

Given a large number of random phasors where the real and imaginary compo-
nents are independent, the Central Limit Theorem allows construction of a joint PDF
of the resulting summation which is circularly Gaussian

$$p_{RI}(r,i) = \frac{1}{2\pi\sigma^2} \exp\left\{-\frac{r^2+i^2}{2\sigma^2}\right\}, \qquad (2.29)$$

where

$$\sigma^2 = \lim_{N\to\infty}\langle r^2\rangle = \lim_{N\to\infty}\langle i^2\rangle = \lim_{N\to\infty}\frac{1}{N}\sum_{k=1}^{N}\frac{\langle|\alpha_k|^2\rangle}{2}. \qquad (2.30)$$

This result is strictly applicable only in situations where the random amplitudes
α_k are independent and the phase ϕ_k is uniformly distributed on the interval $[-\pi,\pi]$.
Although it might seem an improbable distribution, the assumption of uniform phase
is appropriate to the imaging physics. For an unknown surface roughness of a target
that has a variance several times larger than the mean optical wavelength of the illu-
minating coherent beam, the resulting random phase becomes uniformly distributed
on the interval $[-\pi,\pi]$ due to phase wrapping effects.

Since the amplitude and phase are related to the real and imaginary components
of the phasor, r and i by the relationships

$$a = \sqrt{r^2+i^2}$$
$$\theta = \tan^{-1}\frac{i}{r}, \qquad (2.31)$$

the joint density function of a and θ may be found using the Jacobian matrix and
may be expressed as

$$p_{A\Theta}(a,\theta) = \begin{cases} \frac{a}{2\pi\sigma^2}\exp\left\{-\frac{a^2}{2\sigma^2}\right\} & \begin{array}{l} -\pi < \theta \le \pi, \\ a > 0, \end{array} \\ 0 & \text{otherwise,} \end{cases} \qquad (2.32)$$

from which the marginal distributions of a and θ may be easily calculated by integration [31]

$$p_A(a) = \begin{cases} \frac{a}{\sigma^2} \exp\left\{-\frac{a^2}{2\sigma^2}\right\} & a > 0, \\ 0 & \text{otherwise,} \end{cases}$$

$$p_\Theta(\theta) = \begin{cases} \frac{1}{2\pi} & -\pi < \theta \leq \pi, \\ 0 & \text{otherwise.} \end{cases} \tag{2.33}$$

The marginal densities of a and θ in Eqn. 2.33 may be multiplied to obtain the joint density of Eqn. 2.32, which demonstrates that A and Θ are also independent random variables as are the real and imaginary components of the phasors, as noted above by Eqn. 2.27.

The analysis above is central to the argument that the distribution of intensity at the detector plane follows a negative binomial distribution despite the effects of turbulence. To understand this statement, it is first necessary to examine several of the assumptions that lead to a negative binomial model for the detected intensity. For an integration time τ_g much shorter than the coherence time τ of the optical illumination, a detected pixel intensity is formed by a random phasor sum as discussed above, and has a complex envelope amplitude A which is Rayleigh as shown in Eqn. 2.33. Since the intensity I is the square of the amplitude, the distribution transforms to negative exponential [31]

$$p_I(I) = \frac{1}{2\sigma^2} \exp\left\{-\frac{I}{2\sigma^2}\right\} \tag{2.34}$$

for $I \geq 0$ and zero otherwise. However, for an arbitrary counting interval much longer than the laser coherence time, many such negative exponential distributions occur during the integration period of the detector, τ_g. Defining W as the integrated intensity over the counting period, the distribution of W can be shown to follow a

gamma probability density function [31],

$$p_W(W) = \left(\frac{\mathcal{M}}{\overline{W}}\right)^{\mathcal{M}} \frac{W^{\mathcal{M}-1} \exp\left(-\mathcal{M}\frac{W}{\overline{W}}\right)}{\Gamma(\mathcal{M})}, \tag{2.35}$$

where $\overline{W}$ is the mean integrated intensity, and $\mathcal{M}$ is the degree-of-freedom of the distribution, identical to the speckle parameter estimated in Sec. 2.5. The detection of intensity follows a doubly-stochastic process characterized by the statistics of the illumination $p_W(W)$, as well as the statistics of the photon-matter interaction, $P(K|W)$. The latter is commonly modeled to follow a Poisson distribution. Mandel's formula may be used to find the unconditional photon distribution at the detector plane [31], where

$$p(K) = \int_0^\infty P(K|W)p_W(W)dW$$

$$= \int_0^\infty \frac{(\alpha W)^K}{K!}e^{-\alpha W}p_W(W)dW, \tag{2.36}$$

and α is related to the mean integrated intensity by $\overline{K} = \alpha W$.

Substitution of Eqn. 2.35 into Mandel's formula of Eqn. 2.36 yields the negative binomial distribution of intensity at the detector for an arbitrary counting interval given in Eqn. 2.16 and repeated below for convenience,

$$P(K) = \frac{\Gamma(K+\mathcal{M})}{\Gamma(K+1)\Gamma(\mathcal{M})}\left[1+\frac{\mathcal{M}}{\overline{K}}\right]^{-K}\left[1+\frac{\overline{K}}{\mathcal{M}}\right]^{-\mathcal{M}}.$$

The key assumptions used to develop the random phasor sum analysis were independence of the amplitudes and phases of the individual phasors to be summed. The fact that the real and imaginary parts of the resulting amplitude phasors at the optical aperture are uncorrelated, together with the result that the phase is uniformly distributed on the interval $[-\pi, \pi)$, leads to the important observation that the same conditions are satisfied for the subsequent propagation from aperture to detector. The

introduction of a random phase due to atmospheric turbulence does not affect this analysis, since the phase due to the random phasor sum is uniform at the aperture. The addition of further phase effects will wrap modulo 2π and result in uniform phase distribution at the aperture. The result is a negative binomial intensity distribution at the detector, despite the addition of varying degrees of random phase disturbance due to atmospheric turbulence.

2.7   Effect of Image Intensity Scaling and Quantization

The estimator development of Chap. III is based on the statistics of photon arrival at the imaging detector plane. All digital image collection systems impose distortion on the statistics of the captured images due to the unavoidable scaling and quantization of the analog-to-digital (A/D) process, unless the added expense of a true photon-counting detector is justified. This distortion may be regarded as a modification of the probability distribution of the intensity.

Pixel intensity scaling that often accompanies the quantization process must be removed by characterization of the optical system. In most systems, this entails scaling of pixel intensity by a factor that represents the number of photons per intensity count. This factor is unity in a photon-counting camera system, but may be quite high for less sensitive detectors. Without scale correction, the intensity statistics of partially coherent illumination can no longer be accurately modeled by a negative binomial random process. Consider a scaling factor of $q = 1/p$, where p represents the number of photons per intensity count stored by the detector system. The mean of the photon intensity distribution is $\bar{K}$, while the variance is [31]

$$\sigma_K^2 = \bar{K}\left(1 + \frac{\bar{K}}{M}\right). \tag{2.37}$$

After scaling, the detected mean becomes $q\bar{K}$, while the detected variance is $q^2\sigma_K^2$, which is not equal to

$$\sigma_{qK}^2 = q\bar{K}\left(1 + \frac{q\bar{K}}{M}\right). \tag{2.38}$$

as required by specification of the negative binomial process. For non-photon counting detectors, $q < 1$, and the detected variance is lower than that predicted of a true negative binomial process. Unless properly compensated for, this phenomenon yields erroneously high estimates of the speckle parameter from partially coherent image frames.

As will be discussed in Sec. 3.2.3, accurate formulation of the statistical process variance is necessary to conclude iterations of the scene estimation algorithm. For non photon-counting systems the scaled image variance is calculated by $q^2\sigma_K^2$ using Eqn. 2.37.

Even after device scaling calibration is completed, the effect of pixel intensity quantization remains. In systems with coarse A/D intensity quantization, relatively large intensity variance is masked by the coarse assignment of these fluctuations to relatively few intensity bins. This phenomenon is especially notable in darker pixels where image SNR is low and the standard deviation of the pixel intensity is small compared to the quantization effect. The apparent variance is limited with a corresponding artificial increase in the estimated speckle parameter per Eqn. 2.37. Therefore, estimation of the laser illuminator speckle parameter as discussed in Sec. 2.5 is best accomplished using bright pixels with relatively large means. A bright pixel is therefore defined as one whose mean is high enough that the standard deviation of intensity is at least twice the quantization step size. Such a condition ensures that the noise process is dominated by intensity variation versus quantization effects. Furthermore, darker pixels from experimentally collected images tend to be governed by random processes such as additive noise introduced by system amplifiers or shot-noise typical of solid-state detector systems.

2.8 Effects of Image Registration and Averaging

The relatively long coherence times of candidate laser illuminators cause a significant degree of laser speckle for individually collected frames of 2-D LIDAR imagery. Additionally, the instantaneous distortion of the turbulent atmosphere causes what can be described as atmospheric speckle. Figure 2.7(a) illustrates these phenomena given a representative imaging scenario. Although created by distinct random processes, the cumulative effect of these distortions may be effectively reduced by simple image averaging after motion compensation as discussed below.

The phase distortions suffered by individual pixels of an image propagated through large volumes of turbulent atmosphere may be accurately assumed zero-mean Gaussian due to the Central Limit theorem. Furthermore, the summation of J laser-speckle images, each governed by an independent negative binomial process with speckle parameter $\mathcal{M}$, yields a negative binomially distributed composite image with a speckle parameter of $J \times \mathcal{M}$ [31]. The composite image has a mean intensity bound by a much lower variance than that of a single speckle image.

Image averaging reduces a large portion of the random effects of atmospheric and laser speckle image distortion. However, the task of image averaging is complicated by atmospheric tilt and platform motion or vibration. A first and necessary step towards image averaging is multi-frame registration. Significant research has been conducted towards the goal of image registration in general, and towards coherent image registration in particular [7, 53, 62]. The vector projection correlative registration algorithm of [7] is particularly attractive due to its computational efficiency and accuracy under conditions of low SNR. Since a projection-based algorithm can only remove global tip and tilt in an image, the resulting registered images will retain distortion components from higher-order atmospheric effects as well as laser speckle degradation. Figure 2.7(b) illustrates the combined effects of motion compensation and averaging. Perfect image registration performance is assumed for the analysis described in Chapters III and IV, although it is recognized that additional unmodeled
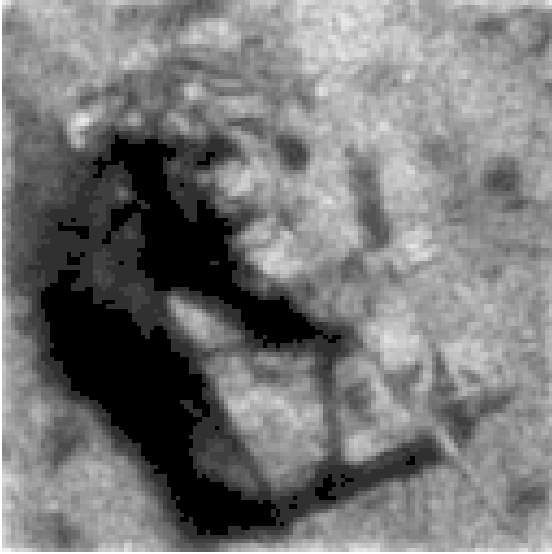
(a) Simulated single-frame image of a tank
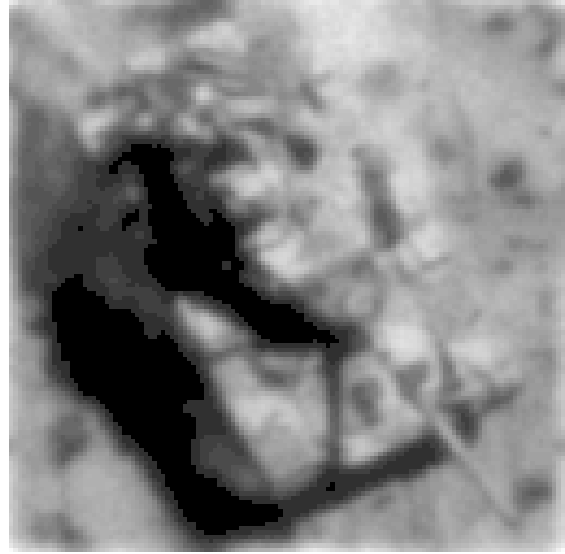
(b) Motion-compensated frame averaged tank image

Figure 2.7:   Subimage (a) shows a simulated single-frame image of a tank illumi-
nated by a coherent illuminator with a speckle parameter of $M = 60$ and propagated
through a 10 km turbulent path with a spherical r_0 value of 4 cm. Subimage (b)
shows a composite image created by motion compensating and averaging 40 frames of
speckle images typical of those shown in subimage (a). Note the dramatic reduction
of image speckle and loss of high-frequency image detail.

blur components will likely exist in simulated or experimental image data. Consid-
eration is given in Chap. V to the case where image registration might not provide
perfect tip/tilt compensation and thereby eliminate motion blur due to translational
shift components of the ensemble imagery.

The average short exposure transfer function has been shown to model the
atmospheric speckle image effects of a series of tilt-removed short exposure images
quite well. Under the assumption that individual speckle images collected by the
laser imaging system can be regarded as independent realizations of images collected
through a homogeneous and isotropic atmosphere, the following OTF may be used to
model the motion-compensated (tip/tilt-removed) ensemble average image [31],

$$\bar{\mathcal{H}}_{se}\left(\nu\right) = \exp\left\{-3.44\left(\frac{\lambda f \nu}{r_0}\right)^{5/3}\left[1 - \left(\frac{\lambda f \nu}{D}\right)^{1/3}\right]\right\}, \qquad (2.39)$$

where f is the effective system focal length, ν is a radial spatial frequency variable, D is the diameter of the optical aperture, and r_0 is Fried's optical seeing parameter. For fixed optical components, the short exposure OTF is completely parameterized by r_0. The short exposure OTF therefore provides an excellent candidate for use as the kernel to deconvolve a blurred image in order to obtain the original image together with the atmospheric seeing condition parameterized by r_0.

For an optical system that processes coherent illumination, the field propagation from plane to plane may be considered a linear process. However, the detected intensity does not follow a linear relationship with the originating intensity due to the constructive and deconstructive phase summations of the random phasors. This phenomenon provides mathematical insight towards the observation of laser speckle in a coherent imaging system. In contrast, if a large number of coherently formed intensity images are averaged over a period of time much larger than the coherence time, the composite image is essentially an incoherently formed intensity map of the remote scene, and does follow a linear relationship with the originating intensity. The optical system may thus be considered a linear, shift-invariant system and the intensity of an image pixel, $i(x, y)$, may be modeled as the convolution of the statistically averaged system point spread function with the remote scene,

$$\bar{h}_{sys}(\xi, \eta) = \mathcal{F}^{-1}\{\bar{\mathcal{H}}_{se}(u, v) \times \mathcal{H}_{opt}(u, v)\}, \qquad (2.40)$$

where $\mathcal{F}^{-1}$ is the inverse Fourier transform operator and $\mathcal{H}_{opt}(u, v)$ is the OTF of the fixed optical system. It is assumed that the effects of finite pixel size are quite negligible compared to the blur induced by the atmosphere. With perfect motion compensation, a pixel of the average image may be expressed as the discrete convolution of $\bar{h}_{sys}(\xi, \eta)$ with the remote scene, $o(\xi, \eta)$,

$$i(x, y) = \sum_{\xi=1}^{N} \sum_{\eta=1}^{N} \bar{h}_{sys}(x - \xi, y - \eta) o(\xi, \eta). \qquad (2.41)$$

with images formed by a detector of size of $N \times N$ elements.

2.9   Knife-Edge OTF Estimation from Coherent Imagery

The impulse response of a fielded optical system may be deduced from a set of experimentally collected image data from a remote scene containing a step target. Such a target contains sufficient contrast to extract the spatial step response of the system from one of its edges. The methods described in [78] were used to recover an estimate of Fried's seeing parameter from experimental imagery collected by the brass-board system described in Sec. 2.4.

A large set of short-exposure images of a step resolution target was collected by the experimental laser vision system described in Sec. 2.4. These data were analyzed to produce an estimate of the actual atmospheric seeing conditions. The individual image frames were spatially registered by correlation with a synthetically generated step target. This process allowed accurate motion compensation of the image ensemble. The remaining image blur was then analyzed to estimate the seeing conditions of the atmosphere for the experimentally collected data.

The first step in the process involves registering and temporally averaging hundreds of frames of image data containing the step target. The registration process was executed on a small portion of the frame containing 10 pixels in the vertical direction and 20 pixels in the horizontal direction. This configuration was used so that anisoplanatic effects would be minimized due to the small angular extent of the target. Anisoplanatic effects cause increased blurring in the temporal average due to spatially uncorrelated motion which would tend to bias the estimated seeing condition towards an unfairly low value of r_0. The non-square size of the frame was chosen to increase averaging in a dimension that did not affect the registration process, since the step target contained no additional features in the image region where the step was not in transition.
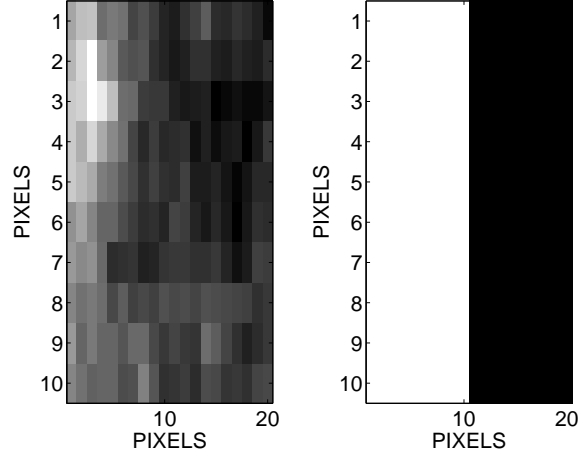
Figure 2.8:   Typical image of the step target used to compute the impulse response (left) and an image of the ideal step target used to register the frames (right).

As an example, Fig. 2.8 shows a typical frame of step target data as well as the synthetic step used to accomplish the registration process. This dataset included 300 frames of imagery collected from a remote step-contrast target imaged under atmospheric turbulence conditions thought to range from approximately 1 to 20 cm.

After registration and averaging, the spatial gradient in the horizontal direction was computed in order to estimate the derivative of the step response. The derivative of the step response is the impulse response of the system in the horizontal direction [78]. The short exposure impulse response was computed for different values of r_0 between 1 and 20 centimeters in increments of 0.1 centimeters using the model described in Eqn. 2.39 and a diffraction limited point spread function convolved with a pixel of the appropriate size [60]. Using an example dataset, it was found that the lowest mean squared error between modeled and measured point spread functions was obtained for a value of $r_0 = 3.9$ cm. Figure 2.9 shows the recovered impulse response and the simulated impulse response for an r_0 of 3.9 cm. This particular dataset will be used in Chap.III to provide atmospheric truth to the experimentally collected data used to test the proposed blind deconvolution algorithm.
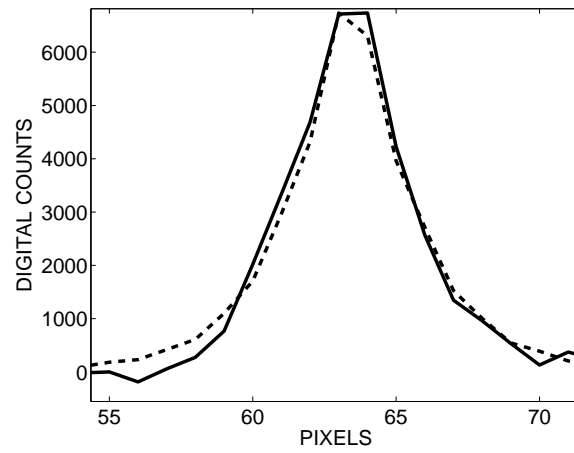
Figure 2.9:   Impulse response recovered via knife edge calculations from the step target measurements (solid line) and an impulse response calculated using a short exposre OTF with an r_o of 3.9 cm (dashed line).

III. Image Reconstruction and Seeing Condition Estimation using MAP Estimation

The purpose of this chapter is to develop a mathematical model of a robust and accurate estimation algorithm that recovers both the remotely imaged scene intensity, as well as the atmospheric seeing conditions under which the imagery was collected. The maximum *a priori* (MAP) estimator seeks a solution to the blind deconvolution problem where an image is presented to the image processor, yet the original truth scene and blur function of the optical system is not known. The construction of such an estimator is simplified somewhat by assuming a general form of the blur function. Under such an assumption, the research falls into the more restrictive category of parameterized blind deconvolution for image reconstruction.

Active coherent illumination of remote scenes adds considerable flexibility to the task of optical battlefield sensing. Unfortunately, high-power laser illuminators typically have fairly long coherence times, resulting in highly coherent scene illumination. Although multi-frame averaging helps to mitigate the speckled appearance of the composite image as discussed in Sec. 2.8, the statistics of the resulting image cannot be accurately modeled using a Poisson random process unless relatively incoherent laser sources are used, or alternatively, a very large number of data frames are combined.

Images collected by a partially coherent LIDAR system experience atmospheric distortion due to the highly turbulent atmosphere of the expected operating environment. Airborne imaging systems are subject to severe atmospheric distortion due to the long slant-range path required of typical tactical scenarios, while ground-based systems will operate over shorter ranges, but through extremely turbulent conditions caused by proximity to the ground. In either case, typical seeing conditions will be limited not by the optical aperture, but rather by the atmospheric coherence diameter quantified by Fried's seeing parameter r_0.

The development of a joint estimator to discover both the remote image reflectance and atmospheric seeing condition falls into the general research category of

coherent image reconstruction. Past efforts involving LIDAR image reconstruction may be roughly divided into adaptive optic (AO) or post-processing techniques, although there have been some composite approaches, e.g. [69]. AO techniques [60, 79] promise good image reconstruction at the expense of relatively heavy, complex systems often unsuitable for manned and unmanned fighter and reconnaissance platform deployment. Furthermore, such an approach often requires point source illuminators or *guide stars* to estimate the instantaneous atmospheric OTF. Research geared to the problem of blind image deconvolution may be applied to incoherent image reconstruction, and such efforts are well surveyed in [41] and [42]. However, the treatment of blind deconvolution of non-Poisson distributed image sets is not well covered in the literature, nor has the problem of parameterized blind convolution been thoroughly studied.

This chapter is organized as follows. Sections 3.1 and 3.2 describe the development of the MAP estimator for partially coherent multi-frame image data, while Sec. 3.2.3 discusses some important implementation details. Section 3.3 presents the results of estimation of seeing parameters and image recovery for both real and simulated datasets. Conclusions and areas of further research are described in Section 3.4.

3.1 Joint Maximum a priori *Image and Seeing Condition Estimation*

Chapter II provided a fairly complete discussion of the important details required to model a coherent optical system operating in the presence of unknown levels of turbulence. The key points of that discussion are summarized in the context of building an estimator that recovers an estimate of the remotely imaged scene. Without a sufficiently accurate model of the blurring effects due to anisoplanatic turbulence, the short exposure OTF provides a firm foundation for parametrization of effects of turbulence on the tilt-compensated optical system. The average OTF of such an optical system $\bar{\mathcal{H}}_{sys}$, including turbulence, can be mathematically described by

$$\bar{\mathcal{H}}_{sys}\left(u,v\right) = \mathcal{H}_{opt}\left(u,v\right)\bar{\mathcal{H}}_{se}\left(u,v\right).\tag{3.1}$$

where $\mathcal{H}_{opt}$ is the non-random OTF of the optics, and $\bar{\mathcal{H}}_{se}$ is the short exposure OTF described by Eqn. 2.39. For fixed optical components, focal length and operating wavelength, the average blurring effects of the atmosphere are completely quantified by the atmospheric coherence diameter, or seeing parameter, r_0. This model serves as a reasonable starting point for the construction of an image restoration algorithm under spatially invariant imaging conditions, where the system FOV is smaller than the isoplanatic angle. Treatment of spatially variant viewing conditions is deferred until Chap. IV.

The experimental laservision system described in Sec. 2.4 captures a series of speckle images for post-processing by an off-board image restoration algorithm. These images are first spatially registered and then averaged to form a motion-compensated frame average (MCFA) image with reduced speckle and motion blur. The MCFA image is an array, $\mathbf{d}$, that represents a measurement of the unknown remote scene $\mathbf{o}$ at the imaging detector. If the characteristics of the atmosphere at the time of image collection were known, this information might be used to construct an estimate of the short exposure OTF and could then be used as the deconvolution kernel to recover the best estimate of the remote scene using an inverse Wiener filter or similar techniques [40]. Unfortunately, due to the random nature of the atmosphere and unknown conditions likely to be encountered by a fielded mobile laser vision system, an accurate estimate of the atmospheric condition is not usually available. Such conditions motivate the method of blind deconvolution by MAP estimation derived in the following section.

3.2 MAP Estimator Derivation

This section uses classical estimation theory to help derive a joint MAP estimator for the remotely illuminated scene together with the atmospheric seeing condition represented by r_0.

Let $\mathbf{D}$ be a random matrix representing a motion-compensated frame averaged (MCFA) image from a collected ensemble of J speckle images, while $\mathbf{O}$ is a non-

random matrix which represents the remote scene or ground truth, R_0 is a random variable representing the average spherical seeing parameter and $\mathbf{d}$, $\mathbf{o}$ and r_0 are specific realizations of each. Because individual pixel intensity has been shown to follow the distribution of Eqn. 2.16, one may express the probability of the detected image pixel given a particular remote scene pixel as

$$P[d(x,y) = D(x,y)|o(x,y) = O(x,y)]$$
$$= \frac{(d(x,y) + \mathcal{M})!}{(d(x,y) + 1)!\mathcal{M}!}(1 + \frac{\mathcal{M}}{i(x,y)})^{-d(x,y)}(1 + \frac{i(x,y)}{\mathcal{M}})^{-\mathcal{M}} \quad (3.2)$$

where $\mathcal{M} = J \times \mathcal{M}_{frame}$ is the composite speckle parameter of the laser illuminator for the MCFA image, $\mathcal{M}_{frame}$ is the speckle parameter of each frame in the ensemble, $d(x,y)$ is a pixel of the MCFA data, constructed from J independent speckle images, and $i(x,y)$ is the average intensity of a corresponding pixel according to Eqn. 2.41.

Bayes rule provides the *a posterior* probability given the *a priori* probabilities,

$$f_{\mathbf{O},R_0|\mathbf{D}}(\mathbf{o},r_0|\mathbf{d}) = \frac{f_{\mathbf{D}|\mathbf{O},R_0}(\mathbf{d}|\mathbf{o},r_0)f_{R_0}(r_0)f_O(o)}{f_{\mathbf{D}}(\mathbf{d})}. \quad (3.3)$$

Note that the denominator of Eqn. 3.3 is the probability of a specific realization of a detected image. Although this probability is not easily determined, it is not conditioned upon the parameters of interest, and can be treated as a constant value when forming a likelihood function [71]. The prior $f_{R_0}(r_0)$ is unknown, but may be assumed as discussed below. The probability of the object in the numerator, $f_O(o)$, is unknown, and may be assumed to be a uniform distribution. In this case, Eqn. 3.3 can be more simply expressed as

$$f_{\mathbf{O},R_0|\mathbf{D}}(\mathbf{o},r_0|\mathbf{d}) = \frac{f_{\mathbf{D}|\mathbf{O},R_0}(\mathbf{d}|\mathbf{o},r_0)f_{R_0}(r_0)}{f_{\mathbf{D}}(\mathbf{d})}. \quad (3.4)$$

Although arbitrary remote scenes certainly have some level of spatial correlation, image pixel distributions are assumed to be spatially independent from those of

neighboring pixels. The assumption of identically distributed and independent pixel distribution is mathematically convenient and common in the derivation of maximum likelihood image estimators [39, 57]. Thus, the total log-likelihood function can be expressed as the product of the independent prior probabilities

$$L(\mathbf{o}, r_0) = \sum_{x=1}^{N} \sum_{y=1}^{N} \left(\ln[f_{D(x,y)|O(x,y),R_0}(d(x,y)|o(x,y), r_0)] \right) + \ln[f_{R_0}(r_0)] \qquad (3.5)$$

or by substitution with Eqn. 3.2,

$$L(\mathbf{o}, r_0) = \sum_{x=1}^{N} \sum_{y=1}^{N} \left(\ln \left[\frac{(d(x,y) + \mathcal{M})!}{(d(x,y) + 1)! \mathcal{M}!} \right] - d(x,y) \ln \left[1 + \frac{\mathcal{M}}{i(x,y)} \right] \right.$$

$$\left. - \mathcal{M} \ln \left[1 + \frac{i(x,y)}{\mathcal{M}} \right] \right)$$

$$+ \ln[f_{R_0}(r_0)]. \qquad (3.6)$$

The probability density function, $f_{R_0}(r_0)$, represents the probability of the seeing parameter r_0 being equal to a specific value, R_0. The form of the probability density function for the random parameter r_0 is assumed to be exponential raised to the power of the number of pixels in the array with a mean determined by environmental conditions,

$$f_{R_0}(r_0) = \left[\frac{e^{-N^2 \frac{r_0}{r_{avg}}}}{r_{avg}/N^2} \right]. \qquad (3.7)$$

The choice of this form for the probability of r_0 is based on the empirical observation that atmospheric seeing is seldom extremely better than the average and can often be much worse. This model also introduces numerical advantages in that its logarithm is very simple to compute and the entire distribution is characterized by a single parameter, r_{avg}. The influence of the assumed prior is discussed further in Sec. 3.2.3.

3.2.1 Joint Maximization of the MAP Likelihood Function.   Joint parame-
ter estimation of the remote scene together with the seeing parameter requires maxi-
mization of an $N^2 + 1$ dimensional surface. A practical approach to maximizing joint
likelihood is to select fixed candidate values for the seeing parameter, $r_0 = r_0'$, and to
maximize the likelihood of the remote scene under the assumed atmospheric condi-
tions. The entire parameter space may be searched by selecting discrete values of r_0'.
Under this simplification, the log likelihood of a particular remote scene pixel reduces
to

$$L(o(x,y), r_0') = \ln[f_{D(x,y)|O(x,y),R_0} f(d(x,y)|o(x,y), r_0')] + \ln[f_{R_0}(r_0')]. \qquad (3.8)$$

By substitution of Eqn. 3.8 with Equations 2.16 and 3.7, it can be shown that

$$L(\mathbf{o}, r_0') = \sum_{x=1}^{N} \sum_{y=1}^{N} (d(x,y) \ln[i(x,y)] - [d(x,y) + \mathcal{M}] \ln[i(x,y) + \mathcal{M}])$$

$$-N^2 \frac{r_0'}{r_{avg}} - \ln\left[\frac{r_{avg}}{N^2}\right]. \qquad (3.9)$$

An assumption is made that there exists a particular realization of a remote
scene, $\hat{\mathbf{o}}_{ml}$, that maximizes the likelihood of Eqn. 3.9 at the discrete seeing condition
r_0', and thus, under the necessary optimality condition

$$\frac{\partial L(\hat{\mathbf{o}}_{ml}, r_0')}{\partial o(\xi, \eta)} = 0. \qquad (3.10)$$

Differentiation of an averaged image pixel given by Eqn. 2.41 with respect to
the remote scene is simply

$$\frac{\partial i(x,y)}{\partial o(\xi, \eta)} = \bar{h}_{sys}(x - \xi, y - \eta) \qquad (3.11)$$

for each pixel, and $\bar{h}_{sys} = \mathcal{F}^{-1}(\bar{\mathcal{H}}_{sys})$ from Eqn. 3.1. The derivative of $L(\mathbf{o}, r'_0)$ with respect to $\mathbf{o}$ is then

$$\frac{\partial L(\mathbf{o}, r'_0)}{\partial o(\xi, \eta)} = \sum_{x=1}^{N}\sum_{y=1}^{N} \left(d(x,y)\frac{1}{i(x,y)}\frac{\partial i(x,y)}{\partial o(\xi,\eta)} \right.$$
$$\left. - (d(x,y) + \mathcal{M})\frac{1}{\mathcal{M} + i(x,y)}\frac{\partial i(x,y)}{\partial o(\xi,\eta)} \right). \tag{3.12}$$

By substitution with Eqn. 3.11

$$\frac{\partial L(\mathbf{o}, r'_0)}{\partial o(\xi, \eta)} = \sum_{x=1}^{N}\sum_{y=1}^{N} \left(\frac{d(x,y)}{i(x,y)}\bar{h}_{sys}(\xi - x, \eta - y) \right.$$
$$\left. - \frac{d(x,y) + \mathcal{M}}{\mathcal{M} + i(x,y)}\bar{h}_{sys}(x - \xi, y - \eta) \right). \tag{3.13}$$

For the important case where $d(x,y) = i(x,y)$ for every x and y, it is easy to show that the functional is everywhere negative, hence the optimality point found by Eqn. 3.10 is a maximum. Although it is unlikely that direct solution to this maximization problem might be found, an iterative solution may be used. An iterative maximization process may be realized by setting Eqn. 3.13 to zero and arranging terms to yield

$$\sum_{x=1}^{N}\sum_{y=1}^{N} \left(\frac{d(x,y)}{i(x,y)}\bar{h}_{sys}(\xi - x, \eta - y) \right)$$
$$= \sum_{x=1}^{N}\sum_{y=1}^{N} \left(\frac{d(x,y) + \mathcal{M}}{\mathcal{M} + i(x,y)}\bar{h}_{sys}(x - \xi, y - \eta) \right). \tag{3.14}$$

In a manner consistent with the derivation of the Richardson-Lucy algorithm [57], both sides of the equation may be multiplied by the remote scene $\mathbf{o}$, and an update equation may be formed to produce an iterative solution for the estimated

scene parameter

$$\mathbf{o}^{new}(r'_0) = \mathbf{o}^{old}(r'_0) \frac{\sum_{x=1}^{N} \sum_{y=1}^{N} \left(\frac{d(x,y)}{i^{old}(x,y)} \bar{h}_{sys}(x - \xi, y - \eta) \right)}{\sum_{x=1}^{N} \sum_{y=1}^{N} \left(\frac{d(x,y)+\mathcal{M}}{\mathcal{M}+i^{old}(x,y)} \bar{h}_{sys}(x - \xi, y - \eta) \right)}, \tag{3.15}$$

with

$$i^{old}(x,y) = \sum_{\xi=1}^{N} \sum_{\eta=1}^{N} \bar{h}_{sys}(x - \xi, y - \eta) o^{old}(\xi, \eta). \tag{3.16}$$

In all cases examined, the algorithm produces a solution that yields an estimate of the observed scene given a MCFA image degraded by speckle and photon noise at discrete values of r'_o. A search over a range of r'_o is performed to find the MAP estimate of the scene and Fried's atmospheric seeing parameter. As will be discussed in Section 3.3, the free parameter r_{avg} described in Eqn. 3.7 seems to present ambiguity in the recovered estimate of r'_o. It was found that successive iterations of the iterative algorithm, starting with an initial value of r_{avg} equal to the diameter of the optical system aperture, provide an estimated seeing condition which was found to decrease towards and stabilize on a final solution for an estimate of r'_o. Although direct repetitive iteration would be time consuming, a more efficient approach will be discussed towards the end of Sec. 3.2.3.

3.2.2   Extension of MAP Estimator to Large Frame Averages.   It is informative to derive the MAP estimator of Eqn. 3.15 for the case where the number of registered speckle images in the ensemble increases without bound. Alternatively, the coherence time of the laser illuminator may be decreased to a point where the speckle parameter becomes very large. In both situations, the negative binomial distribution characteristic of partially coherent illumination tends to the more familiar Poisson distribution that describes incoherent scene illumination. Using a similar derivation

3-8

as outlined above, the MAP estimator becomes

$$\mathbf{o}^{new}(r'_0) = \mathbf{o}^{old}(r'_0) \frac{\sum_{x=1}^{N} \sum_{y=1}^{N} \left(\frac{d(x,y)}{i^{old}(x,y)} \bar{h}_{sys}(x-\xi, y-\eta) \right)}{\sum_{x=1}^{N} \sum_{y=1}^{N} \bar{h}_{sys}(x-\xi, y-\eta)}. \tag{3.17}$$

where the denominator acts as a normalization constant to allow conservation of intensity for each iterated image, and $i^{old}(x,y)$ is given by Eqn. 3.16. This result is an expression of the Richardson-Lucy algorithm, commonly applied to image reconstruction problems that involve Poisson noise processes [57]. The contribution of Eqn. 3.15 lies in its ability to provide a decision-theoretic MAP estimate of the remote scene for cases where partially coherent illumination is unavoidable, as in tactical scenarios where frame gathering time is critical, and high-powered laser illuminators necessarily have correspondingly low speckle parameters.

3.2.3   Algorithm Implementation and Choice for $\mathbf{r_{avg}}$.   The update algorithm for successive image frame iteration of Eqn. 3.15 may be easily implemented in a quasi-realtime system by recognizing the double-summation of the pointwise divided images as discrete convolutions. Using fast Fourier implementations, iteration rates of $10-20$ Hz are common using modern desktop personal computers operating on 256×256 pixel images. The initial scene iteration may be started using a uniform image matrix for $\mathbf{o}^{old}$ with a common intensity value equal to the mean of the input MCFA image, $\mathbf{d}$. A faster final estimated solution is realized by setting the $\mathbf{o}^{old}$ equal to the MCFA, however, zeros contained in the MCFA data will prevent update at the corresponding pixel location for the final estimated image, $\mathbf{o}^{new}$.

The mean intensity matrix, $\mathbf{i}^{old}$ is calculated iteratively by circularly convolving the system PSF with the previously iterated scene estimate, $\mathbf{o}^{old}$. Iterations may be terminated when the mean-squared difference between the mean intensity $\mathbf{i}^{old}$ and the new image $\mathbf{o}^{new}$ convolved with the system transfer function $\bar{h}_{sys}$ becomes less than

the predicted variance of the negative binomial distribution per Eqn. 5.12, or when

$$\sum_{x=1}^{N}\sum_{y=1}^{N}\left(i(x,y)-d(x,y)\right)^2 \leq \sum_{x=1}^{N}\sum_{y=1}^{N} d(x,y)\left(1+\frac{\sum_{x=1}^{N}\sum_{y=1}^{N} d(x,y)}{\mathcal{M}}\right). \qquad (3.18)$$

Accurate algorithm termination is enhanced by using only bright pixel regions to form estimates of image variance as discussed in Sec. 2.7.

In general, blind deconvolution is an ill-posed problem [41]. The assumed prior for r_0 presented in Eqn. 3.7 distinguishes this MAP estimator from a maximum likelihood estimator by preventing the trivial solution of $\hat{\mathbf{o}} = \mathbf{d}$ with $\hat{r}_0 = \infty$. In such a case, the operator would simply be presented with the MCFA image and informed that the atmosphere caused no distortion. The assumed prior effectively combats selection of the trivial solution by forcing a slow decrease in total likelihood as r_0 is increased. In some situations, the average seeing condition may be well quantified. In the case of completely unspecified atmospheric conditions, the introduction of the prior introduces the free parameter r_{avg}. To solve the estimation problem in these cases, the algorithm may be initiated with a larger than expected value for r_{avg}, on the order of the system entrance aperture diameter. The MAP estimate of $\hat{r}_0$ may then be substituted for the next estimate of r_{avg}, and the algorithm repeated to iteration stopping criteria when $\hat{r}_0 \approx r_{avg}$. This *outer iteration* does not require that the entire algorithm be run at each iteration. The first two terms in Eqn. 3.9 can be computed as a function of $\hat{r}_0$ in the first iteration and saved as only the logarithm of the prior changes as a function of r_{avg}. The logarithm of the prior as a function of $\hat{r}_0$ and r_{avg} can be pre-computed and stored in a lookup table. This makes the implementation of the iterative approach for finding r_{avg} as fast as the implementation of the algorithm when r_{avg} is known *a priori*.

3.3   Results

This section compares the MAP blind deconvolution algorithm using both simulated and experimentally collected data. Simulated data were constructed to compare

well with resolution board and step target data collected at a mountaintop test range using a candidate imaging laser radar system described in Sec. 2.4 [54].

Table 3.1 describes the significant parameters of the simulated data. The experimental laser illuminator speckle parameter was estimated according to the technique documented in Sec. 2.5. Although 12-bit image quantization effects tended to bias results obtained from observation of dark pixels, a nominal estimate of $\mathcal{M}_{frame} = 60$ was obtained from observation of the bright regions of several image sets. Motion compensated ensembles of J averaged images yielded composite speckle parameter estimates modeled by $\mathcal{M} = J \times \mathcal{M}_{frame}$ described in Sec. 2.8.

Ground truth imagery was not available in the case of experimental image collection. In this case, a comparison is made between the MAP estimated seeing condition and the seeing condition estimated using the knife-edge line-spread function estimation technique described in Sec. 2.9.

Table 3.1: Table describing the simulation parameters used to create the turbulence degraded imagery used to recover Fried's seeing parameter using MAP estimation.

Parameter	Value
Slant Range to Target	10 Kilometers
Optical Diameter	20 Centimeters
Number of Phase Screens	10
Distance Between Phase Screens	1 Kilometer
Speckle Parameter of Source	60
Pixels per Image	128 by 128
Pixel Pitch of Detector	11.8 Micrometers
Mean Wavelength	1.54 Micrometers
Focal Length	3 Meters
Images per Frame Ensemble	50
Size of Imaged Target Area	5 by 5 Meters

3.3.1 Results Obtained using Simulated Image Data. Simulated imagery was created using Rayleigh-Sommerfeld wide FOV imaging as described in Sections 2.1 through 2.3. In order to properly account for laser speckle effects, 60 images were
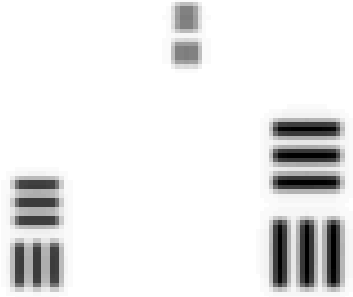
Figure 3.1: Diffraction limited simulated image reflectance pattern used to test algorithm performance.

propagated through identically distributed but independent random phase screens. The resulting images were averaged in order to simulate a single image with the proper speckle parameter of $\mathcal{M} = 60$. The synthetically generated image data were quantized to 10-bit resolution in order to match the limited quantization of the experimentally collected data described in Sec. 3.3.2. Atmospheric distortion was varied by simulating various spherical r_0 values representing D/r_0 values of 4, 2.5, 2, 1.3 and 1.0. One thousand frames of partially coherent image data were generated for each of the five atmospheric conditions. 50-Frame motion-compensated frame average images were constructed and introduced to the iterative MAP estimator, using uniform initial scene estimates with the average seeing condition initially set to $r_{avg} = D$, the diameter of the optics. The diffraction-limited object is shown in Fig. 3.1.

Algorithm iteration was usually complete within 30-60 seconds using a general purpose PC running at 2.8 GHz, with differential image variance decreasing to the analytically predicted value of Eqn. 2.37 within approximately 200-300 iterations for low values of r'_0, and approximately 30-50 iterations as r'_0 values closer to D were searched. The change in log-likelihood was found to monotonically increase in all
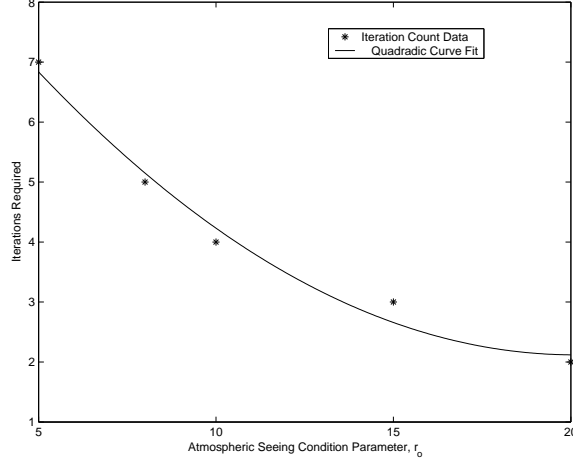
Figure 3.2:   Plot of the number of iterative solutions required to allow the estimated r_0 to be within 10% of the final estimated solution. Initial guess of r_{avg} was set to the optical diameter.

cases, with no tendency to decrease for subsequent iterations at a particular value of r_0'. Without introducing a stopping criteria for the iterative algorithm at each value of r_0', iterative estimation of the scene was found to continue beyond the point where the recovered scenes accurately represented the initial MCFA used as input to the algorithm. Iteration to a stable value of r_0 given an initial guess of $r_{avg} = D$ was fast for scenes created with low atmospheric turbulence, although the number of required iterative solutions increased for more turbulent conditions. Figure 3.2 shows the number of solutions required to move the estimated value of $\hat{r}_0$ from the initial estimate of $r_{avg} = D$ to a value within 10% of the final iterated value.

Visual inspection of the resulting images indicated improved spatial resolution. Table 3.2 shows the MAP estimated values of spherical $\hat{r}_0$ versus the actual seeing parameter used to create the turbulence. Figure 3.4(a) shows a representative MCFA image for the condition of $D/r_0 = 4$ ($r_0 = 5$ cm) used as input to the algorithm, while Fig. 3.4(b) shows the recovered image using the MAP blind deconvolution process. Note that the estimated seeing conditions presented in Table 3.2 indicate a consistently pessimistic recovery of the actual seeing conditions used to create the image

data. It is possible that such bias may be attributed to motion blur effects induced by anisoplanatic viewing conditions. This result is further discussed in Sec. 3.4.

Table 3.2: Simulated truth and estimated values for Fried's seeing parameter r_0 as estimated using the MAP estimation blind deconvolution algorithm described in Sec. 3.2.

Simulated r_0 (cm)	estimated $\hat{r}_0$ (cm)
5	4.7
8	7.5
10	9.6
15	14.4
20	19.1

3.3.2 Results Obtained using Experimentally Collected Image Data. Experimentally collected data was limited to a pair of 300-image datasets collected for a particular atmospheric condition on a controlled mountain-top optical range. A resolution bar target and a step-intensity target were imaged according to the parameters outlined in Table 3.1. Both targets were arranged such that only slight azimuth change was required to image either target, ensuring similar atmospheric profiles. Additionally, imaging of the target sets was separated in time by approximately 2 minutes. The 10 km optical path to the remote target prevented accurate atmospheric truth using scintillometer measurements. In order to compare results, the atmospheric seeing condition of the experimentally imaged step-intensity target was estimated using the knife-edge OTF estimation technique described in Sec. 2.9. The averaged wind speed was recorded in excess of 35 meters per second at the optical aperture.

The experimental system used to collect image data for this effort was not a photon-counting system. A calibration factor of $p = 6$ photons per count [47] was introduced to properly scale the image intensity as discussed in Sec. 2.8. In addition, the experimental collection system quantized the image intensity data into 12-bit words. Dynamic range considerations of the analog-to-digital conversion process fur-

3-14
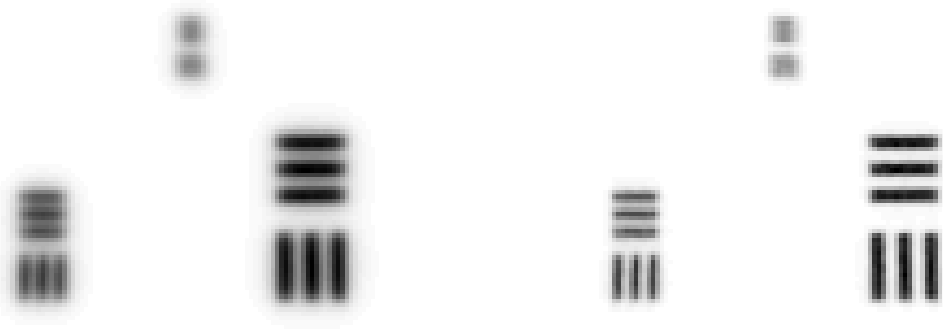
(a) Simulated motion-compensated frame average (MCFA) image for blind deconvolution algorithm

(b) Recovered image using MAP estimation

Figure 3.3:   Comparison of simulated motion compensated frame average (MCFA) image under atmospheric conditions of $D/r_0 = 4$ ($r_0 = 5$ cm) against the MAP estimated image. Subfigure (a) is the original MCFA image, while Subfigure (b) shows the MAP recovered image which was produced for a most likely estimate of $\hat{r}_0 = 4.7$ cm. Note the additional high-frequency spatial detail of Subfigure (b) relative to Subfigure (a).
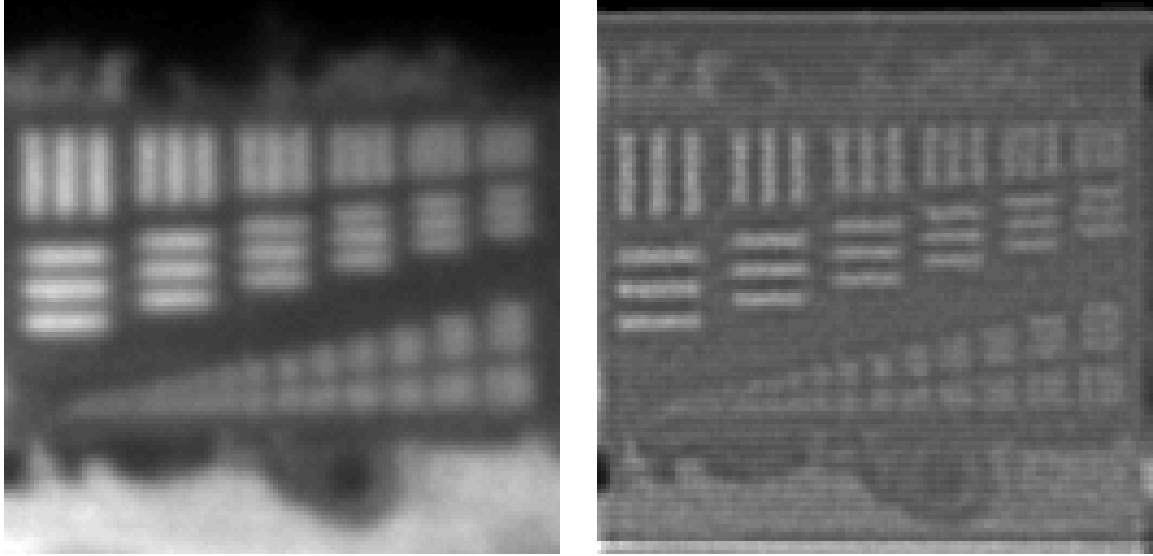
(a) Experimental motion-compensated frame average (MCFA) image for blind deconvolution algorithm

(b) Recovered experimental image using MAP estimation

Figure 3.4: Comparison of experimentally collected motion compensated frame average (MCFA) to the MAP estimated image. Subfigure (a) is the original MCFA image, while Subfigure (b) shows the MAP recovered image which was produced for a most likely estimate of $\hat{r}_0 = 3.6$ cm. Note the additional high-frequency spatial detail relative to Subfigure (a). Estimated image contrast is somewhat reduced by image edge effects of the deconvolved image due to the circular convolution properties of the discrete Fourier transform.

ther decreased the quantization to approximately 10 bits overall for the images used in this study.

Blind deconvolution of both the step intensity and resolution bar targets was performed, yielding an estimate of 3.6 cm for the spherical seeing parameter, together with maximum likelihood images. Figure 3.4 (a) shows the 10 km MCFA image of the resolution bar target as input to the algorithm, while Fig. 3.4 (b) shows the result of deconvolution. The estimate of atmospheric condition is in fairly good agreement with a figure of 3.9 cm derived from the knife-edge response of the step-intensity target.

3.4 Conclusions and Discussion

The agreement of estimated seeing conditions with simulated and experimental truth is encouraging. Imagery produced by the automatic algorithm consistently yields an appreciable increase in high frequency image detail, while avoiding the tendency to settle on a trivial solution where the estimated scene equals the motion compensated averaged image data.

For the case of simulated data, it was noted that the estimates of $\hat{r}_0$ were approximately 6% low, representing pessimistic seeing conditions. This discrepancy might be caused by the relatively high levels of anisoplanatism inherent in the simulated data.

Although the limited experimental data was in close agreement with truth deduced from knife-edge response techniques, it was noted that the estimate of $\hat{r}_0$ was approximately 8% low. The knife-edge response technique was performed on a small region of the step-target image, thus negating the additional blur caused by anisoplanatism. Given confidence in the truth data yielded by the knife-edge techniques, it appears that the MAP estimator is estimating poorer seeing conditions than actually encountered during data collection, since the MAP estimator uses the entire (anisoplanatic) MCFA as input data. For this particular viewing geometry, it can be shown that the isoplanatic angle is much smaller than the field of view. Using [60], the isoplanatic angle is approximately 24 microradians for a spherical $r_0 = 4$ cm, while the system field of view is slightly greater than 50 milliradians. However, the tilt isoplanatic angle is significantly larger than 24 microradians [61]. Clearly, anisoplanatic effects warrant consideration for these data.

The myriad of isoplanatic patches that comprise the detected image tend to cause additional blurring not modeled by the short exposure OTF of Eqn. 2.39, despite ideal global image registration. A better system model would include the additional blurring effects that are produced by the anisoplanatic imaging process. The analysis presented in Chap. IV attempts to resolve the quantitative effects of this blur, and

replace the short exposure OTF with a transfer function that captures the effects of isoplanatic patch motion blur.

The importance of accurate motion compensation was recognized during the early portion of these experiments. Without accurate image frame registration, the system models presented in Chap. II tend to become less valid as noted by inspection of Eqn. 1.1. In the extreme case where no motion compensation is performed, the application of a long exposure OTF [31] becomes appropriate under certain conditions, with the unavoidable loss of image detail. The problem of image registration blur as well as blur caused by heavy anisoplanatic warping is considered in Chap. V.

IV. Anisoplanatic Optical Transfer Function for Blind Deconvolution

Wide field-of-view imaging systems present unique challenges to image restoration of remotely imaged scenes. Common tactical employment of such systems involves imaging paths though the densest regions of the atmosphere, over fairly long horizontal or slant paths to target objects. In such environments, the system FOV can dramatically exceed the tilt isoplanatic (isokinetic) angle, even during modest levels of atmospheric turbulence [55]. Under such circumstances, the statistical imaging model can no longer be accurately described as a shift-invariant system. In contrast, the transmitted image is subject to phase and amplitude distortions that vary as a function of position on the imaging device, due to the wavefront decorrelation that occurs due to the necessarily large FOVs required to image typical scenes-of-interest.

Several approaches have yielded successfully reconstructed images under wide FOV conditions. A novel multiframe processing algorithm is described in [19] that has been shown to effectively mitigate image degradation from coherent speckle and anisoplanatic viewing conditions by iteratively processing subimage regions of a remote scene. It appears that the independent processing of multiple subimages by the modified Ayers-Dainty blind deconvolution algorithm admits improvement for images best described by a spatially variant imaging process. Block matching or image *dewarping* techniques [9, 23, 61], while computationally expensive, attempt to break the shift-invariant problem into several smaller, shift-variant sub-problems. The restored image quality has been shown to vary dramatically as a function of the *isoplanatic patch* size [9]. However, without prior information regarding atmospheric condition, it becomes difficult to determine the number and size of the component patches that comprise the detected image. Computational demands grow rapidly as the number of isoplanatic patches is increased.

Adaptive optic (AO) techniques [33,60,69,79], may be employed to mitigate the effects of atmospheric turbulence in wide FOV systems, however, these techniques are also computationally expensive and require substantial hardware resources. In the

case of anisoplanatic viewing conditions, multiple OTFs corresponding to each iso-planatic patch must be estimated by way of point-source illumination or artificial guide-star creation at or near each of the corresponding points on the remote tar-get [26, 77]. The computational burden of multiple guide-star creation and OTF estimation is prohibitive for application to image reconstruction from small, agile tactical platforms such as manned fighter-reconnaissance aircraft or remotely-piloted vehicles. While the rapid development of micro-electro-mechanical (MEM) devices will certainly revolutionize the fielding of AO systems, solutions that avoid AO archi-tectures and the associated computational burden are more readily applied to space and weight constrained applications in the near term.

This chapter documents the derivation and application of an anisoplanatic OTF (AOTF) based on tip and tilt correlation models of turbulent atmosphere as the kernel function of a maximum *a priori* estimation algorithm used to simultaneously estimate an image of the remote scene together with the atmospheric seeing condition param-eterized by Fried's seeing parameter, r_0. Previous research documented in Chap. III and [54] employed the short-exposure average OTF, $\bar{\mathcal{H}}_{se}$, to model the imaging pro-cess of a series of motion-compensated speckle image frames from a candidate laser vision system. Under this model, the image formation process was considered linear in intensity and shift-invariant in the average of many such motion-compensated im-age frames. However, it was understood that $\bar{\mathcal{H}}_{se}$ was only an approximation to the true average OTF, since additional blur components contributed by the motion of the myriad of isoplanatic patches were not accurately captured in this statistical model. A more accurate OTF would capture these additional blur components and evolve as a function of the FOV that surrounds the scene-of-interest.

This chapter is organized as follows. A brief introduction to the difficulties in-volved with imaging through turbulence with wide FOV systems is given in Sec. 4.1.1. Section 4.1.2 outlines a procedure used to create simulated anisoplanatic partially co-herent speckle imagery that is used to compare to experimentally collected imagery. A simple tilt-only model is presented to describe the additional blur resulting from the

random motion of isoplanatic patches in Sec. 4.1.3, resulting in an improved overall OTF to describe the degradation of the motion-compensated frame average image. Section 4.1.4 presents a model that captures the additional tilt variance as a function of system FOV for a multi-layered turbulence path to be incorporated into an aniso-planatic OTF for use within a blind deconvolution algorithm. In Sec. 4.2, images are reconstructed and seeing conditions are estimated from both simulated and experimental image ensembles, using each the original short exposure OTF and the AOTF for comparison. The results are discussed and the chapter is summarized in Sec. 4.3.

4.1 Anisoplanatic Blur Model

4.1.1 Limitations of the Short Exposure OTF.   The FOV of tactical laser radar imaging systems is necessarily wide, typically exceeding the isoplanatic angle of the atmosphere by a large margin. Such conditions discourage modeling the formation of images using a single OTF due to spatial variance imposed by the atmosphere. However, it has been demonstrated that the expected value of some statistical OTF can accurately model the additional blur induced by the uncorrelated motion of the multitude of isoplanatic patches projected to the imaging detector [23, 69, 72]. Such an OTF must evolve as the system FOV is changed.

In one extreme, system FOV might be made sufficiently narrow that the expected atmospheric effects can be accurately modeled by the average short exposure transfer function introduced in Sec. 2.8 and repeated here for convenience [31]

$$\bar{\mathcal{H}}_{se}\left(\nu\right) = \exp\left\{-3.44\left(\frac{\lambda f \nu}{r_0}\right)^{5/3}\left[1 - \left(\frac{\lambda f \nu}{D}\right)^{1/3}\right]\right\}, \qquad (4.1)$$

where λ is the mean wavelength of the laser illumination, f is the system focal length, ν is a radial spatial frequency variable, D is the diameter of the optical aperture, and r_0 is Fried's seeing parameter or optical coherence diameter. For fixed optical components, the short exposure OTF is completely parameterized by r_0. The short exposure OTF predicts the ensemble average atmospheric image degradation after removal of

image tilt common to the entire imaged scene. The OTF is accurate for an image constructed from a series of perfectly registered (global tilt-removed) image frames, collected from a system with such a narrow FOV that the image transformation process is spatially invariant. However, the short exposure OTF is optimistic (predicts excessive high frequency detail) in the common situation where system FOV begins to exceed the isoplanatic angle imposed by the turbulent atmosphere.

Unfortunately, tactical sensors require a very wide FOV. Typical geometry constraints of tactical sensors require that the optical paths arising from individual points that comprise an extended remote scene pass through distinct parts of the turbulent atmosphere. Figure 1.4 depicts the geometry of a system that experiences anisoplanatic effects. Paths traced from a pair of point sources separated by some distance to the telescope aperture traverse regions of turbulence that possess different indices of refraction and thus tend to delay the optical phase by varying amounts.

Excellent examples of relevant slant-path propagation problems are presented in [55] as well as [79] and [23], where the effects of tilt anisoplanatism are studied in some detail. As a further example, consider the following candidate laser vision scenario. An armored tank, with a maximum lateral extent of 10 meters is viewed from a distance of 10 kilometers using a gated eye-safe laser radar imaging system. The field of view subtends approximately 200 arc seconds (10 milliradians). Further assume a mean optical wavelength of 1.5 micrometers, and a constant turbulence level across an essentially horizontal imaging path of $C_n^2 = 10^{-13} \ m^{2/3}$. The isoplanatic angle of an arbitrary optical system using spherical wave propagation is given by [61]

$$\theta_0(L) = \left[1.09 \left(\frac{2\pi}{\lambda} \right)^2 L^{8/3} C_n^2 \right]^{-3/5}, \tag{4.2}$$

where L is the atmospheric path length. The resulting isoplanatic angle is a mere 0.55 arc seconds (0.28 microradians). Although the tilt isoplanatic angle is roughly an order of magnitude larger than this figure [26], the system FOV remains dramatically larger than the tilt isoplanatic angle. In wide FOV situations the number of tilt

isoplanatic patches may even approach or exceed the number of pixels in the detector array.

4.1.2 Simulation of Image Propagation through Turbulent Atmosphere. Simulation of the anisoplanatic imagery used for comparison to the measured experimental data is described in detail in Sec. 2.1 through Sec. 2.3 but will be briefly reviewed for clarity. The propagation of spherical waves from point sources that compose a target scene is disturbed by the random index of refraction of turbulent eddies within the included atmosphere enroute to the imaging system. The large volume of atmosphere between the target and optical aperture may be modeled as a series of thin phase screens placed at intervals along the propagation path. Due to the large number of turbulent eddies of varying refraction index, the central limit theorem permits the phase delay of each phase screen to be modeled as having a circularly Gaussian distribution of phase delay [35, 38]. Phase screens are approximated as being statistically independent due to physical separation. A single thin phase screen may be constructed by summation of the discrete individual screens while accounting for geometric propagation through each screen [8]. Isoplanatic effects of propagation may be effectively simulated by conducting Rayleigh-Sommerfeld propagation from each point on a target through this single thin phase screen placed at the optical aperture. A coherent system model described in Sec. 2.1 and [8] is used to create speckle images at the imaging detector with the correct spatio-temporal coherence. The composite thin-phase screen disturbs independent realizations of speckle images in accordance with the desired level of atmospheric turbulence. Note that in order to simulate anisoplanatic viewing conditions, a composite thin phase screen must be created for each point propagated from the target to the aperture.

4.1.3 Optical Tilt Effects Induced by Atmospheric Turbulence. Tip and tilt effects imposed by the turbulent atmosphere cause the majority of image blur in the averaged intensity of the detected image ensemble. Excluding piston effects, roughly 89% of the turbulence distortion power is contained in Zernike coefficients Z_2

and Z_3 [60]. The accurate spatial registration of a series of short-duration exposure speckle images yields an average image created by a spatially invariant system model characterized by the short-exposure OTF of Eqn. 4.1. However, in those cases where the atmospheric viewing conditions do not permit system description by a spatially invariant model, it becomes necessary to find other methods to quantify image degradation effects. A major component of these unquantified effects is due to the blur induced by averaging images which have significant amounts of local image warping due to anisoplanism. Another source of blur in the averaged image might be due to poor image registration, although this effect is not treated in the following analysis as it is highly dependent on the performance of the image registration algorithm employed. The focus of this section is the development of an expression for an anisoplanatic OTF that captures the expected value of the motion blur resulting from the uncorrelated tilt variance of point sources that originate from the remote target scene

The following analysis is presented to quantify the blur due only to the motion of a point source disturbed by the tip and tilt components of a randomly turbulent atmosphere. Such analysis will allow an elegant description of the blur that results from the decorrelated motion between points sources separated by greater than the anisoplanatic angle. Considering the optical system response to a single target point source located close to the optical boresight, the system may be approximated as shift-invariant. The point spread function, $p(x, y)$ is defined as the linear shift-invariant response of the optical system to the 2-D Dirac delta function, δ

$$p(x, y) = \delta(x, y) \otimes h(x, y) = \iint\limits_{-\infty}^{\infty} h(\xi, \eta)\, \delta(x - \xi, y - \eta)\, d\xi d\eta = h(x, y) \qquad (4.3)$$

where $h(x, y)$ is the instantaneous impulse response of the optical system and $\otimes$ represents the convolution operator. To capture the blurring effects of the atmospheric tip and tilt components exclusively, one may consider that the atmosphere produces a blur by only shifting the location of the point spread function as a function of time.

In this case, the instantaneous PSF is

$$p\left(x,y\right) = \delta\left(x - \alpha\left(t\right), y - \beta\left(t\right)\right), \tag{4.4}$$

where, α and β are random variables that may be explicitly written as a function of time.

By definition, the Optical Transfer Function is simply the Fourier transform of the PSF,

$$\mathcal{H}\left(f_x, f_y\right) = \mathcal{F}\left[h\left(x,y\right)\right] = \int\limits_{-\infty}^{\infty}\!\!\int p\left(x,y\right) e^{-j2\pi\left(f_x x + f_y y\right)} dx dy \tag{4.5}$$

and by substitution with Eqn. 4.4,

$$\mathcal{H}\left(f_x, f_y\right) = \mathcal{F}\left[h\left(x,y\right)\right] = \int\limits_{-\infty}^{\infty}\!\!\int \delta\left(x - \alpha\left(t\right), y - \beta\left(t\right)\right) e^{-j2\pi\left(f_x x + f_y y\right)} dx dy. \tag{4.6}$$

The solution to the integral is trivial due to the properties of the Dirac delta,

$$\mathcal{H}\left(f_x, f_y, t\right) = e^{-j2\pi\left(f_x \alpha(t) + f_y \beta(t)\right)}. \tag{4.7}$$

Due to the large volumes of distributed turbulence between the target and optical aperture, the tip and tilt or *image jitter* experienced at the aperture is commonly assumed to be a zero-mean Gaussian random process [25]. Thus, α and β are independent Gaussian, zero-mean random variables,

$$p_\alpha\left(\alpha\right) = \frac{1}{\sqrt{2\pi}\sigma_\alpha} e^{-\frac{\alpha^2}{2\sigma_\alpha^2}}, \tag{4.8}$$

and

$$p_\beta\left(\beta\right) = \frac{1}{\sqrt{2\pi}\sigma_\beta} e^{-\frac{\beta^2}{2\sigma_\beta^2}}. \tag{4.9}$$

The ensemble average OTF is easily found by joint expectation over α and β,

$$\bar{\mathcal{H}}\left(f_x, f_y\right) = E_{\alpha,\beta}\left[e^{-j2\pi(f_x\alpha+f_y\beta)}\right] = \int\!\!\!\int_{-\infty}^{\infty} e^{-j2\pi(f_x\alpha+f_y\beta)}p_{\alpha,\beta}\left(\alpha,\beta\right)d\alpha d\beta. \qquad (4.10)$$

A further assumption is made that the tip and tilt are mutually independent, thus their joint distribution is separable,

$$\bar{\mathcal{H}}\left(f_x, f_y\right) = \int\!\!\!\int_{-\infty}^{\infty} e^{-j2\pi(f_x\alpha+f_y\beta)}p_{\alpha}\left(\alpha\right)p_{\beta}\left(\beta\right)d\alpha d\beta. \qquad (4.11)$$

By substitution of Equations 4.8 and 4.9 into Eqn. 4.11 the OTF can be written as

$$\bar{\mathcal{H}}\left(f_x, f_y\right) = \frac{1}{\sqrt{2\pi}\sigma_{\alpha}}\frac{1}{\sqrt{2\pi}\sigma_{\beta}}\int\!\!\!\int_{-\infty}^{\infty} e^{-j2\pi(f_x\alpha+f_y\beta)}e^{-\left(\frac{\alpha^2}{2\sigma_{\alpha}^2}+\frac{\beta^2}{2\sigma_{\beta}^2}\right)}d\alpha d\beta, \qquad (4.12)$$

which is easily recognized as the Fourier transform of a pair of jointly independent Gaussian random variables. By use of the appropriate Fourier transform tables [31], it can be shown that

$$\bar{\mathcal{H}}\left(f_x, f_y\right) = \frac{1}{\sqrt{2\pi}\sigma_{\alpha}}\frac{1}{\sqrt{2\pi}\sigma_{\beta}}\left|\sqrt{2\pi\sigma_{\alpha}^2 2\pi\sigma_{\beta}^2}\right|\exp\left[-\pi\left(2\pi\sigma_{\alpha}^2 f_x^2 + 2\pi\sigma_{\beta}^2 f_y^2\right)\right]. \qquad (4.13)$$

Since the variances of the tip and tilt σ_{α}^2 and σ_{β}^2 are always positive, the average OTF reduces to

$$\bar{\mathcal{H}}\left(f_x, f_y\right) = \exp\left[-\left(2\pi^2\sigma_{\alpha}^2 f_x^2 + 2\pi^2\sigma_{\beta}^2 f_y^2\right)\right], \qquad (4.14)$$

which is a radially symmetric Gaussian function due to assumed equal variance in the tip and tilt axes. A similar derivation may be found in the literature [52,80], and the average OTF is often expressed as

$$\bar{\mathcal{H}}\left(u, v\right) = \exp\left[-\left(2\pi^2\sigma_{\alpha}^2\left(\lambda f u\right)^2 + 2\pi^2\sigma_{\beta}^2\left(\lambda f v\right)^2\right)\right], \qquad (4.15)$$

where u and v are spatial frequency variables in the aperture plane, λf is the optical scaling factor for Fresnel propagation to the detector located at a focal length of f meters for a mean optical wavelength of λ, and σ_α^2 and σ_β^2 are tilt variances in the u and v directions respectively.

$\bar{\mathcal{H}}(u,v)$ can be seen to have circular symmetry by letting $\nu = \sqrt{(\lambda f u)^2 + (\lambda f v)^2}$ and by assuming equal variance power in both the u and v coordinate axes. Under these conditions, $\sigma_\alpha^2 = \sigma_\beta^2 = \sigma_A^2$ and

$$\bar{\mathcal{H}}(\nu) = e^{-2\pi^2 \sigma_A^2 \nu^2}. \tag{4.16}$$

The simplified OTF is completely parameterized by the axis-combined tilt variance, σ_A^2. Although derived above for the case of isoplanatic imaging, the Gaussian OTF provides the foundation for the construction of an anisoplanatic OTF. If the Gaussian tilt variance that results from an anisoplanatic imaging process might be derived, this variance may be substituted into the above expression to yield a suitable AOTF [72]. The overall OTF employed to model an ensemble-average of well-registered anisoplanatic imagery is simply the product of the non-random OTF of the optics, the OTF that embodies atmospheric effects after global tilt motion compensation and some OTF that corresponds to the blur introduced by the uncorrelated motion of the many isoplanatic patches,

$$\bar{\mathcal{H}}_{sys}(u,v) = \mathcal{H}_{opt}(u,v)\,\bar{\mathcal{H}}_{se}(u,v)\,\bar{\mathcal{H}}_{AOTF}(u,v). \tag{4.17}$$

The last two terms of Eqn. 4.17 represent the expected OTF that describes the atmospheric imaging system model. The true system model is not spatially invariant for the case of anisoplanatic viewing conditions, however, the system may be considered shift-invariant in the average with the inclusion of $\bar{\mathcal{H}}_{AOTF}(u,v)$ to account for blur effects due to anisoplanatism. A comment on the relationship of this model to the short and long-exposure OTF is appropriate. Assuming no image registration of indi-
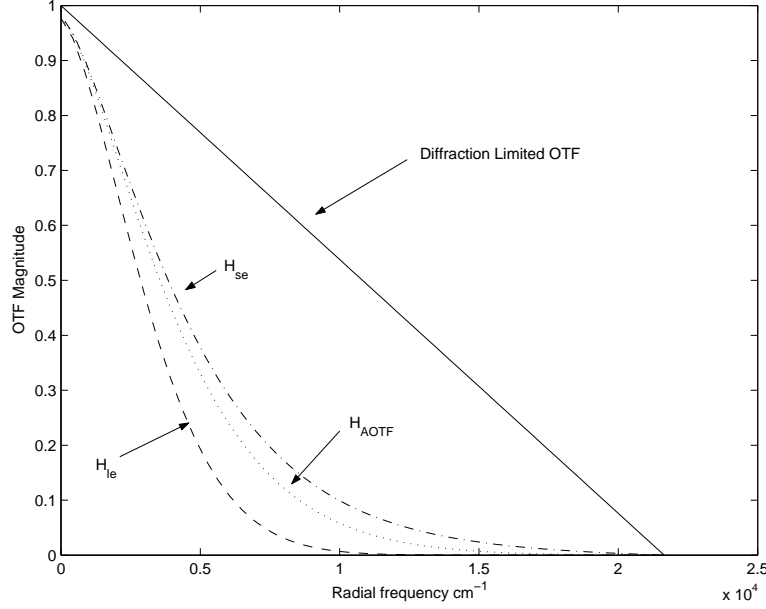
Figure 4.1: Comparison of long-exposure, short-exposure and anisoplanatic OTFs with $D/r_0 = 5$. The long-exposure OTF models an image created by averaging a series of atmospherically distorted images without the benefit of tip and tilt removal. The higher spatial frequencies evident in the short-exposure OTF are a direct result of such motion compensation for images collected with a spatially invariant optical system. In systems that are spatially variant due to anisoplanatic effects, high frequency detail is lost due to the summation of many uncorrelated anisoplanatic patches within each image, resulting in an OTF that is conditioned on the degree of anisoplanatism.

vidual images within the ensemble, an accurate system model would replace the last two terms of Eqn. 4.17 with the long-exposure OTF [31]. Such an OTF would have very little high frequency content, due to considerable blur imposed by global motion of each ensemble image. After global image registration, dramatic high frequency spatial detail is gained, however, not as much as if the viewing conditions permitted spatially invariant image formation. Thus, the OTF most applicable to the actual anisoplanatic viewing condition lies somewhere between the short and long-exposure OTF, as depicted in Fig. 4.1.

4.1.4 Tilt Variance as a Function of Geometry. The instantaneous displacement φ of an imaged point at the imaging detector in units of meters is the integrated gradient of wavefront phase, normalized by the area of the system aperture [80]

$$\varphi = \frac{\lambda f \int\!\!\int\limits_{-\infty}^{\infty} U\left(r\right) \nabla \phi \; dr}{2\pi \int\!\!\int\limits_{-\infty}^{\infty} U\left(r\right) dr}, \tag{4.18}$$

where $U\left(r\right)$ is the non-zero field over the aperture extent, $\nabla \phi$ is the wavefront phase gradient, and r is the 2-D spatial variable in the plane of the optical aperture. In the simple case of linear gradient or tip/tilt, the gradient can be replaced by an appropriate slope multiplied by the independent variable in either cartesian coordinate axis, u or v.

Considering a series of uniformly spaced thin phase screens as depicted in Fig 4.2, the u-axis wavefront tilt α at the optical aperture in radians from an arbitrary imaged point $P\left(u + \rho_u, v + \rho_v\right)$ on the target displaced from the optical boresight may be synthesized from a normalized, weighted sum of basis vectors

$$\alpha = \frac{\int\!\!\int\limits_{-\infty}^{\infty} \sum\limits_{n=1}^{N} \left(u + \rho_{u_n}, v + \rho_{v_n}\right) A_n\left(u + \rho_{u_n}, v + \rho_{v_n}\right)\phi_n\left(u, v\right) dudv}{\int\!\!\int\limits_{-\infty}^{\infty} uA\left(u, v\right) dudv}, \tag{4.19}$$

where u and v are spatial variables in the aperture in units of meters that correspond to the x and y coordinates in the detector, the random field $\phi_n\left(u, v\right)$ represents the phase of the nth of N phase screens, and $A_n\left(u + \rho_{u_n}, v + \rho_{v_n}\right)$ is the deterministic aperture weighting function geometrically formed by projection from the point source $P\left(u + \rho_u, v + \rho_v\right)$ on the target to the optical aperture plane. ρ_u and ρ_v are the orthogonal components of displacement in meters from optical boresight measured at the target plane. Since the discrete atmospheric phase screens are uniformly spaced, the displacement of the projected apertures from a point $P_1(u_1, v_1)$ at each screen may be found according to the linear relationships $\rho_{u_n} = \frac{z_n}{L}u_1$ and $\rho_{v_n} = \frac{z_n}{L}v_1$ where z_n is the z-axis position of the nth phase screen, and L is the distance from the target to the optical aperture. Typical aperture weighting functions are radially symmetrical
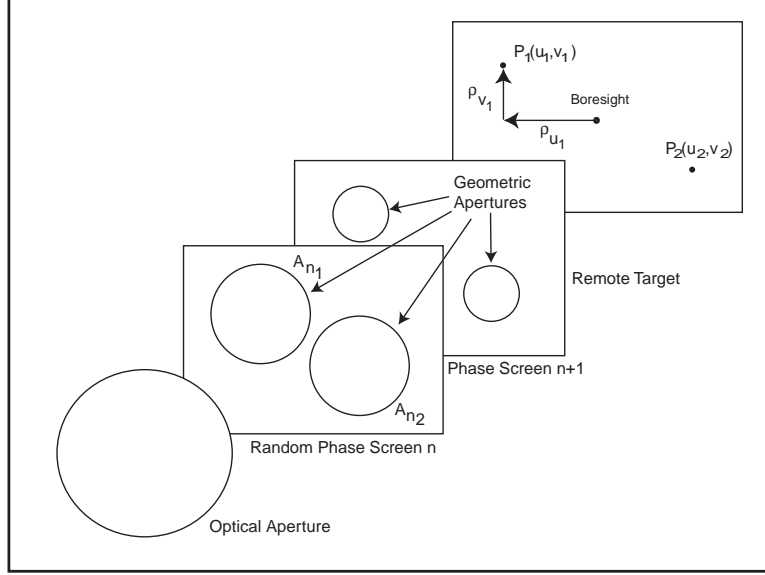
Figure 4.2: Coherent imaging model. Two distinct point sources from the target propagate to the optical aperture through a turbulent atmosphere represented by N thin phase screens uniformly distributed along the path from target to receiver. At each random atmospheric thin phase screen, a projected aperture function is formed by the physical geometry of the point source and receiver location as depicted. The model is used to predict the summed tilt contribution from each point source at the optical aperture.

and have a value of unity within the aperture, and zero outside this region. The denominator of Eqn. 4.19 serves to normalize tilt magnitude with reference to the aperture weighting function of the optical system, $A(u,v)$.

Heuristically, the tilt measured at the optical aperture for a given point on the target may be understood to be composed of two components. One component is a global tilt which may be effectively removed by accurate image registration. The second component is local tilt due to anisoplanatic viewing conditions. Note that these two components are independent, since any global tilt that might exist in the local tilt component would be removed by global image registration. Therefore, the composite tilt α may be written as $\alpha = \alpha_c + \alpha_u$, where α_c and α_u are the spatially correlated and uncorrelated tilt components respectively. Considering a pair of arbitrary points on a target, it may easily be shown that their uncorrelated tilt variance $E[\alpha_u^2]$ is the residual variance calculated by subtracting the correlated tilt variance from the total

tilt variance,

$$E[\alpha_u^2] = E[\alpha^2] - E[\alpha_1\alpha_2], \tag{4.20}$$

where $E[\alpha^2]$ is the overall tilt variance of either of the points at the aperture and $E[\alpha_1\alpha_2]$ is the correlated tilt power between the two points.

It is instructive to first compute the aperture tilt covariance $E[\alpha_1\alpha_2]$ resulting from two distinct points on the target, $P_1(u_1, v_1)$ and $P_2(u_2, v_2)$. $E[\alpha_1\alpha_2]$ will depend only on point separation if the atmospheric turbulence can be considered isotropic. For a fixed level of atmospheric turbulence, more distant points on the target will produce less correlated tilt power at the aperture. On the other hand, two closely spaced points, subtending an angle well within the tilt isoplanatic angle for a given turbulence level, will yield essentially no uncorrelated tilt variance $E[\alpha_u^2]$.

Calculation of the tilt covariance of two arbitrary points is mathematically straightforward. It is convenient to fix one point at the optical boresight of the target, while locating the second point at a distance of ρ_u and ρ_v in the u and v directions respectively. The u-axis tilt covariance at the aperture is then

$$E[\alpha_1\alpha_2] = \psi \int\!\!\!\int\!\!\!\int\!\!\!\int_{-\infty}^{\infty} \sum_{n_1=1}^{N} \sum_{n_2=1}^{N} E\Big[uA_{n_1}(u,v)\, \phi_{n_1}(u,v)$$

$$\left(u' + \rho_{u_{n_2}} \right) A_{n_2}\left(u' + \rho_{u_{n_2}}, v' + \rho_{v_{n_2}} \right)$$
$$\phi_{n_2}(u', v')\, du\, dv\, du'\, dv' \Big], \tag{4.21}$$

where

$$\psi = \left(\int\!\!\!\int_{-\infty}^{\infty} uA(u,v)\, du\, dv \right)^{-2} \tag{4.22}$$

is the scalar normalization constant formed by integration over the extent of the u-axis *tilted aperture* in the plane of the optical receiver.

As is common in the literature, the individual phase screens are taken to be statistically independent zero-mean random Gaussian fields, therefore,

$$E\left[\phi_{n_1}\left(u_1, v_1\right)\phi_{n_2}\left(u_2, v_2\right)\right] = 0, \quad \forall \; n_1 \neq n_2 \tag{4.23}$$

which results in the cancelation of summation cross-terms. After dropping the subscript on n for convenience, the tilt covariance becomes

$$E\left[\alpha_1\alpha_2\right] = \psi \iiiint\limits_{-\infty}^{\infty} \sum_{n=1}^{N} u A_n\left(u, v\right)\left(u' + \rho_{u_n}\right) A_n\left(u' + \rho_{u_n}, v' + \rho_{v_n}\right)$$

$$E\left[\phi_n\left(u, v\right)\phi_n\left(u', v'\right)\right] du\, dv\, du'\, dv'. \tag{4.24}$$

After making the substitutions of variables, $\tilde{u} = u' + \rho_{u_n} - u$ and $\tilde{v} = v' + \rho_{v_n} - v$, the correlated component of tilt at the aperture may be expressed as

$$E\left[\alpha_1\alpha_2\right] = \psi \iiiint\limits_{-\infty}^{\infty} \sum_{n=1}^{N} u A_n\left(u, v\right)\left(\tilde{u} + u\right) A_n\left(\tilde{u} + u, \tilde{v} + v\right)$$

$$E\left[\phi_n\left(u, v\right)\phi_n\left(u + \left[\tilde{u} - \rho_{u_n}\right], v + \left[\tilde{v} - \rho_{v_n}\right]\right)\right] du\, dv\, d\tilde{u}\, d\tilde{v}, \tag{4.25}$$

and the expected value operation in the integrand may be recognized as an autocorrelation of the nth phase screen, R_{ϕ_n}, which is only a function of $\tilde{u}, \tilde{v}, \rho_{u_n}$ and ρ_{v_n}. This observation allows the quadruple integral to be split into a pair of double integrals

$$E\left[\alpha_1\alpha_2\right] = \psi \sum_{n=1}^{N} \iint\limits_{-\infty}^{\infty} R_{\phi_n}\left(\tilde{u} - \rho_{u_n}, \tilde{v} - \rho_{v_n}\right)$$

$$\left\{\iint\limits_{-\infty}^{\infty} u A_n\left(u, v\right)\left(\tilde{u} + u\right) A_n\left(\tilde{u} + u, \tilde{v} + v\right) du\, dv\right\} d\tilde{u}\, d\tilde{v}. \tag{4.26}$$

The integral within the braces of Eqn. 4.26 is the 2-D autocorrelation of the nth tilted aperture function. Let this quantity be represented by $G_{u_n}(\tilde{u}, \tilde{v})$. Then,

$$E\left[\alpha_1 \alpha_2\right] = \psi \sum_{n=1}^{N} \iint_{-\infty}^{\infty} R_{\phi_n}\left(\tilde{u} - \rho_{u_n}, \tilde{v} - \rho_{v_n}\right) G_{u_n}\left(\tilde{u}, \tilde{v}\right) d\tilde{u} d\tilde{v}. \qquad (4.27)$$

It is now necessary to quantify the tilt variance of an arbitrary point in the scene, $E[\alpha^2]$. Similar analysis is presented in the literature, e.g. [3]. For the case of tilt variance of a given point at the target, there exists no displacement between point sources at the target, i.e., $\rho_{u_n} = 0$ and $\rho_{u_v} = 0, \quad \forall\, n \in N$, and the uncorrelated tilt at the aperture may be found by substitution of $E[\alpha^2]$ into Eqn. 4.20,

$$E\left[\alpha_u^2\right] = \psi \sum_{n=1}^{N} \iint_{-\infty}^{\infty} \left[R_{\phi_n}\left(\tilde{u} - 0, \tilde{v} - 0\right) - R_{\phi_n}\left(\tilde{u} - \rho_{u_n}, \tilde{v} - \rho_{v_n}\right)\right] G_{u_n}\left(\tilde{u}, \tilde{v}\right) d\tilde{u} d\tilde{v}. \qquad (4.28)$$

The structure function may be expressed as $D_{\phi_n}\left(\rho\right) = 2\left(R_{\phi_n}\left(0\right) - R_{\phi_n}\left(\rho\right)\right)$ for an isotropic turbulent atmosphere, where ρ represents radial separation between points on a thin phase screen. After adding and subtracting $R_{\phi_n}\left(0, 0\right)$ to both terms within the integrand, the uncorrelated tilt may be written

$$E\left[\alpha_u^2\right] = \frac{\psi}{2} \sum_{n=1}^{N} \iint_{-\infty}^{\infty} \Lambda_{\phi_n}\left(\tilde{u} - \rho_{u_n}, \tilde{v} - \rho_{v_n}\right) G_{u_n}\left(\tilde{u}, \tilde{v}\right) d\tilde{u} d\tilde{v}. \qquad (4.29)$$

where

$$\Lambda_{\phi_n}\left(\tilde{u} - \rho_{u_n}, \tilde{v} - \rho_{v_n}\right) = \left\{D_{\phi_n}\left(\tilde{u} - \rho_{u_n}, \tilde{v} - \rho_{v_n}\right)\right\} - \left\{D_{\phi_n}\left(\tilde{u}, \tilde{v}\right)\right\}. \qquad (4.30)$$

An identical derivation can be used to find the transverse component of tilt. A more useful form of the uncorrelated tilt power can be found by summing the orthogonal components of tilt variance in each axis. Assuming symmetry of the

optical aperture in both the u and v axes, the combined total uncorrelated tilt power is then

$$E\left[\tau_u^2\right] = \psi \sum_{n=1}^{N} \iint\limits_{-\infty}^{\infty} \Lambda_{\phi_n}\left(\tilde{u} - \rho_{u_n}, \tilde{v} - \rho_{v_n}\right)\left\{G_{u_n}\left(\tilde{u}, \tilde{v}\right) + G_{v_n}\left(\tilde{u}, \tilde{v}\right)\right\} d\tilde{u}d\tilde{v}. \qquad (4.31)$$

By allowing $\rho_n = \sqrt{\rho_{u_n}^2 + \rho_{v_n}^2}$ and recognizing the radial symmetry of the summed tilted aperture correlation functions, $G_n(\tilde{u}, \tilde{v}) = G_{u_n}\left(\tilde{u}, \tilde{v}\right) + G_{v_n}\left(\tilde{u}, \tilde{v}\right)$, the uncorrelated tilt may be expressed as in integral over polar coordinates r and θ,

$$E\left[\tau_u^2\right] = \psi \sum_{n=1}^{N} \int\limits_{\theta} \int\limits_{\rho} \Lambda_{\phi_n}\left(r - \rho_n\right) G_n\left(r\right)\ r dr d\theta. \qquad (4.32)$$

The phase structure function noted in Eqn. 4.30 may be most simply modeled by using Kolmogorov statistics, with the important limitation that the effects of turbulence are constrained to some inertial subrange such that turbulent eddy sizes are bounded by the upper and lower scale values L_0 and l_0 respectively [1]. Then,

$$D_\phi\left(\rho, z_n\right) = 2.91 k^2 \rho^{5/3} \int_0^{z_n} C_n^2\left(z\right) \left(\frac{z}{z_n}\right)^{5/3} dz, \qquad l_0 \ll \rho_0 \ll L_0. \qquad (4.33)$$

Assuming constant C_n^2 profile as might be encountered during a horizontal path imaging scenario, Eqn. 4.33 reduces to

$$D_\phi\left(\rho, z_n\right) = 1.09 C_n^2 z_n k^2 \rho^{5/3}, \qquad l_0 \ll \rho_0 \ll L_0, \qquad (4.34)$$

where the spherical coherence radius is $\rho_0 = \left(0.55 C_n^2 z_n k^2\right)^{-3/5}$, and $k = \frac{2\pi}{\lambda}$. For each phase screen, the length z_n is the extent of the nth atmosphere encompassed by the screen in the z-axis.

Substituting the Kolmogorov phase structure function from Eqn. 4.34 into Eqn. 4.32 and expressing Fried's parameter for spherical wave propagation as

$$r_o = \left[\frac{4\pi^2}{k^2 C_n^2 \frac{3}{8} z_n} \right]^{3/5},$$
(4.35)

a form of Eqn. 4.32 more suitable for use within the parameterized blind deconvolution algorithm is

$$E\left[\tau_u^2\right] = 11.627\pi^2 \psi r_0^{-5/3} \sum_{n=1}^{N} \int_{-\pi}^{\pi} \int_0^{\infty} \left[(r - \rho_n)^{5/3} - r^{5/3} \right] G_n(r) \, r dr d\theta,$$
(4.36)

where $E\left[\tau_u^2\right]$ is the uncorrelated angular tilt variance at the optical aperture expressed in units of square radians.

One final simplification may be realized due to the radial symmetry of the integrand, with the expression reduced to a single integral after integration over θ,

$$E\left[\tau_u^2\right] = 23.254\pi^3 \psi r_0^{-5/3} \sum_{n=1}^{N} \int_0^{\infty} r \left[(r - \rho_n)^{5/3} - r^{5/3} \right] G_n(r) \, dr,$$
(4.37)

As expected, for a target point $P_2(u_2, v_2)$ located along optical boresight (i.e., $|\vec{\rho}_n| = 0$), the uncorrelated tilt variance is zero, and all of the tilt power between the two points is correlated. The numerically computed uncorrelated tilt of a point as it is displaced from the optical boresight for a particular anisoplanatic viewing geometry and range of atmospheric conditions is calculated according to Eqn. 4.37 and plotted in Fig. 4.3.

The radially symmetric integrand of Eqn. 4.37 that results from the multiplication of the auto-correlation of the tilted aperture functions $G_n(r)$, with the displaced structure function $\Lambda_{\phi_n}(r - \rho_n)$ is only a function of the imaging system geometry given a particular thin phase screens location, and may be pre-computed in an off-line system for various target engagement ranges. A fast look-up table approach would obviate the need for calculation of the 2-D cross correlations of the tilted aper-
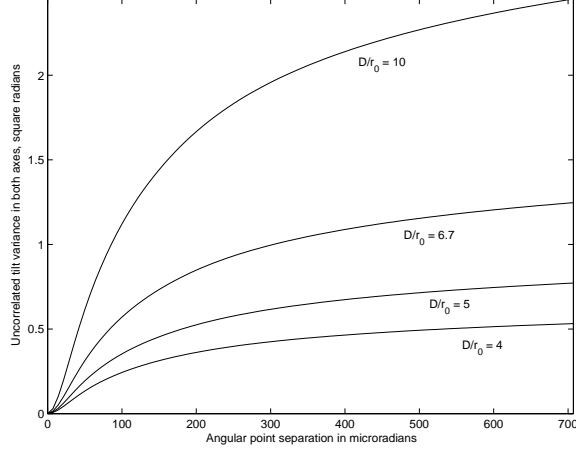
Figure 4.3:   Uncorrelated tilt variance as a function of angular point separation. The total uncorrelated tilt variance is plotted as a function of point separation in the target plane for several values of r_0. The optical aperture is 20 cm, and range to target is 10 km.

ture functions in a real-time environment. The numerical calculation of the aperture auto-correlation $G_n(r)$ is required only at a single phase screen, and may be linearly scaled for the remaining screens. As an alternative to numerical calculation of the integral in Eqn. 4.37, $G_n(r)$ should be easily computed in closed analytical form, given relatively simple aperture geometries [63]. Figure 4.4 shows an example tilted correlation function for the common case of a uniform circular aperture weighting function.

The well-behaved nature of the structure function in the limit as $|\vec{\rho}_n|$ approaches zero allows the use of any of the common atmospheric models, including Kolmogorov, von-Karman, modified von-Karman [38], etc. However, an important limitation of the expression when used for turbulence strength estimation is the requirement to assume constant C_n^2 as a function of distance to the target. Such an assumption allows compact parameterization of the seeing condition using spherical r_0 and is often made for horizontal and moderate slant-path imaging as is typically encountered in the tactical observation environment.
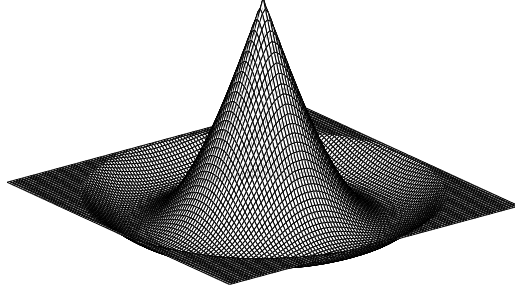
Figure 4.4:   2-D autocorrelation of a tilted circular aperture weighting function. This *Witch's Hat* function was created by the sum of the u-axis tilted autocorrelation function with that of the v-axis tilted function.

4.1.5   Anisoplanatic OTF for Wide FOV Systems.   The analysis conducted in Sec. 4.1.4 describes the uncorrelated tilt power at the optical aperture due to a single point source on the target separated by some distance $|\vec{\rho}_n|$ from the optical boresight. Clearly, larger FOV systems will be best described by AOTFs that incorporate greater uncorrelated tilt variance. To achieve an appropriate OTF, a suitable point separation must be chosen to capture the expected uncorrelated blur effects that span the system FOV. An argument can be made to select a radial point separation equal to the radius of the system FOV. Such a choice yields an OTF that predicts the maximum amount of uncorrelated tilt motion blur in each averaged data frame,

$$\bar{\mathcal{H}}_{AOTF}\left(\nu\right) = e^{-2\pi^2\sigma^2_{A_{FOV}}\nu^2}, \tag{4.38}$$

where

$$\sigma^2_{A_{FOV}} = E\left[\tau_u^2\right] = 23.254\pi^3 f^2\psi r_o^{-5/3}\sum_{n=1}^{N}\int_0^{\infty} r\left[\left(r - \rho_{FOV_n}\right)^{5/3} - r^{5/3}\right]G_n\left(\rho\right)dr \tag{4.39}$$

is obtained from Eqn. 4.37 with $\rho_n = \rho_{FOV_n}$. Here, $\sigma^2_{A_{FOV}}$ is the tilt variance expressed in units of square meters at the detector plane corresponding to the conical field of view described by a point chosen at the furthest extent of the target image under

observation. The scale factor of f^2 is required to transform aperture wavefront tilt variance to image displacement variance at the detector plane.

For a fixed system focal length, an operational user might choose to reduce ρ_{FOV} in order to surround only the "objects of interest" in the overall target scene, allowing a more appropriate OTF for use in a suitable image restoration algorithm.

4.2 Results

A maximum *a posteriori* blind deconvolution algorithm [54] that estimates the remote scene image together with the atmospheric seeing condition was used to process both simulated and experimentally collected data. The MAP algorithm is briefly reviewed in Sec. 4.2.2. As noted in Chap. III, the short exposure OTF was employed to form a MAP estimate for Fried's seeing parameter, r_0. Although image detail was restored relative to the motion-compensated frame average image data input to the routine, it was understood that the additional blur introduced by anisoplanatic patch motion was not properly modeled via the short exposure OTF of Eqn. 4.1.

This section compares the recovered seeing parameters and images obtained using the improved AOTF to those estimated using the short-exposure OTF. Section 4.2.1 documents the procedure used to create the simulated data and the method used to extract atmospheric truth from the experimentally collected data. Section 4.2.3 outlines the compared results using simulated wide FOV speckle image data, while Sec. 4.2.4 documents the comparison for experimentally collected data obtained from an optical range located at North Oscura Peak, White Sands Missile Range (WSMR), New Mexico.

4.2.1 Experimental Method.   To quantify the improvement of r_0 estimation over a broad range of seeing conditions, simulated anisoplanatic 10-Kilometer laser radar data were generated and processed using both the short exposure OTF and the improved anisoplanatic OTF. The simulated image data consisted of a subsection of a standard resolution board target with a system FOV that greatly exceeded the tilt

isoplanatic angle of the simulated turbulent atmosphere for various levels of Fried's seeing parameter. Experimentally collected data consisted of five large ensembles of speckle imagery of a standard resolution target and step-contrast target located at a range of 10 km from the laser vision system.

  4.2.1.1 Synthetic Imagery Generation. Prior to consideration of atmospheric effects, simulated image data were generated to capture the effects of partially coherent laser illumination of a remote scene. The spatio-temporal coherence properties of a gated laser illuminator may be effectively characterized by a scalar speckle parameter, $\mathcal{M}$. The parameter may be mathematically regarded as the degree-of-freedom parameter of the negative binomial distribution used to describe the detection of coherent illumination at the detector [31]. Note that in the limit as $\mathcal{M}$ grows without bound, the negative binomial distribution tends toward the familiar Poisson distribution often used to model incoherent illumination. Physically, $\mathcal{M}$ may be understood to represent the degree of illuminator stability over an observed gating period. Laser illuminators possessing large speckle parameters have less coherence and detected images tend to have less laser-speckle.

  A perfectly coherent plane wave was assumed incident on the target. The target coordinates were assigned such that the target depth along the axis of propagation varied uniformly with a variance of 10 optical wavelengths. Such target roughness caused optical phase interference and yielded a completely developed intensity speckle pattern at the detector subject to the diameter of the optical aperture. Images produced from a system with shorter coherence times were simulated by averaging several fully developed speckle images. As an example, a simulated image collected from a laser system found to have a speckle parameter of $\mathcal{M} = 60$ requires the generation and summation of 60 fully developed speckle images, each created with different uniformly distributed random surface roughness. Table 4.1 lists the salient parameters used to conduct the simulation.

Table 4.1:   This table describes the simulation parameters used to create the aniso-planatic turbulence degraded imagery used to recover Fried's seeing parameter by way of blind image deconvolution.

Parameter	Value
Slant Range to Target	10 Kilometers
Optical Diameter	20 Centimeters
Number of Phase Screens	10
Distance Between Phase Screens	1 Kilometer
Speckle Parameter of Source	60
Pixels per Image	128 by 128
Pixel Pitch of Detector	11.8 micrometers
Mean Wavelength	1.54 micrometers
Focal Length	3 Meters
Images per Frame Ensemble	50
Size of Imaged Target Area	5 by 5 Meters

To capture the deleterious effects of the turbulent atmosphere, the 10-kilometer propagation path was divided into ten, 1-kilometer atmospheric volumes. Statistically independent random Gaussian thin phase screens were constructed using a method similar to that documented in [35] and [38] for each of the ten volumes. The phase delay effects for each of the atmospheric volumes were effectively collapsed to a thin phase screen located behind each volume. To capture anisoplanatic effects, the projected sub-apertures for each imaged point were calculated at each of the ten thin phase screens. The optical phase delay through each of these sub-apertures was summed to create a single thin phase screen located at the optical aperture. For each imaged point at the remote target, light was propagated using Rayleigh-Sommerfeld propagation to the optical aperture [8], [54]. To simulate the effect of partially coherent illumination, $\mathcal{M}$ fully developed speckle images were propagated using varying surface roughness for each set of phase screens and averaged to create a single anisoplanatically distorted, partially coherent speckle image.

4.2.1.2   Knife-Edge OTF Estimation from Experimentally Collected Imagery.   The following section provides a review of the knife-edge techniques introduced in Sec. 2.9. A large image set of a step resolution target ground truth was collected by the experimental laser vision system described in Sections 2.4 and 4.2.4. These data were analyzed to produce an estimate of the actual atmospheric seeing conditions. The individual image frames were spatially registered by correlation with a synthetically generated step target. This process allowed accurate motion compensation of the image ensemble. The remaining image blur was then analyzed to estimate the seeing conditions of the atmosphere for the experimentally collected data.

The long path between the imaging system and target makes atmospheric seeing condition measurement difficult using standard scintillometry techniques. To obtain accurate atmospheric truth, a line-spread function was deduced from experimentally collected imagery according to the method described in [78]. Five large sets of image data were considered, each consisting of 300 speckle images. For each data set, the speckle images of a step-contrast target was first registered and then averaged to produce a single, motion-compensated image frame. The spatial gradient in the horizontal direction was computed from this image in order to estimate the derivative of the step response. The derivative of the step response is the impulse response of the system in the horizontal direction [78]. The short exposure impulse response was computed for different values of r_0 between 1 and 20 centimeters in increments of 0.1 centimeters using the model described in Eqn. 2.39 and a diffraction limited optical transfer function convolved with a pixel of the appropriate size [60]. The simulated OTFs were best fit to the data using the least-square error metric. The estimated spherical seeing conditions for each data set are tabulated in Table 4.2.

4.2.2   MAP Blind Deconvolution Algorithm.   A novel blind deconvolution algorithm was previously developed to simultaneously estimate a remote scene together with current seeing conditions [54]. The algorithm was developed using a Bayesian approach under the assumption that the detection of partially coherent illumina-

4-23

tion follows a negative binomial statistical distribution [31]. Under this framework, a likelihood-based cost function was constructed for each pixel of the detected image. An assumption of independent pixel distributions was made, whereby the total likelihood function for the image was formed from the product of the individual distributions. The likelihood cost function was modified by the addition of an assumed prior for the seeing condition. The assumed prior followed a negative exponential distribution, due to the physical observation that atmospheric seeing is seldom extremely better than some average condition and can often be worse. For each value of the seeing condition characterized by Fried's seeing parameter, an iterative maximization of the likelihood was performed. For each specific value of r_0, iterations were continued until the variance of the image decreased to that predicted by the negative binomial distribution. It was found that the algorithm revealed a maximum value of r_0, beyond which the likelihood tended to decrease due to the influence of the negative exponential prior. This estimate for r_0, together with the resulting estimated image, represented a useful solution to the blind deconvolution problem. However, it was understood that the employed deconvolution kernel did not account for the effects of atmospheric anisoplanatism, and tended to provide pessimistic estimates of seeing conditions.

4.2.3 Results Obtained using Simulated Image Data. Five, 1000-image data sets were constructed to simulate atmospheric conditions described by spherical r_o values of 5, 8, 10, 15 and 20 centimeters, for D/r_o values of 5, 2.5, 2, 1.33 and 1.0 respectively. A MAP blind deconvolution algorithm [54] was used to estimate the most probable seeing parameter for each of the averaged images formed from 50-frame ensembles within each data set. The algorithm was run using both the short-exposure OTF and the new AOTF. Iteration was allowed to continue until the variance between the convolved estimated image decreased to the variance of the negative binomial

distribution used to model the statistics of partially coherent light [31]

$$\sigma_K^2 = \bar{K}\left(1 + \frac{\bar{K}}{\mathcal{M}}\right), \tag{4.40}$$

where $\bar{K}$ is the distribution mean and $\mathcal{M}$ is the estimated speckle parameter. A value of $\mathcal{M} = 60$ was estimated from the experimental data and used for the generation of simulated data [54]. The results of the comparison are tabulated in Table 4.2.

Table 4.2: This table describes the simulated and estimated values for Fried's seeing parameter r_0 as estimated using a blind deconvolution algorithm that uses only the short-exposure OTF of Eqn. 4.1 compared to the same algorithm using the total system OTF described by Eqn. 4.17.

Simulated r_0 in cm	estimated r_0 using $\mathcal{H}_{se}$	estimated r_0 using AOTF
5	4.7	5.1
8	7.5	7.8
10	9.6	9.8
15	14.4	14.7
20	19.1	19.7

The additional anisoplanatic blur components modeled by the AOTF increased the accuracy of the estimation of Fried's parameter from 5% mean error to within 2% using simulated imagery.

4.2.4 Results Obtained using Experimentally Collected Image Data. Experimentally collected data was limited to five pairs of 300-image datasets collected for a particular atmospheric condition on a controlled mountain-top optical range. A resolution bar target and a step-intensity target were imaged according to the parameters outlined in Table 3.1. The gated laser imaging camera was located atop the North Oscura Peak site at the White Sands Missile Range, New Mexico. The site elevation was 7993 feet (2436 m) MSL, while the target site (Beck Site) was located at a height of 5060 ft (1542 m) MSL. The slant-path range to target was 10,040 meters. This geometry resulted in a downlook angle of approximately 17 degrees. Weather condi-

tions were extremely dry, with a humidity of 16%. Individual images were collected with a gate time of 12 ns, at a frame collection rate of 10 Hertz. Both targets were arranged such that only slight azimuth change was required to image either target, ensuring similar atmospheric profiles. Additionally, imaging of each pair of target sets was separated in time by less than three minutes. The 10 km optical path to the remote target prevented accurate atmospheric truth using scintillometer measurements. In order to compare results, the atmospheric seeing condition of the experimentally imaged step-intensity target was estimated using the knife-edge OTF estimation technique described in Sec. 4.2.1.2. Wind speed was recorded in excess of 35 meters per second at the optical aperture, validating the assumption of independent turbulence realizations for each of the 10 Hertz frame rate speckle images.

Blind deconvolution of motion-compensated frame averages of the five resolution bar target data sets was performed using the MAP algorithm briefly described in Sec. 4.2.2. The estimated seeing conditions were compared for both the short-exposure OTF and the new AOTF system models for each data set. These figures were compared to atmospheric truth estimates derived from the knife-edge estimation technique outlined in Sec. 4.2.1.2, and tabulated in Table 4.3.

Table 4.3:   Table describing the estimated values for Fried's seeing parameter r_0 for experimentally collected imagery as estimated using a knife-edge OTF technique, as well as a blind deconvolution algorithm that uses only the short-exposure OTF of Eqn. 4.1 compared to the same algorithm using the total system OTF described by Eqn. 4.17.

Knife-Edge r_0 in cm	estimated r_0 using $\mathcal{H}_{se}$	estimated r_0 using AOTF
3.9	3.6	3.8
4.1	3.4	3.7
4.6	4.3	4.7
3.2	3.0	3.2
3.6	3.4	3.6

Fig. 4.5 shows a representative 10 km motion-compensated frame-average image of the resolution bar target as input to the algorithm, while Fig. 4.6 (a) shows the
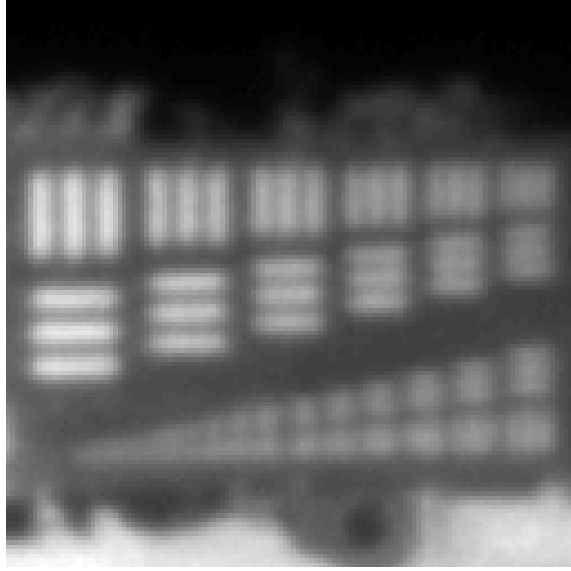
Figure 4.5: Motion-compensated frame average (MCFA) image created from 50 frames of experimentally collected laser radar data for input to the MAP blind deconvolution algorithm. The seeing condition estimated using knife-edge techniques was found to be $r_0 = 3.9$.

result of deconvolution using the short exposure transfer function. Figure 4.6 (b) illustrates the same image deconvolved using the improved AOTF system model.

The additional anisoplanatic blur components modeled by the AOTF increased the accuracy of the estimation of Fried's parameter from 8.6% mean error to within 2.9% using experimentally collected image data.

4.3   Conclusions and Discussion

The results presented in Tables 4.2 and 4.3 indicate that blind deconvolution estimation of r_0 was slightly pessimistic (poorer seeing condition) when only the short-exposure average OTF was assumed for a valid imaging model. The inclusion of the AOTF into the system OTF tended to yield less pessimistic estimates of the seeing parameter that were closer to truth conditions for both the synthetic and experimentally collected imagery. The addition of an anisoplanatic related uncorrelated blur component to the deconvolution kernel appears to increase the accuracy of estimated
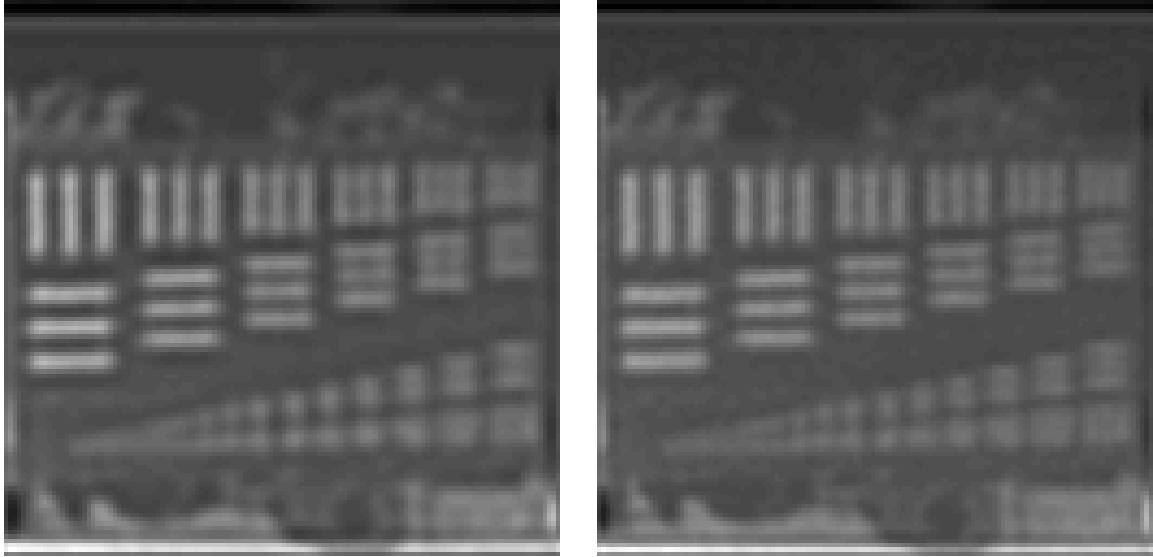
(a) Isoplanatic MAP estimate image of experimentally collected laser radar image data

(b) Anisoplanatic MAP estimate image of experimentally collected laser radar image data

Figure 4.6:   Comparison of the MAP estimated image using the isoplanatic and anisoplanatic deconvolution kernel functions. Subfigure (a) is MAP estimate image of experimentally collected laser radar image data using short-exposure OTF only. Estimated $\hat{r}_0 = 3.6$. Subfigure (b) is the MAP estimate image of experimentally collected laser radar image data using combined anisoplanatic system model of Eqn. 4.17. Estimated $\hat{r}_0 = 3.8$. Note slightly increased image detail that is apparent in the smaller bar patterns compared to Subfigure (a).

seeing condition over a fairly broad range of simulated seeing conditions, as well as at least a limited range of seeing conditions in the case of experimentally collected data.

The additional accuracy gained by improved estimation of atmospheric conditions might be beneficial in many types of imaging applications. For example, a novel seeing monitor might be constructed that requires only the collection of random images with sufficiently high spatial frequency content, rather than specific test patterns designed to assist the seeing monitor. It should be noted that the derived AOTF is not limited to coherent imagery, and the estimation algorithm outlined in [54] is equally applicable to incoherent imagery if slightly modified to estimate Poisson statistics rather than the negative binomial statistics of partially coherent laser illumination.

V. Weighted Averaging of an Ensemble of Collected Image Frames

The research described in previous chapters has introduced novel techniques for remote scene and atmospheric seeing condition estimation. To use the methods described, several short duration images collected by a suitable coherent vision system must be combined in order to reduce the deleterious effects of atmospheric and coherent speckle. The need to combine multiple frames of image data introduces the question of how best to effect this combination. In one extreme, the image processor might choose to simply average some number of available images without regard to translational image alignment or registration. Without such registration, the composite image may be considered the resultant output of an optical system well described by the long-exposure OTF [31].

Image registration dramatically increases high spatial frequency image detail in the resulting average image by reducing globally distributed motion blur due to camera platform vibration or tilt and tip components of a turbulent atmospheric viewing path. In the case where viewing conditions are isoplanatic, the optical system can be described as shift invariant, and almost all such motion blur can be removed from the averaged image given a sufficiently robust image registration algorithm. The resulting average image may be considered the product of a shift-invariant optical system with an OTF well described using the short-exposure OTF [31]. However, there exist fundamental as well as practical limitations to the overall image improvement realized by image registration [58]. Given such limitations, it is clear that some level of global motion blur will remain in the composite image.

In addition to the image degradation caused by unresolved global spatial registration, there exists the problem of local subimage blur due to the effects of anisoplanatism. Such effects were the subject of study in Chapter IV. Due to the shift-variant system model that describes individual image frame formation through a wide FOV optical system operating in a turbulent atmospheric environment, global image registration techniques are inadequate to deal with the isolated and relatively uncorrelated

motion of the myriad of isoplanatic patches that comprise each image frame. In cases of heavy turbulence, individual frames may become severely *warped* or distorted due to the shift-variant imaging system. The inclusion of such frames into the ensemble average image will manifest as image blur, since individual frames are statistically uncorrelated, and the turbulent motion of the atmosphere yields many such frames with distinctly warped image areas.

This chapter supplements the research presented in prior sections by seeking a useful method whereby the effects of such outlier frames are minimized. A brief background of frame selection for optical systems and outlier detection in registration algorithms is presented in Sec. 5.2. A cost function is developed using maximum likelihood estimation theory in Sec. 5.3 that quantifies the admissibility of a particular frame to the overall ensemble frame average. The likelihood function is maximized using an iterative algorithm and compared to a simpler model of the imaging process that admits a direct solution of the maximization problem. The research leads to an elegant binary hypothesis that may be used to discard frames from the ensemble depending on a simple likelihood ratio test. The outlier estimator performance is demonstrated using both synthetically generated as well as experimentally collected image data in Sections 5.5 and 5.6. The resulting development allows for significant image enhancement in cases where atmospheric distortion and image registration deficiencies cause degradation in the frame average image, as discussed in Sec. 5.7.

5.1 *Image Improvement by Averaging an Ensemble of Registered Speckle Image Frames*

Considering the problem of image reconstruction from a sequential series of short time-gated exposures from a coherent laser imaging system, accurate translational registration is a critical initial requirement due to the atmospheric tip and tilt that is characteristic of long viewing paths to the target scene, as well as motion and vibration encountered by the imaging platform. Accurate frame registration permits the subsequent reduction of image speckle, a significant concern for coherent imaging

systems that use illuminating sources with long coherence times. In addition to laser speckle, the atmospheric turbulence between the target and imaging system causes individual ensemble frames to become heavily corrupted by speckle due to the various phase delays imparted by the non-uniform atmospheric index of refraction. To further complicate the problem, long distance viewing often results in very low photon counts despite employment of high-powered illuminating laser sources. The summation of several, well-registered image frames is often mandatory to increase image SNR and reduce image speckle.

The individual images returned from a coherent imaging system over long propagation paths with long illuminator coherence times are typified by high levels of speckle and large intensity variance. Figure 5.1 shows a cropped 128x128 pixel portion of a single image of a resolution bar target board collected by an experimental laser-vision system at a range of approximately 10 kilometers. Typical imaging systems permit frame rates in the tens of Hertz, producing image ensembles ranging from 10 to perhaps 100 images over some acceptably short dwell period. As is evident from Fig 5.1, speckle and intensity variance makes automated image registration difficult. However, the method of fast vector projection correlation has been applied to this problem with remarkable success [7, 53]. Figure 5.2 illustrates the improvement gained by automatically registering and averaging an ensemble of 50 image frames collected under the same conditions as shown in Fig 5.1.

Correlation-based registration processing is not without occasional error, since estimation of the shift parameters for some frames in the ensemble may be hampered by false correlation peaks. Such is often the case when specular glint in a particular frame erroneously correlates with actual bright features in the remote scene image. This effect may be noted by the high-intensity return in the lower corner of Fig. 5.2, where a false correlation peak occurred due to a bright specular return from an off-screen portion of the image. In such cases, it is important to recognize that a registration error has indeed occurred, and that steps are taken to either re-register
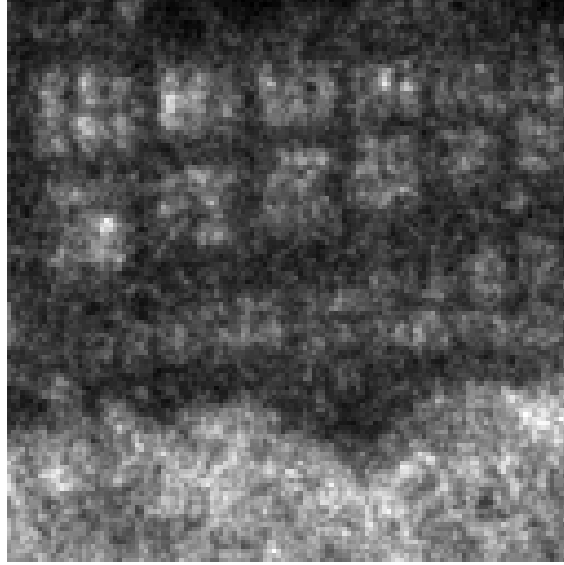
Figure 5.1: Intensity image formed from a single frame of reflected coherent light from a resolution board target collected at an experimental optical range from a distance of 10 kilometers.

the frame or to deemphasize the contribution of the frame to the ensemble average image.

5.2 Background

This research uses a maximum likely (ML) formulation to establish weighting coefficients for individual frames in a multi-frame image ensemble. Several research teams have considered ML techniques for the development of novel and robust image registration algorithms [11,17,32,39,81,82]. Although considerable research has been conducted to develop new and enhanced image registration algorithms, the literature is sparse with general techniques that quantify the goodness-of-fit of a particular image frame relative to the average image. Several Bayesian treatments of outlier detection within the general context of image processing are available [27,34], however, these methods assume statistical models which are not necessarily applicable to the random processes that govern the detection of coherent illumination through a non-uniform atmosphere.
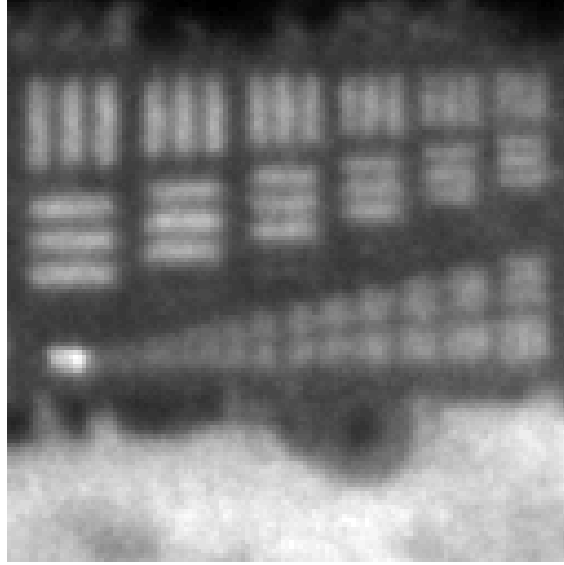
Figure 5.2:   Frame average of 50 consecutive image frames collected at an experimental optical range from a distance of 10 kilometers. Although substantial improvement is evident when compared to Fig. 5.1, registration error may be noted by the bright specular return error that is seen in the lower left corner of the target board. These errors are caused by false correlation peaks due to a bright specular return from the door handle of the supporting truck (off-screen to left). Some vertical ghosting of the upper bars is also evident.

Fried realized that the probability of obtaining accurate, high spatial-frequency images from an optical system decreases exponentially as the ratio of the optical aperture diameter to the seeing parameter (D/r_0) increases [25]. Several researchers have subsequently attempted to establish frame selection performance limits for enhancement of reconstructed imagery [22,59], and they offer a series of image quality metrics that may be used to compare images retrieved from an optical system. However, no significant research can be found that describes likelihood-based methods to identify which frames should be considered candidates for removal from the ensemble before averaging.

It was shown in Sec. 2.6.1 that the pixel intensity distribution along a series of temporally separated image frames gathered from a partially coherent illumination system follows a Negative Binomial (NB) random process [31]. This distribution may be understood to be a more general treatment of the Poisson intensity process com-

monly applied to the case of incoherent illumination. As demonstrated in Sec. 2.6.1, the summation of many frames of NB distributed intensity data result in images that are also governed by a NB process with increased speckle parameter $\mathcal{M}$. Using this physically based statistical model of partially coherent illumination, one may construct a Bayesian estimator that yields a likelihood function for the weight of each image in a series of independently collected image frames within a temporally contiguous ensemble. It should be pointed out that the coherence times of candidate laser illumination systems, while long compared to incoherent sources, is actually rather short compared to the frame rate of typical laser-vision systems. Typical coherence times of laser systems are measured in the nanosecond to microsecond range, while frame collection frame rates are on the order of 10-30 Hertz. Very small changes in angle between the target and camera due to platform motion or atmospheric turbulence cause almost complete decorrelation between images collected during each frame period. To a very good approximation, individual frames gathered by such systems may be treated as statistically independent realizations of the underlying noise process.

The development of an estimator for the relative weights that might be assigned to individual short-exposure images is based on the inherent distinction between image degradation that occurs due to the coherent imaging process versus that caused by anisoplanatic image warping or poor image frame registration. Although difficult to identify due to the lack of *a priori* knowledge of the remote scene and atmospheric seeing conditions, it may be assumed that the intensity distribution of individual pixels due to image warping or mis-registration does not follow a NB distribution. A possible exception to this assumption might occur for the case of imaging a scene of uniform reflectance. However, for the vast majority of interesting cases, there exists no mechanism to cause one to believe that such a distribution would be governed by a NB noise process in the more general case. Under this framework, it is easy to understand why the likelihood of an individual image might be assigned a lower value in those cases where warping or mis-registration has occurred. If no such image

degradation exists, a candidate frame will be well modeled by the statistics of the NB process, and the assigned likelihood will be relatively high.

5.3   *Frame Weight Estimator Development*

A series of J images is collected by a system that propagates highly coherent light towards a target scene through a volume of turbulent atmosphere and reflects from the target back to the optical receiver aperture as discussed in Sec. 2.1. A physically motivated model for the statistical variation of pixel intensity measured in photons is negative binomial [31],

$$P(K) = \frac{\Gamma(K + \mathcal{M})}{\Gamma(K+1)\Gamma(\mathcal{M})} \left[1 + \frac{\mathcal{M}}{\bar{K}}\right]^{-K} \left[1 + \frac{\bar{K}}{\mathcal{M}}\right]^{-\mathcal{M}}, \qquad (5.1)$$

where $\bar{K}$ is the mean photon count, $\mathcal{M}$ is the *speckle parameter*, and K is the random photon count at the detector. Let $K = d_j(x - \hat{\alpha}_j, y - \hat{\beta}_j)$, the number of photons arriving at the detector for each pixel for the jth detected image in the ensemble. Here, $\hat{\alpha}_j$ and $\hat{\beta}_j$ are the previously estimated shifts for each of the J image frames in the ensemble according to some arbitrary registration algorithm.

In order to incorporate the effects of frame weighting within an ensemble of images, the mean pixel intensity may be modeled as the weighted average of each of the ensemble images shifted according to the estimated registration components, $\hat{\alpha}_j$ and $\hat{\beta}_j$. Let $\bar{K} = i(x, y)$, defined mathematically as

$$i(x, y) = \frac{1}{J} \sum_{n=1}^{J} A_n d_n \left(x - \hat{\alpha}_n, y - \hat{\beta}_n\right), \qquad (5.2)$$

where A is the vector of J weights that remain to be estimated according to the statistics of Eqn. 5.1, and n is used to index the sum to avoid confusion later in this derivation. Thus, $i(x, y)$ may be thought of as a pixel of the weighted motion-compensated frame average image. According to this model, frames that are found

to have low estimates for the corresponding weight A_j will tend to contribute less to the frame-averaged image.

5.3.1 Maximum Likelihood Frame Weight Estimator Derivation. Without the benefit of *a priori* information on the frame weights, a MAP estimator cannot be constructed, however, a suitable maximum likelihood (ML) estimator may be derived. Bayes rule may be used to maximize the probability of frame weights given the image data, $\Pr[A_j | d_j(x, y)]$, by simply maximizing the probability of the image data given the weights, $\Pr[d_j(x, y) | A_j]$ [71]. The pixels of the data are assumed independent and identically distributed as is often the case with similar developments [39], allowing

$$
P_{\mathbf{d}_j|\mathbf{A}}(\mathbf{D}_j|\mathbf{A}) = \prod_{x=1}^{N} \prod_{y=1}^{N} \frac{\Gamma\left(d_j\left(x - \hat{\alpha}_j, y - \hat{\beta}_j\right) + \mathcal{M}\right)}{\Gamma\left(d_j\left(x - \hat{\alpha}_j, y - \hat{\beta}_j\right) + 1\right)\Gamma(\mathcal{M})}
$$
$$
\left[1 + \frac{\mathcal{M}}{i(x, y)}\right]^{-d_j\left(x-\hat{\alpha}_j, y-\hat{\beta}_j\right)} \left[1 + \frac{i(x, y)}{\mathcal{M}}\right]^{-\mathcal{M}}. \tag{5.3}
$$

With the assumption that the frames are independent due to the relatively long interframe period and therefore contain uncorrelated speckle, the total probability may be found by multiplying the probabilities of all J image frames in the ensemble,

$$
P_{\mathbf{d}|\mathbf{A}}(\mathbf{D}|\mathbf{A}) = \prod_{j=1}^{J} \prod_{x=1}^{N} \prod_{y=1}^{N} \frac{\Gamma\left(d_j\left(x - \hat{\alpha}_j, y - \hat{\beta}_j\right) + \mathcal{M}\right)}{\Gamma\left(d_j\left(x - \hat{\alpha}_j, y - \hat{\beta}_j\right) + 1\right)\Gamma(\mathcal{M})}
$$
$$
\left[1 + \frac{\mathcal{M}}{i(x, y)}\right]^{-d_j\left(x-\hat{\alpha}_j, y-\hat{\beta}_j\right)} \left[1 + \frac{i(x, y)}{\mathcal{M}}\right]^{-\mathcal{M}}. \tag{5.4}
$$

It is convenient to maximize the natural logarithm of Eqn. 5.4 due to numerical difficulties encountered while multiplying many large numbers. The resulting log-likelihood function $L(\mathbf{d}) = \ln P_{\mathbf{d}|\mathbf{A}}(\mathbf{D}|\mathbf{A})$ is

$$L\left(\mathbf{d}\right) = \sum_{j=1}^{J}\sum_{x=1}^{N}\sum_{y=1}^{N}\left\{ \frac{\Gamma\left(d_j\left(x-\hat{\alpha}_j, y-\hat{\beta}_j\right)+\mathcal{M}\right)}{\Gamma\left(d_j\left(x-\hat{\alpha}_j, y-\hat{\beta}_j\right)+1\right)\Gamma\left(\mathcal{M}\right)} \right.$$

$$\left. - d_j\left(x-\hat{\alpha}_j, y-\hat{\beta}_j\right)\ln\left[1+\frac{\mathcal{M}}{i\left(x,y\right)}\right] - \mathcal{M}\ln\left[1+\frac{i\left(x,y\right)}{\mathcal{M}}\right] \right\}. \quad (5.5)$$

The intended maximization of the log-likelihood is with respect to the weights of the individual frames in the ensemble. Let A_{j_0} be an arbitrary frame weight in the set of A_j. Note that the first term within the braces of Eqn. 5.5 bears no dependence on the frame weights and may be disregarded in the maximization analysis. However, the remaining two terms have an implicit relationship with A_j as defined by Eqn. 5.2. After some arithmetic, the derivative of the log-likelihood with respect to an arbitrary weight in the ensemble can be expressed as

$$\frac{dL\left(\mathbf{d}\right)}{dA_{j_0}} = \sum_{j=1}^{J}\sum_{x=1}^{N}\sum_{y=1}^{N}\frac{d}{dA_{j_0}}\left\{ d_j\left(x-\hat{\alpha}_j, y-\hat{\beta}_j\right)\ln i\left(x,y\right) \right.$$

$$\left. - \left[d_j\left(x-\hat{\alpha}_j, y-\hat{\beta}_j\right)+\mathcal{M}\right]\ln\left[\mathcal{M}+i\left(x,y\right)\right] \right\}. \quad (5.6)$$

In order to simplify this expression, it is necessary to examine the change in $i(x,y)$ with respect to A_{j_0}. By substitution with Eqn. 5.2,

$$\frac{d}{dA_{j_0}}i\left(x,y\right) = \frac{d}{dA_{j_0}}\frac{1}{J}\sum_{n=1}^{J}A_n d_n\left(x-\hat{\alpha}_n, y-\hat{\beta}_n\right), \quad (5.7)$$

the change in $i(x,y)$ with respect to A_{j_0} reduces to the single term after expanding the sum,

$$i'(x,y) = \frac{d}{dA_{j_0}}i\left(x,y\right) = \frac{1}{J}d_{j_0}\left(x-\alpha_{j_0}, y-\beta_{j_0}\right). \quad (5.8)$$

After a bit more arithmetic, the derivative may be expressed as

$$\frac{dL\left(\mathbf{d}\right)}{dA_{j_0}} = \sum_{j=1}^{J}\sum_{x=1}^{N}\sum_{y=1}^{N} i'\left(x,y\right)\left\{\frac{d_j\left(x-\hat{\alpha}_j, y-\hat{\beta}_j\right)}{i\left(x,y\right)} - \frac{d_j\left(x-\hat{\alpha}_j, y-\hat{\beta}_j\right)+\mathcal{M}}{\mathcal{M}+i\left(x,y\right)}\right\}. \quad (5.9)$$

By rearranging the terms and setting to zero to find the maximum of the log-likelihood, one obtains

$$\sum_{j=1}^{J}\sum_{x=1}^{N}\sum_{y=1}^{N}\frac{d\left(x-\hat{\alpha}_j, y-\hat{\beta}_j\right)}{i\left(x,y\right)}d_{j_0}\left(x-\alpha_{j_0}, y-\beta_{j_0}\right) =$$

$$\sum_{k=1}^{J}\sum_{x=1}^{N}\sum_{y=1}^{N}\frac{d\left(x-\hat{\alpha}_k, y-\hat{\beta}_k\right)+\mathcal{M}}{\mathcal{M}+i\left(x,y\right)}d_{j_0}\left(x-\alpha_{j_0}, y-\beta_{j_0}\right). \quad (5.10)$$

Although an explicit solution for the elements of A does not appear to be readily obtainable, an iterative solution may be found as follows. For each particular frame weight in the ensemble, A_{j_0}, a new estimate, $\hat{A}_{j_0}^{new}$ may be recursively found from the previous estimate, $\hat{A}_{j_0}^{old}$, given a particular dataframe from the ensemble, d_{j_0}.

The update equation may be conveniently expressed as

$$\hat{A}_{j_0}^{new} = \hat{A}_{j_0}^{old}\frac{\sum\limits_{j=1}^{J}\sum\limits_{x=1}^{N}\sum\limits_{y=1}^{N}\frac{d\left(x-\hat{\alpha}_j, y-\hat{\beta}_j\right)+\mathcal{M}}{\mathcal{M}+i^{old}(x,y)}d_{j_0}\left(x-\hat{\alpha}_{j_0}, y-\hat{\beta}_{j_0}\right)}{\sum\limits_{k=1}^{J}\sum\limits_{x=1}^{N}\sum\limits_{y=1}^{N}\frac{d\left(x-\hat{\alpha}_k, y-\hat{\beta}_k\right)}{i^{old}(x,y)}d_{j_0}\left(x-\hat{\alpha}_{j_0}, y-\hat{\beta}_{j_0}\right)}, \quad (5.11)$$

where

$$i^{old}\left(x,y\right) = \frac{1}{J}\sum_{n=1}^{J}\hat{A}_n^{old}d_n\left(x-\hat{\alpha}_n, y-\hat{\beta}_n\right).$$

This recursive technique has the benefit of restricting $\hat{A}_{j_0}^{new}$ to be a member of the set of positive real numbers. To estimate the J frame weights of images in an ensemble, Eqn. 5.11 must be iterated for each frame under consideration. At each iteration, the average image $i(x,y)$ is reformed with the frame weights found from the previous iteration according to Eqn. 5.2.

Appendix A describes a direct solution of a likelihood function based on simpler Gaussian statistics rather than negative binomial statistics.

5.3.2   ML Frame Weight Estimator Implementation.   The iterative algorithm was implemented using a general-purpose computer. Note that the numerator and denominator of the update equation in Eqn. 5.11 result in strictly positive scalar quantities due to the summation over all frames and pixels in the resulting images. A nominal starting point for the frame weights is a vector of ones. In practice, the resulting frame weights may be normalized to sum to J after each iteration, such that likely frames within the ensemble remain close to unity, while frames that are deemed outliers tend to drop to values less than unity as the iterations progress.

For all simulated and experimentally collected datasets analyzed, the algorithm appeared to slowly arrive at a solution where outlier frames have very small associated weights, while frames that fit well to the ensemble mean have associated weights that remain close to unity. However, no clear strategy for terminating the iterative process was discovered. Prior to using the algorithm, an estimate for the speckle parameter of the system, $\mathcal{M}$, must be found. If enough frames of registered image data are available from a calibration dataset, $\mathcal{M}$ may be found directly from the variance of pixel intensity along columns of bright pixels according to the expression for the variance of the negative binomial distribution [31],

$$\sigma_K^2 = \bar{K}\left(1 + \frac{\bar{K}}{\mathcal{M}}\right). \tag{5.12}$$

Alternatively, the maximum likelihood estimation procedure for the speckle parameter described in Sec. 2.5 may be used.

Algorithm convergence was notably faster for larger values of the coherent source speckle parameter. Although the convergence of the iterative algorithm can be slow for low values of $\mathcal{M}$, an important observation was that the gradients of the weights

5-11

could be inspected after only a few iterations in order to decide if the associated frames indicated poor ensemble registration.

As an example, Fig. 5.3 shows the first difference of the weight vector after only two iterations using imagery collected from an experimental optical range. These are the same data used to create the images shown in Figures 5.1 and 5.2. Note that five of the frames are associated with weights that have highly negative gradients. These frames correspond to the registration errors that occur due to false correlation of a bright specular return source on the remote scene. As the algorithm is allowed to progress until the likelihood equation approaches an asymptotic value, the weights of the corresponding negative gradients eventually approach zero. However, the number of iterations required to reach such convergence might be prohibitive in many applications. In such applications, a simple method might be devised to compare the gradient of the weights to the ensemble mean or median of the gradients after several iterations, effectively detecting frames that do not fit well to the image ensemble. Figure 5.4 (a) shows a typical weight corresponding to an outlier frame as a function of the number of iterations, while Fig. 5.4 (b) shows the ensemble likelihood as calculated for each iteration step using Eqn. 5.5. Figure 5.5 (b) shows the resulting frame average image with weights derived from the iterative algorithm after 1200 iterations. Notably absent is the contribution from the poorly registered frames visible in Fig. 5.2 and repeated for comparison in Fig. 5.5 (a).

The outlier detection algorithm did not appear to be overly sensitive to poor estimates of the speckle parameter. While low estimates of the system speckle parameter did tend to slow the rate at which frame weights decreased below unity, higher estimates tended to speed weight decrease by a commensurate amount. However, in all cases studied, the relative gradient of the weights seemed to provide a reliable and robust indicator of frames that were either poorly registered or had significant image warping.
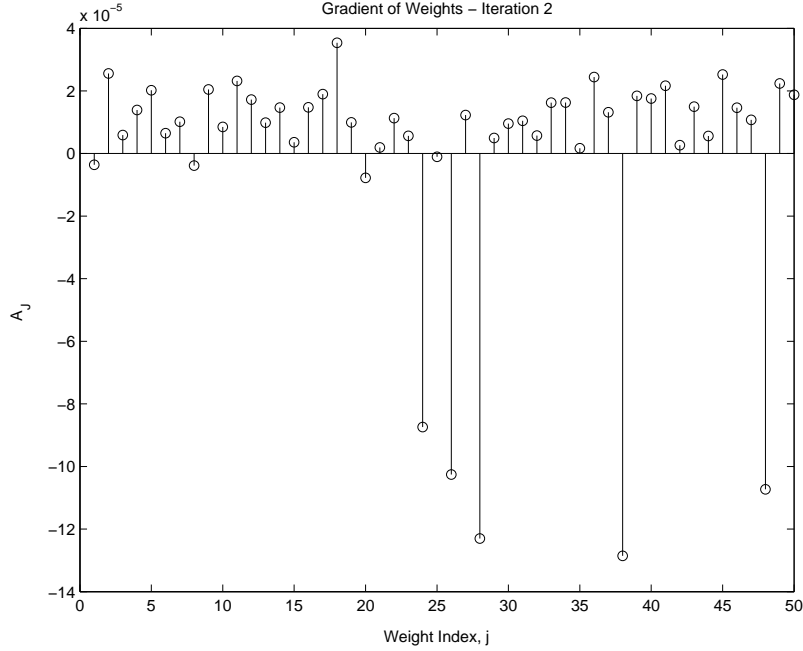
Figure 5.3: Plot of the gradient of the weights (first difference) calculated after two iterations of Eqn. 5.11 for each of the 50 weights. Frames 24, 26, 28, 38 and 48 are good candidates for elimination, due to a substantial negative trend of the weights towards zero. Image data was experimentally collected at a range of 10 km and had an estimated speckle parameter of $\mathcal{M} = 60$. The vector-correlation method of [7] was used to register the imagery.

5.4 *Frame Average Image Improvement by Discarding Suspect Outlier Image Frames*

The frame weight estimation technique described in Sec. 5.3 may be impractical for some applications due to several shortcomings. The most notable detractor of the algorithm is its computational burden. Although the component mathematical operations are simple, the number of operations increases dramatically for large, operationally representative imagery, and large numbers of images within each ensemble. Another detractor involves the means to stop such an iterative algorithm. Although one might find a suitable stopping criteria by inspection of the iterative weight differences or perhaps the rate of ascent of the log-likelihood curve, no measure of optimality is guaranteed by such *ad-hoc* criteria. To overcome such limitations, the problem was recast as a binary hypothesis as discussed below.
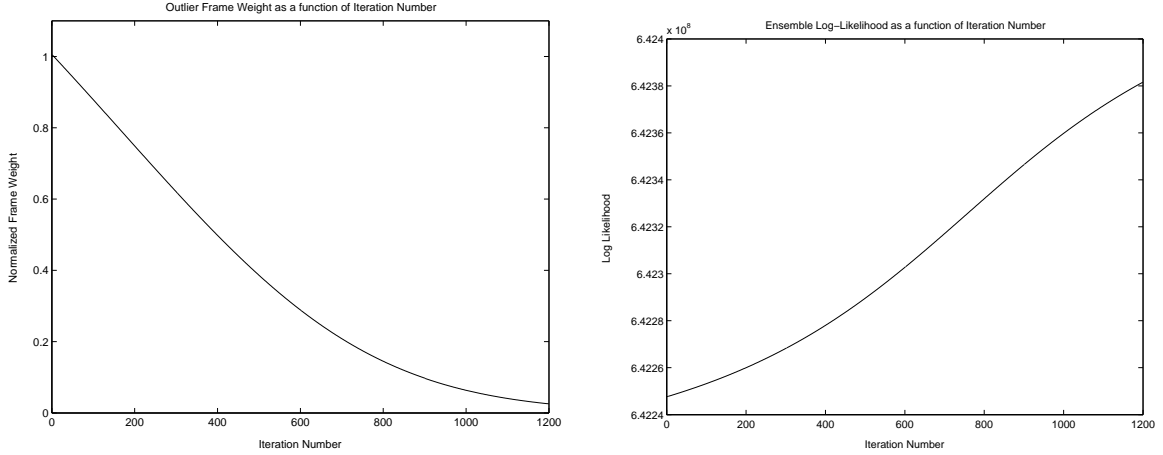
(a) Typical outlier continuous frame weight as a function of iteration.

(b) Overall ensemble likelihood as a function of iteration.

Figure 5.4:   Calculated weight of a typical outlier frame and ensemble likelihood as a function of the number of iterations. As iterations progress, the weight assigned to an outlier frame tends to decrease asymptotically to zero (a), while the overall ensemble likelihood tends to increase (b).

Significant insight may be obtained by examination of frame weight values after a large number of estimator iterations. For datasets which contain outliers due either to local or global mis-registration, the weights corresponding to outlier frames tended to decrease to very small values. This observation suggests the utility of an algorithm that permits only binary frame weighting. Such a system would assign a frame weight of unity for those frames that fit well to the ensemble average, while assigning a value of zero to those that did not.

The problem may be simplified by formulating two distinct hypotheses. Let H^0 represent the hypothesis that the frame is well matched to the ensemble average, while H^1 represents the case that the frame is an outlier relative to other images within the ensemble. Under this framework, two distinct frame average images may be constructed. Under H^0 the candidate frame A_{j_0} should be included in the ensemble and be assigned full weighting of $A_{j_0} = 1$. In this case the frame average may be constructed by including the frame in the set of equally weighted frames in the ensemble,
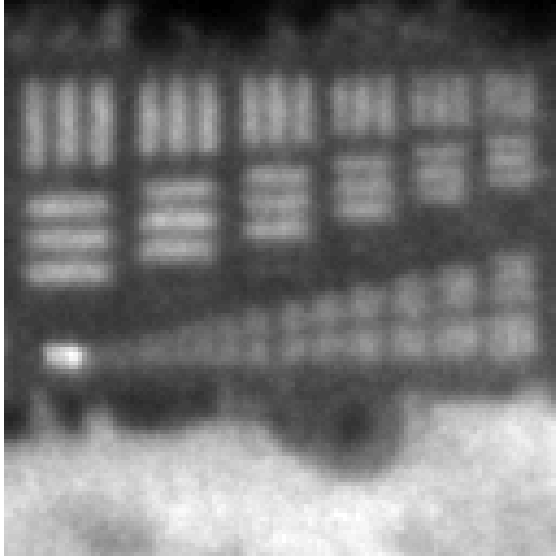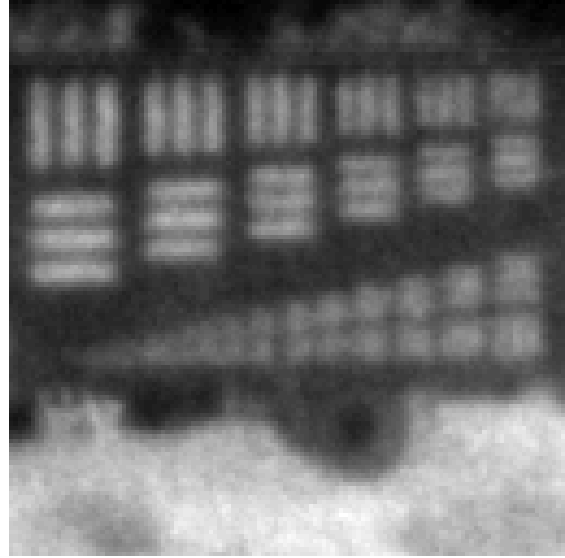
(a) Unweighted average image. (b) ML frame weighted average image.

Figure 5.5: Comparison of the weighted average image created by applying the iteratively determined weights to the frames within the ensemble, to the unweighted average image using all frames in the ensemble. Subimage (a) shows the unweighted average image. Due to the low value of some of the weights, the resulting weighted average image of subimage (b) is essentially created by eliminating those weights that have driven to values close to zero after 1200 iterations. Note the absence of the bright specular return and vertical ghosting of horizontal resolution bars evident in subimage (a).

$$i^0(x, y) = \frac{1}{J} \sum_{n=1}^{J} d_n \left(x - \hat{\alpha}_n, y - \hat{\beta}_n \right). \tag{5.13}$$

For the case of the alternate hypothesis, H^1, the frame average may be constructed by deleting the frame under consideration, while assigning equal weighting to the remaining frames in the ensemble,

$$i^1(x, y) = \frac{1}{J-1} \sum_{n \neq j_0}^{J} d_n \left(x - \hat{\alpha}_n, y - \hat{\beta}_n \right). \tag{5.14}$$

To compute a binary hypothesis test, the probability distributions governing each hypothesis must be computed and compared. The likelihood ratio test provides a convenient method to effect such a comparison [71]. Under this construct, if

$$\frac{Pr[H^1]}{Pr[H^0]} > \gamma, \tag{5.15}$$

where γ represents some threshold determined by cost, then the data was most likely generated under hypothesis H^1. The probability distributions $Pr[H^0]$ and $Pr[H^1]$ may be quantified by substitution of Equations 5.13 and 5.14 into Eqn. 5.1 with $\bar{K}$ equal to either $i^0(x, y)$ or $i^1(x, y)$. For the jth frame of the ensemble, the corresponding distributions are

$$P_{d_j}^0 (D_j) = \prod_{x=1}^{N} \prod_{y=1}^{N} \frac{\Gamma \left(d_j \left(x - \hat{\alpha}_j, y - \hat{\beta}_j \right) + \mathcal{M} \right)}{\Gamma \left(d_j \left(x - \hat{\alpha}_j, y - \hat{\beta}_j \right) + 1 \right) \Gamma (\mathcal{M})}$$
$$\left[1 + \frac{\mathcal{M}}{i^o(x, y)} \right]^{-d_j \left(x - \hat{\alpha}_j, y - \hat{\beta}_j \right)} \left[1 + \frac{i^0(x, y)}{\mathcal{M}} \right]^{-\mathcal{M}} \tag{5.16}$$

and

$$P^1_{d_j}(D_j) = \prod_{x=1}^{N} \prod_{y=1}^{N} \frac{\Gamma\left(d_j\left(x-\hat{\alpha}_j, y-\hat{\beta}_j\right) + \mathcal{M}\right)}{\Gamma\left(d_j\left(x-\hat{\alpha}_j, y-\hat{\beta}_j\right) + 1\right)\Gamma(\mathcal{M})}$$
$$\left[1 + \frac{\mathcal{M}}{i^1(x,y)}\right]^{-d_j\left(x-\hat{\alpha}_j, y-\hat{\beta}_j\right)} \left[1 + \frac{i^1(x,y)}{\mathcal{M}}\right]^{-\mathcal{M}} \qquad (5.17)$$

for the the H^0 and H^1 hypotheses respectively.

Upon assumption of statistically independent ensemble images, the total probability likelihood ratio for the j_0^{th} frame may be written as

$$\Delta_{j_0} = \frac{P_d^1(D)}{P_d^0(D)} > \gamma, \qquad (5.18)$$

where

$$\Delta_{j_0} = \frac{\displaystyle\prod_{k \neq j_0}^{J} \prod_{x=1}^{N} \prod_{y=1}^{N} \left\{ \frac{\Gamma\left(d_k(x-\hat{\alpha}_k, y-\hat{\beta}_k) + \mathcal{M}\right)}{\Gamma\left(d_k(x-\hat{\alpha}_k, y-\hat{\beta}_k) + 1\right)\Gamma(\mathcal{M})} \left[1 + \frac{\mathcal{M}}{i^1(x,y)}\right]^{-d_k\left(x-\hat{\alpha}_k, y-\hat{\beta}_k\right)} \left[1 + \frac{i^1(x,y)}{\mathcal{M}}\right]^{-\mathcal{M}} \right\}}{\displaystyle\prod_{j=1}^{J} \prod_{x=1}^{N} \prod_{y=1}^{N} \left\{ \frac{\Gamma\left(d_j(x-\hat{\alpha}_j, y-\hat{\beta}_j) + \mathcal{M}\right)}{\Gamma\left(d_j(x-\hat{\alpha}_j, y-\hat{\beta}_j) + 1\right)\Gamma(\mathcal{M})} \left[1 + \frac{\mathcal{M}}{i^0(x,y)}\right]^{-d_j\left(x-\hat{\alpha}_j, y-\hat{\beta}_j\right)} \left[1 + \frac{i^0(x,y)}{\mathcal{M}}\right]^{-\mathcal{M}} \right\}}. \qquad (5.19)$$

Although not identical, the leading gamma terms in both the numerator and denominator may be simplified by noting that all but the j_0^{th} term will survive the division operation of the likelihood ratio. The resulting expression may then be written as

$$\Delta_{j_0} = \frac{\displaystyle\prod_{k \neq j_0}^{J} \prod_{x=1}^{N} \prod_{y=1}^{N} \left\{ C_{j_0} \left[1 + \frac{\mathcal{M}}{i^1(x,y)}\right]^{-d_k\left(x-\hat{\alpha}_k, y-\hat{\beta}_k\right)} \left[1 + \frac{i^1(x,y)}{\mathcal{M}}\right]^{-\mathcal{M}} \right\}}{\displaystyle\prod_{j=1}^{J} \prod_{x=1}^{N} \prod_{y=1}^{N} \left\{ \left[1 + \frac{\mathcal{M}}{i^0(x,y)}\right]^{-d_j\left(x-\hat{\alpha}_j, y-\hat{\beta}_j\right)} \left[1 + \frac{i^0(x,y)}{\mathcal{M}}\right]^{-\mathcal{M}} \right\}}. \qquad (5.20)$$

where

$$C_{j_0} = \frac{\Gamma\left(d_{j_0}\left(x-\hat{\alpha}_{j_0}, y-\hat{\beta}_{j_0}\right) + 1\right)\Gamma(\mathcal{M})}{\Gamma\left(d_{j_0}\left(x-\hat{\alpha}_{j_0}, y-\hat{\beta}_{j_0}\right) + \mathcal{M}\right)} \qquad (5.21)$$

is the surviving gamma term after division. To avoid numerical difficulties, a log-likelihood ratio may be calculated as

$$\mathbb{D}_{j_0} = \frac{\sum\limits_{k \neq j_0}^{J} \sum\limits_{x=1}^{N} \sum\limits_{y=1}^{N} \left\{ \ln(C_{j_0}) - d_k \left(x - \hat{\alpha}_k, y - \hat{\beta}_k \right) \ln \left[\frac{\mathcal{M} + i^1(x,y)}{i^1(x,y)} \right] - \mathcal{M} \ln \left[\frac{\mathcal{M} + i^1(x,y)}{\mathcal{M}} \right] \right\}}{\sum\limits_{j=1}^{J} \sum\limits_{x=1}^{N} \sum\limits_{y=1}^{N} \left\{ -d_j \left(x - \hat{\alpha}_j, y - \hat{\beta}_j \right) \ln \left[\frac{\mathcal{M} + i^0(x,y)}{i^0(x,y)} \right] - \mathcal{M} \ln \left[\frac{\mathcal{M} + i^0(x,y)}{\mathcal{M}} \right] \right\}}. \qquad (5.22)$$

To decide if the suspect j_0^{th} frame should be retained for inclusion within the weighted frame average, one needs only compute the ratio $\mathbb{D}_{j_0}$ for each of the J frames in the ensemble. As will be clarified in the following section, inspection of the distribution of likelihood ratios reveals those frames that should be retained or discarded in order to increase the overall likelihood of the ensemble averaged image.

5.4.1 *Distribution of Likelihood Ratios for Ensemble Images.*

The random nature of the images collected by the coherent imaging system yields a likelihood ratio that may also be considered a random variable $\mathbb{D}$. In order to decide which frames should be discarded, a rule must be established to compare the elements of the likelihood ratio $\mathbb{D}$ to some threshold γ. A simple rule might set the threshold to the sample mean of the likelihood ratio population, and discard those frames that fall below this mean,

$$\mathbb{D}_{j_0} \underset{H_0}{\overset{H_1}{\gtrless}} \bar{\mathbb{D}} = \frac{1}{J} \sum_{j=1}^{J} \mathbb{D}_j. \qquad (5.23)$$

Using such a rule, if $\mathbb{D}_{j_0} > \bar{\mathbb{D}}$ then the hypothesis H^1 must be declared as indicated in Eqn. 5.15 for the j_0^{th} frame.

Unfortunately, such a simple rule presents difficulties in practical applications. An important shortcoming of this simple rule may be understood by considering the case where an ensemble contains many images that fit fairly well to the average ensemble image, several images that are moderately degraded by warping or mis-registration, and yet a few images that are severely degraded. Using the rule of

Eqn. 5.23, the calculated threshold would be heavily influenced by the few severely corrupted image frames. In practice, this threshold might be so large that the moderately corrupted image frames would not be identified as outliers relative to the majority of the ensemble family.

The development of a more useful decision rule requires an understanding of the distribution of the random variable $\mathbb{D}$. Unfortunately, complete characterization of this distribution requires *a priori* information concerning the remote target scene as well as the current atmospheric conditions under which the imagery was collected. However, the problem may be simplified by considering two distinct cases. One case considers the vector of likelihood ratios $\mathbb{D}^0$ corresponding to frames from an ensemble of images corrupted only by the negative binomial noise process. The second case involves likelihood ratios $\mathbb{D}^1$ corresponding to frames from an ensemble where some image frames are corrupted by other noise processes such as global mis-registration or anisoplanatic frame warping.

Considering the case of $\mathbb{D}^0$, an argument may be made to demonstrate that the distribution approaches Gaussian in the limit as the number of frames in the ensemble grows large. The denominator of Eqn. 5.22 may be considered to be a constant K for a given ensemble of images, and does not change as a function of the selected frame j_0 under consideration. In this case, the random variable may be expressed as

$$\mathbb{D}_{j_0}^0 = \frac{1}{K} \sum_{k \neq j_0}^{J} \sum_{x=1}^{N} \sum_{y=1}^{N} \left\{ \ln(C_{j_0}) - d_k \left(x - \hat{\alpha}_k, y - \hat{\beta}_k \right) \ln \left[\frac{\mathcal{M} + i^1(x,y)}{i^1(x,y)} \right] - \mathcal{M} \ln \left[\frac{\mathcal{M} + i^1(x,y)}{\mathcal{M}} \right] \right\}. \qquad (5.24)$$

In the limit as the number of statistically independent frames grows large, the summation of J unknown distributions approaches Gaussian per the Central Limit Theorem. Division of this random variable by the constant K only scales this Gaussian distribution. This result is intuitively satisfying, as it implies that a subject frame under the case of $\mathbb{D}^0$ will result in a likelihood ratio that symmetrically falls on either side of the mean of some unimodal distribution. This distribution is depicted in Fig. 5.6 as

$p_d(D^0)$. In some cases the frame may fit better to the ensemble average, in other cases worse. Such behavior may be attributed to the unbiased fit that a particular frame will have within an ensemble where the only distortion is caused by the statistics attributed to partially coherent illumination.

In the case of $\mathbb{D}^1$, frames that do not fit well to the ensemble will cause the numerator of Eqn. 5.22 to become large, since the likelihood $P_d^1(D)$ will increase for such frames. However, those frames that do fit the average ensemble image will distribute as for the case of $\mathbb{D}^0$. This mechanism destroys the symmetry of the distribution. Frames that do not fit the ensemble will tend to skew the distribution by pushing the mean of the distribution towards larger values. This distribution is depicted in Fig. 5.6 as $p_d(D^1)$. This result is useful to help determine how best to select those frames that must be discarded from the ensemble.
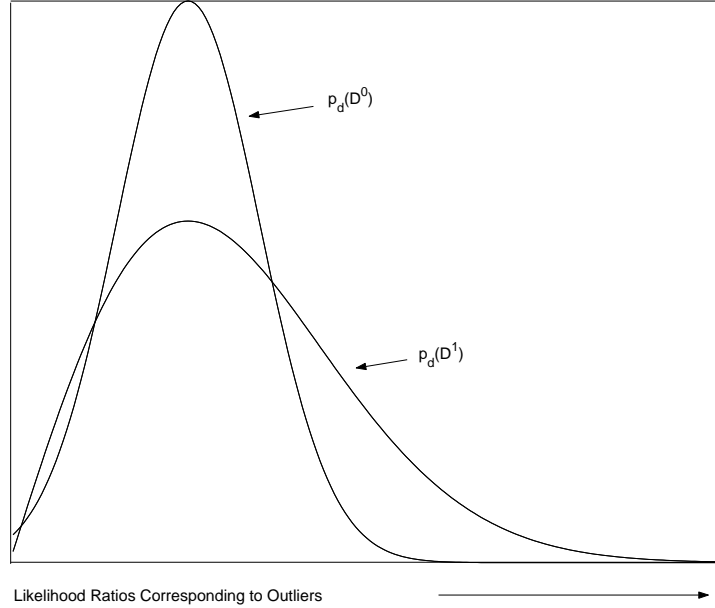
Figure 5.6:   Plot of two distinct distributions of the random variable $\mathbb{D}$. The symmetrical normal distribution $p_d(D^0)$ results from the likelihood ratio test for the case where all frames are corrupted only by negative binomial noise. The skewed distribution corresponding to outlier frames is labeled as $p_d(D^1)$. For the case where a significant number of frames are corrupted by other noise processes such as image warping or global mis-registration, the symmetry of the PDF $p_d(D^0)$ is destroyed because the value of the likelihood ratio of Eqn. 5.22 tends to increase for such frames.

In contrast to the rule proposed in Eqn. 5.23, a more appropriate algorithm evaluates and compares the distribution of an unknown likelihood ratio vector $\mathbb{D}$ to a Gaussian distribution. If the distribution appears Gaussian within some predefined confidence metric, the algorithm may be terminated and only image data with likelihood ratios greater than a preset threshold would be discarded. Alternatively, in the case where the distribution of $\mathbb{D}$ is found to be sufficiently distinct (skewed) from a Gaussian distribution, frames with likelihood ratios above the threshold should be discarded and the likelihood ratio test repeated. A suitable threshold may be found by first calculating the unbiased sample variance

$$\sigma_{\mathbb{D}}^2 = \frac{1}{N-1} \sum_{j=1}^{J} \left(\mathbb{D}_j - \bar{\mathbb{D}} \right), \tag{5.25}$$

where $\bar{\mathbb{D}}$ is defined by Eqn. 5.23. The standard deviation of the distribution is $\sigma_{\mathbb{D}}$ and may be used to formulate a suitable threshold. Setting a 1-sigma threshold of $\gamma = \bar{\mathbb{D}} + \sigma_{\mathbb{D}}$ identifies those frames that are reasonably distant from the process mean for elimination from the ensemble average. After elimination, another ratio test must be performed to ensure that elimination of these outliers yields a Gaussian distribution of likelihood ratios. If not, the algorithm must be repeated until outliers have been eliminated. Such processing avoids the possibility of undetected moderate outliers due to the presence of frames that are far removed from the ensemble average.

5.4.2   Testing the Likelihood Ratio for Gaussian Distribution.   Several statistical tools exist to test an unknown distribution for Gaussian fit. Of particular merit is the Lilliefors statistical test [16], which does not require *a priori* knowledge of the parameters of the Gaussian distribution to which the data are compared.

The Lilliefors test requires calculation of the sample mean and variance as described in Eqn. 5.23 and 5.25. The observed data ratios $\mathbb{D}_j$ are statistically normalized

by subtracting the mean and dividing by the variance,

$$\mathbb{Z}_j = \frac{\mathbb{D}_j - \bar{\mathbb{D}}}{\sigma_{\mathbb{D}}} \quad j = 1, 2, ..., J. \tag{5.26}$$

This data normalization process distinguishes the test as a refinement of the Kolmogorov-Smirnov test for normality [16]. Two hypotheses are proposed. $\mathcal{H}_0$ is the hypothesis that the random sample comes from a normal distribution with unspecified mean and variance, while $\mathcal{H}_1$ denotes the hypothesis that the data comes from a non-normal distribution. The empirical cumulative distribution $S(j)$ function is constructed from the normalized data samples and compared to the standard normal cumulative distribution function $F(j)$. The Lilliefors test statistic T is defined as the largest difference between the two cumulative distributions,

$$T = \sup_j |F(j) - S(j)| . \tag{5.27}$$

Using this construct, reject $\mathcal{H}_0$ (delcare the sample data as non-normally distributed) with significance level α if the test statistic is greater than $p = 1 - \alpha$. Tables of Lilliefors quantiles for varying sample sizes and α may be found in the literature, e.g. [16]. For sample sizes of $J > 30$ samples, a p-value of 95% can be found by calculating $w_{.95} = 0.866/\sqrt{J}$. If T is found to exceed $w_{.95}$, the hypothesis that the data were drawn from a normal distribution may be rejected within a confidence interval of 95%.

5.5 Results using Simulated Anisoplanatic Imagery Data

Simulation of a coherent laser vision system was discussed in detail in Sections 2.1 through 2.3. The anisoplanatic viewing conditions encountered by a wide FOV optical system may cause significant anisoplanatic image warping due to the shift-variance of the optical system. In addition, the speckle caused by coherent illumination and atmospheric phase delay makes accurate global image registration

difficult, especially where long optical paths reduce the available signal-to-noise ratio at the imaging detector. The effects may be accurately simulated using the same techniques used to conduct the remote scene and seeing condition estimation experiments documented in Chapters III and IV.

A resolution board target intensity pattern was propagated to the optical aperture through various levels of turbulence simulated by the placement of Gaussian random thin phase screens along the optical path. The synthetically generated imagery was generated with a speckle parameter of $\mathcal{M} = 60$ to match the experimentally collected image data discussed in Sec. 5.6. Observation of the individually generated images under poor seeing conditions revealed significant anisoplanatic image warping that was impossible to remove by global image registration techniques, as may be illustrated by the example of Fig. 5.7. The vector correlation image registration algorithm described in [7] was selected to remove global image tilt. Despite global tilt removal, significant image blurring was noted in the unweighted frame average due to many highly distorted speckle images caused by the random nature of the generated phase screens. Figure 5.7 shows a comparison between a nominal simulated speckle image that does not suffer dramatic distortion effects, and an image selected due to its heavily distorted appearance caused by a particularly unlucky phase screen that was generated close to the optical aperture. Clearly, the removal of rogue images such as that shown in Fig. 5.7 (b) from the ensemble average will tend to enhance the effective seeing condition of the system.

To understand the performance of the detection algorithm under a broad range of atmospheric conditions, the simulated imagery data of Chapter IV were processed for outlier detection. The data were partitioned into subsets of 50-frame image ensembles for a total of 10 ensembles per atmospheric condition. D/r_0 conditions of 10, 4, 5, 2.5, 2, 1.3 and 1 were simulated using a 20 cm optical aperture. Simulation parameters of these data are summarized in Table 5.1. The data were processed for outliers using the algorithm detailed in Sec. 5.4. A threshold of one standard deviation above the process mean was selected for rejection of suspected outliers, and the

(a) Nominal synthetic image frame.

(b) Synthetic image heavily distorted by turbulence.
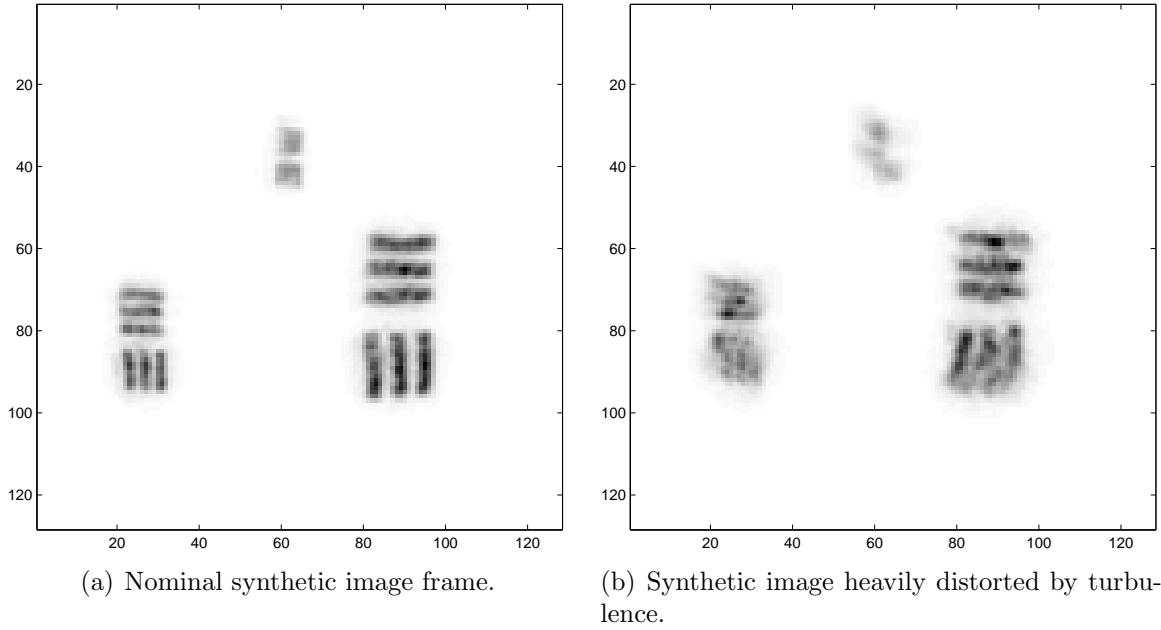
Figure 5.7:   Comparison of a pair of synthetically generated resolution bar target speckle images drawn from a randomly generated turbulence simulation. Simulated average r_0 is 2 cm. over a 10 kilometer path. Subfigure (a) shows a nominal frame from the ensemble. Distinct bars are apparent for all but the smallest pattern, however some anisoplanatic warping is notable. Subfigure (b) shows an image frame heavily distorted by the atmospheric distortion. Such a frame is clearly a good candidate for automatic removal by an outlier detection algorithm.

process was repeated until the likelihood ratio appeared to be normally distributed as discussed in Sec. 5.4.1. In most cases only two iterations of the likelihood ratio test were required to reach a normally distributed ratio distribution. For good seeing conditions, the likelihood ratio data appeared Gaussian after the first iteration, and no additional iterations were performed. In several cases under poor seeing conditions, a third iteration was required due to very distant outliers that tended to mask outliers closer to the process mean.

Table 5.1:   Table describing the simulation parameters used to create statistically accurate random speckle imagery for evaluation of the registration outlier detection algorithm.

Parameter	Value
Slant Range to Target	10 Kilometers
Optical Diameter	20 Centimeters
Speckle Parameter of Source	60
Pixels per Image	128 by 128
Pixel Pitch of Detector	11.8 micrometers
Mean Wavelength	1.54 micrometers
Focal Length	3 Meters
Images per Frame Ensemble	50
Size of Imaged Target Area	5 by 5 Meters

Figure 5.8 depicts a typical improvement in the average image gained by binary frame weighting of the component speckle image frames. Intensity bars are included in the figures to demonstrate the additional contrast that is gained by automated deletion of frames that serve only to blur the average image. Table 5.2 details the performance of the detection routine using simulated imagery for various atmospheric conditions. The knife-edge OTF estimation technique described in Sec. 2.9 was performed on the weighted average images to ascertain the level of improvement in spatial resolution gained by the automatic deletion of suspect frames.

(a) Synthetic unweighted average image.   (b) Synthetic binary weighted average image.
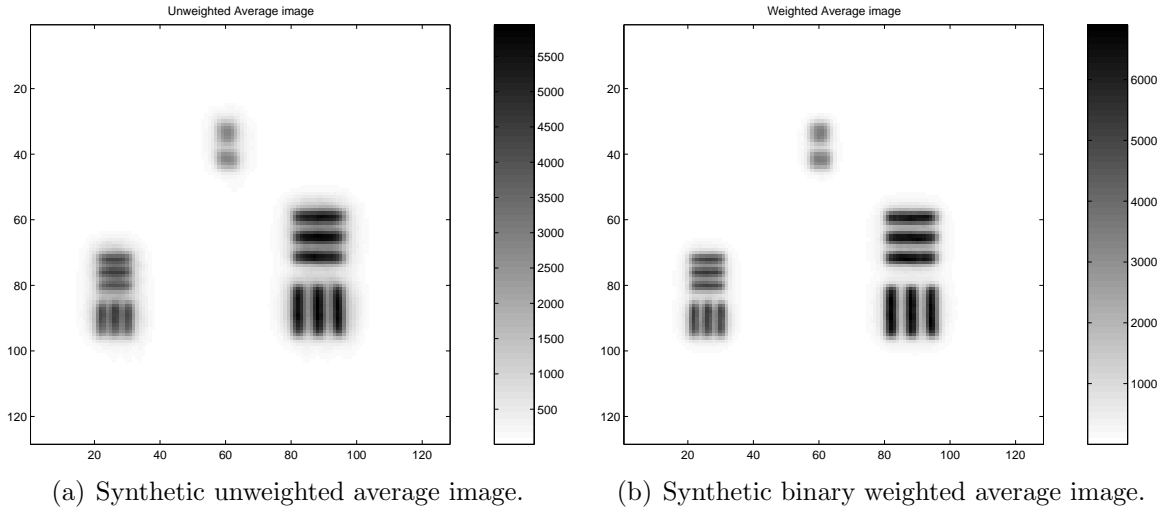
Figure 5.8:   Comparison of the unweighted (subimage a) and binary weighted (subimage b) average images for a typical outlier detection simulation. Sample image frames of this 50-frame ensemble are shown in Figures 5.7(a) and 5.7(b). Note the increased image contrast indicated by the maximum photon count on the intensity bars, as well as the slight but notable reduction of blur in the weighted average compared to the unweighted average. Simulated r_0 is 4 cm, and 21 of 50 frames were automatically removed from the ensemble prior to computing the average image shown in subimage (b).

Table 5.2:   Table showing the results of weighted frame averaging 5 sets of synthetically generated resolution bar imagery over a broad range of atmospheric seeing conditions. Values for number of frames rejected and effective r_0 are averaged over the ten 50 frame ensembles within each 500 image data set.

Target Set	Frames Rejected	Actual r_0	Effective r_0	r_0 Increase
Set 1	24.4	2 cm.	2.7 cm.	35%
Set 2	23.4	4 cm.	4.7 cm.	17%
Set 3	21.4	5 cm.	5.7 cm.	14%
Set 4	18.3	8 cm.	8.4 cm.	5%
Set 5	17.3	10 cm.	10.2 cm.	2%
Set 6	16.4	15 cm.	15.1 cm.	0.7%
Set 7	16.1	20 cm.	20.0 cm.	0%

5.6   *Results using Experimentally Collected Imagery Data*

A large variety of experimentally collected image data was available to test the outlier detection algorithm. In addition to the supported resolution bar target analyzed in Chapters III and IV, other interesting scenes were processed to test the outlier detection algorithm performance using nominal tactical imagery. In all cases, these image datasets were pre-processed for global tip and tilt removal by the fast vector correlation algorithm described in [7]. Figure 5.1 shows a nominal speckle image of the supported resolution bar target observed at a range of 10 kilometers using a 3 meter focal length optical system. Due to the presence of large resolution bars, the knife-edge OTF estimation technique describe in Sec. 2.9 was useful in determining the amount of improvement that removal of suspect speckle image frames produced for these datasets. Knife-edge estimation was not available for tactical target scenes. In these cases, the anisoplanatic OTF blind estimation algorithms described in Chapters III and IV was used to judge improvement. Several images are shown in the following figures to demonstrate the visual improvement realized by application of the outlier detection algorithm.

5.6.1   Resolution Bar Target Data.   Typical weighted versus unweighted resolution bar imagery is characterized by the improvement noted in Fig. 5.5. Five, 300-image sets of resolution bar imagery were processed by the outlier detection algorithm. The 300 image sets were partitioned into 50 frame ensembles prior to introduction to the outlier detection algorithm. Due to the 10 Hz frame collection rate, the generation of each ensemble required 5 seconds, over which the atmospheric conditions were assumed statistically stationary. The actual seeing condition was estimated from the unweighted average image. An *effective* r_0 was derived from the binary weighted average images, and may be considered a metric for image improvement between the unweighted and weighted average images. Table 5.3 documents the number of suspect frames deleted from the weighted average image, as well as the improvement noted in spatial resolution using knife-edge OTF estimation techniques.

Table 5.3:   This table describes the results of weighted frame averaging 5 distinct sets of resolution bar imagery collected on an experimental optics range. Values for number of frames rejected, actual and effective r_0 are averaged over the six 50 frame ensembles within each 300 image data set.

Target Set	Frames Rejected	Knife-Edge r_0	Effective r_0	r_0 Increase
Set 1	19.6	3.9	4.3	10%
Set 2	19.2	4.1	4.6	12%
Set 3	17.9	4.6	4.9	7%
Set 4	24.5	3.2	3.6	13%
Set 5	22.8	3.6	4.1	14%

5.6.2   Tactical Image Datasets.   To evaluate the utility of the algorithm on collections of image frames of nominal tactical scenes, several sets of imagery were processed. Three representative datasets are presented in the following sections. Spatial resolution improvement was indicated by the resulting images, and is quantified by estimation of an effective seeing condition for each the weighted and unweighted average imagery. Table 5.4 summarizes the improvement realized by application of the outlier detection algorithm to these diverse datasets.

(a) Unweighted M-60 average image.   (b) Binary weighted M-60 average image.
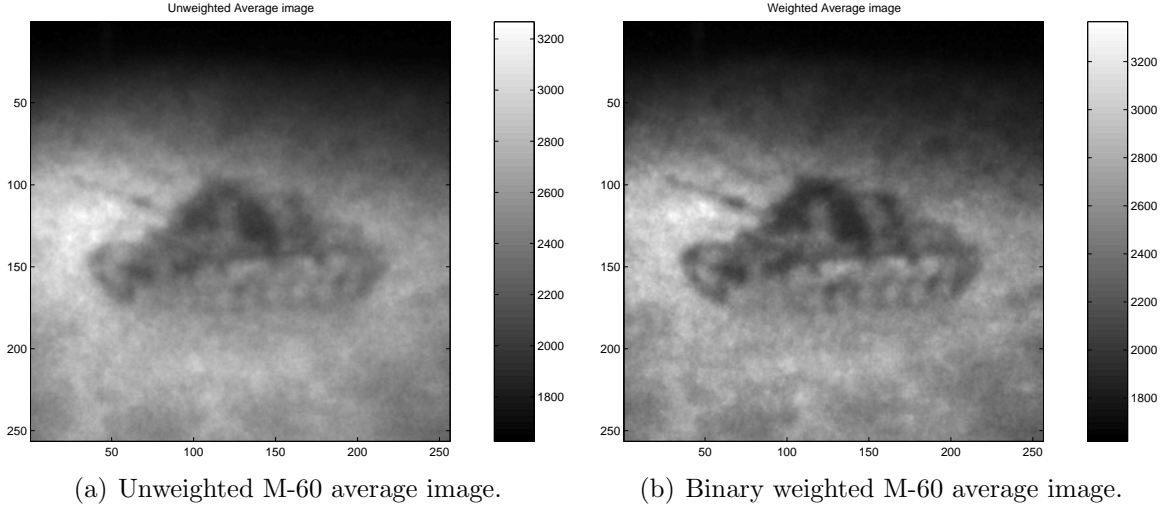
Figure 5.9:   Comparison of the unweighted (a) and binary weighted average image (b) for a M-60 armored tank. Contrast is slightly improved, with marked improvement in spatial resolution. Blind estimation of r_0 increased from 2.7 cm for the unweighted image, to 3.3 cm after image weighting. 24 of 50 frames were deleted from the ensemble prior to computing the average image shown in subimage (b).

5.6.2.1   M-60 Armored Tank Vehicle.   Fig 5.9 illustrates the comparison of weighted and unweighted average imagery obtained from remote imaging of an M-60 armored tank at 10 kilometers. Spatial resolution is markedly increased by deletion of outlier frames, although image contrast is not appreciably increased. 24 of 50 frames were selected for elimination by the algorithm, yielding a significant increase in effective r_0 for the imaging conditions from 2.7 cm to 3.3 cm. Figure 5.10 shows the increase in effective seeing conditions as estimated by the anisoplanatic blind deconvolution algorithm described in Chapters III and IV. The peak of the likelihood vs. r_0 curve is significantly shifted to the right by removal of suspected outlier frames.

5.6.2.2   M-923 5-Ton Truck with Structures.   Fig 5.11 shows a representative scene composed of a military 5-ton truck against a background of a building and a water tower. Significant vertical registration blur is evident by inspection of the vehicle headlights. The algorithm automatically discarded 21 of the 50 frames in the ensemble, producing an average image that has reduced blur and dramatically en-

(a) Unweighted M-60 r_0 plot.   (b) Binary weighted M-60 r_0 plot.
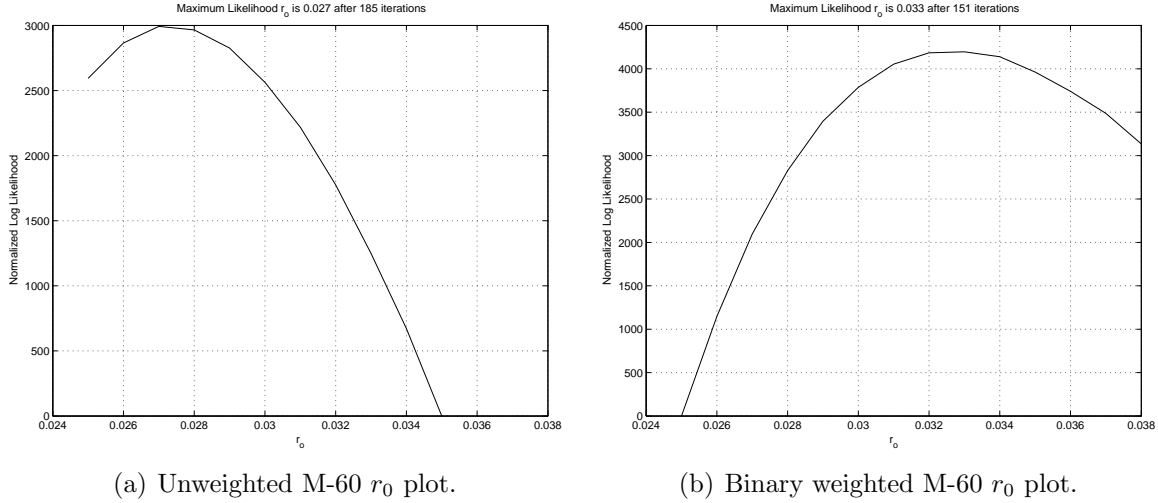
Figure 5.10:   Comparison of the estimated effective seeing conditions between the unweighted (a) and binary weighted (b) average images. The peak in the maximum likelihood estimator occurs at $r_0 = 2.7$ cm for the unweighted average, and increases to $r_0 = 3.3$ for the case of the binary weighted average image.

hanced contrast. Blind deconvolution estimation of the seeing condition has increased from approximately 4.2 to 4.8 cm, indicating notable improvement the spatial resolution of the final image.

   5.6.2.3   Scud Missile Imagery.   Fig 5.12 shows a Scud missile transport-erector-launch (TEL) vehicle against a fairly nondescript background. Application of the outlier removal technique improved the image contrast, and slightly but notably reduced the image blur. The effective r_0 was increased by more than 11% from 3.5 cm to 3.9 cm. Slightly better wheel definition and edge sharpness is apparent. Inspection of the individual frames of this dataset revealed that several frames were poorly registered by the fast vector correlation algorithm, and that some of the frames suffered from slight anisoplanatic warping effects.

5.7   Conclusions and Discussion

   Accurate identification of outlier image frames aids the image processor by reducing image blur due to averaging frames of a collected image ensemble. The max-

(a) Unweighted M-923 average image.   (b) Binary weighted M-923 average image.
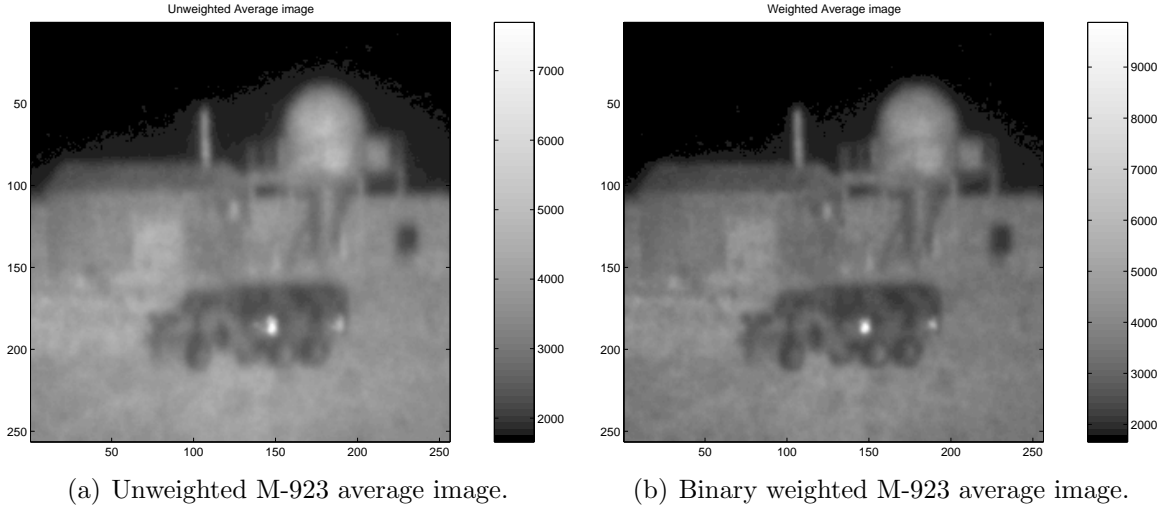
Figure 5.11:   Comparison of the unweighted (a) and binary weighted average image (b) for a M-923 5-ton truck and surrounding structures. Note the increased image contrast indicated by the maximum photon count on the intensity bars, as well as reduced blur noted by inspection of the specular returns from the vehicle headlights. Blind estimation of r_0 increased from 4.2 cm for the unweighted image, to 4.8 cm after image weighting. 21 of 50 frames were deleted from the ensemble prior to computing the average image shown in subimage (b).

(a) Unweighted Scud average image.   (b) Binary weighted Scud average image.
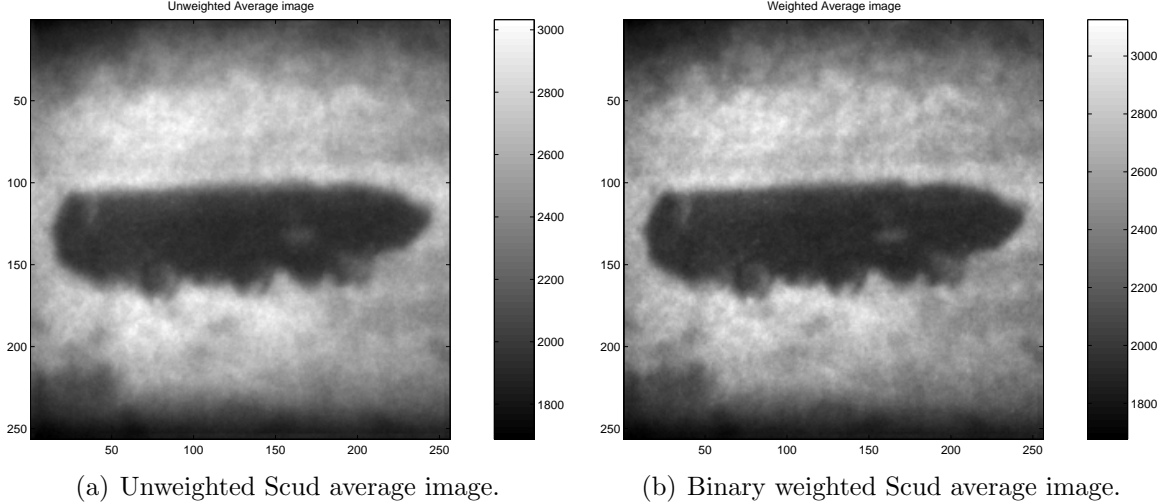
Figure 5.12:   Comparison of the unweighted (a) and binary weighted average image (b) for a Scud transporter-erector-launch (TEL) vehicle against a non-descript background. Note the slightly increased image contrast, as well as reduced blur noted by inspection of the horizontal edges of the TEL and wheels. Blind estimation of r_0 increased from 3.5 cm for the unweighted image, to 3.9 cm after image weighting. 22 of 50 frames were deleted from the ensemble prior to computing the average image shown in subimage (b).

Table 5.4:   Table describing the results of weighted frame averaging 3 diverse sets of tactical target imagery collected on an experimental optics range. Values for number of frames rejected, actual and effective r_0 are calculated for each of the three 50 frame ensembles.

Target Set	Frames Rejected	Actual r_0	Effective r_0	r_0 Increase
M-60 Tank	24	2.7	3.3	20%
M-923 Truck	21	4.2	4.8	14%
SCUD TEL	22	3.5	3.9	11%

imum likelihood framework derived in Sec. 5.3 appears to be a highly effective tool for identification of such frames.

For the case of simulated imagery, the technique appears to be highly effective for cases of relatively poor seeing condition, and less effective as the seeing parameter approaches the optical aperture diameter. This result is satisfying, as the formation of anisoplanatically warped images is less likely for better seeing conditions, and global tip and tilt are dramatically reduced. In cases of poor seeing conditions, the relative frequency of capturing a frame such as the warped image noted in Fig. 5.7(b) becomes more probable. For imagery collected during seeing conditions characterized by r_0 sizes approaching the optical aperture, the technique appears unnecessary. There remains the possibility of mis-registration of the imagery due to false correlation peaks specific to some datasets. This effected was noted during the processing of experimentally collected data, but was not encountered during reduction of the simulated data, perhaps due to the simplicity of the resolution pattern used in the study.

The results obtained from processing experimentally collected data were very promising. The concept of *effective r_0* was introduced in Sec. 5.6.1 to demonstrate the quantitative improvement of the average images formed by binary frame weighting of the component ensemble imagery. The increase in effective seeing conditions was notable in all imagery processed. The effect was dramatic for the cases where false correlation peaks prevented accurate registration of images. As an example, the

imagery used to form the average image shown in Fig. 5.5 was populated by several frames that did not register accurately due to a bright specular return from the chrome door handle of the vehicle that supported the resolution target board. This return was erroneously correlated with a portion of the resolution target board in some image frames. The detection of these frames is clear and distinct as demonstrated by the plot of likelihood ratios shown in Fig. 5.13.
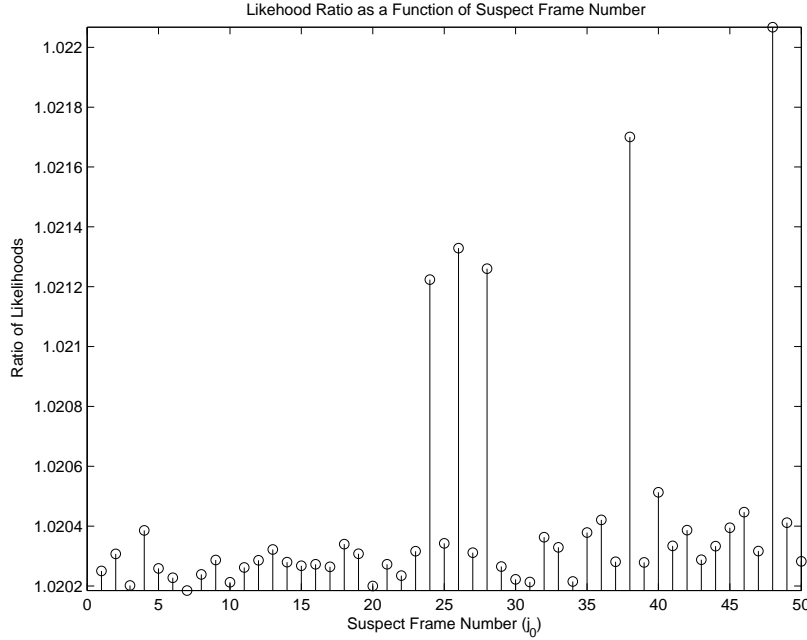
Figure 5.13:   Likelihood ratios calculated for a set of experimentally collected imagery of a supported resolution target board. The 5 notable outlier frames correspond to images that were not accurately registered to the ensemble mean due to false correlation peaks from a bright specular return.

The imagery of the M-60 tank discussed in Sec. 5.6.2.1 is an example of data corrupted by both anisoplanatic warping and the general inability of the registration algorithm to accurately align the image frames given the severe speckle noise of the data. Distinct features begin to become apparent in the resulting image after outlier removal, including the enhancement of the gun barrel and definition of the tread wheels. Such details become important to the tactical operator when faced with the tasks of vehicle identification or distinction between friend and foe. The plots shown in Fig. 5.10 depict a typical output from the blind deconvolution algorithm described

in detail in Chapters III and IV. The increase in the effective seeing condition of more than 20% is significant. The images of Figures 5.11 and 5.12 show similar contrast and sharpness enhancement, and demonstrate effective seeing condition increases of 14% and 11% respectively.

5.8   Summary

A novel Bayesian technique was developed to identify those frames within an ensemble of coherently collected imagery that tended to reduce the likelihood of the composite ensemble. It appears that the choice of the maximum likelihood cost function is useful under a framework where frames corresponding to low likelihoods reduce the contrast and spatial frequency content of the ensemble averaged image.

An initial research effort attempted to iteratively solve for the individual continuous weights of each image that maximized the overall likelihood of the entire ensemble. Under the assumption of individual pixel distributions, as well as statistical independence of the collected images, a composite likelihood of the image ensemble was derived using the negative binomial statistical model for detected intensity of a coherent imaging system. It was found that the iterative algorithm suffered from numerical expense. Additionally, it was difficult to determine a suitable termination criteria. Due to these limitations, a simpler model was developed to investigate the applicability of a binary frame weighting model, whereby frames assigned a weight of unity were retained, while those assigned a weight of zero were discarded. A likelihood ratio test provided a convenient and expeditious mechanism to assign these binary weights.

Application of the binary weights to form a weighted frame average resulted in ensemble average images that had improved contrast and spatial resolution, as further indicated by improvement of the apparent seeing conditions through which the individual images were formed. The applications of this system are numerous, and are not limited to coherent imaging systems as a slight modification of the negative binomial distribution to the Poisson distribution yields an estimator for incoherent

image outlier detection. Any imaging system faced with the problems of anisoplanatism and tip-tilt removal would benefit from the selective removal of images that do not positively contribute to the frame average. Such applications include tactical airborne or ground-based wide FOV imaging, as well as astronomical ground-based imaging systems that process large ensembles of short-exposure imagery.

VI. Conclusions and Summary

Restoration of images collected from the backscattered emissions of a remote target illuminated by partially coherent illumination is a challenging problem that offers system designers significant benefits over traditional imaging systems. Although passive infrared (IR) imaging systems operating in the thermal region offer the user moderate resolution without the need for active illumination of the scene, reliance on ambient illumination often presents operational difficulties. For passive IR imagers, the ambient thermal contrast ratio presents difficult challenges for application to target detection and recognition during the periods of thermal crossover that occur during dusk and dawn. In addition, such systems rely on emissions in the 8-12 micron wavelength region. Such wavelengths are an order of magnitude longer than typical high-power laser illuminators based on Nd:Yag technology which operate in the 1 to 1.5 micron region. Since the resolving power of an optical imaging system follows an inverse linear relation with wavelength, roughly an order of magnitude of resolution is gained by reconstructing imagery at the shorter wavelengths typical of high-power solid-state laser illuminators. In addition to the enhancement of basic resolution limits, the use of active illumination introduces tactical and strategic flexibility impossible with passive incoherent illumination. Gated laser vision systems allow reduction of noise by way of accurate shutter control in unison with beam pulse timing. Such a system allows tremendous flexibility in the elimination of visible clutter. For example, targets obscured by camouflage netting may be better resolved by first gating out the camouflage noise and operating on only the data within the tightly gated region surrounding the target depth. In addition, such mechanization provides accurate range information to different regions of the target field, although the challenges associated with this application were not investigated in this research effort.

6.1 Summary of MAP Estimation of Partially Coherent, Anisoplanatically Distorted Imagery

The accurate restoration of images created by an active coherent vision system comes at the expense of some particular difficulties. Even without the deleterious effects of atmospheric turbulence, the coherent nature of the active illumination causes highly speckled imagery that is often unsuitable for presentation to the operator without some form of image post-processing. The research described in the preceding chapters presupposes that individual images are first averaged to reduce the gross effects of laser as well as atmospheric speckle. Whether the image processor uses a single, or an ensemble average of partially coherent imagery, the accurate formulation of a likelihood-based image estimator depends firmly on the underlying assumption of the probabilistic distribution of the detected illumination. The negative binomial probability mass function has been demonstrated to be a very accurate model that conveniently extends from fully developed speckle imagery, to images formed from relatively incoherent lasers or even incoherent illumination in the more extreme case. In this regard, the research described here is easily extended along the continuum of coherency ranging from laser illuminators with extremely long coherence times to passively illuminated scenes. The latter case is merely a convenience due to the extension of the negative binomial distribution to the Poisson distribution for the limiting situation of very large speckle parameters.

Atmospheric turbulence causes tremendous image distortion for scenarios where long slant-range paths over low-altitude turbulence is unavoidable. Turbulence close to the optical aperture causes the majority of phase abberation in the detected imagery. Unlike satellite space-vehicle imaging systems, airborne or ground-based imaging systems will suffer high levels of atmospheric distortion. Adaptive optic wavefront pre-distortion allows highly effective image restoration for cases where the atmospheric distortion may be estimated in near real-time. However, such systems are large, expensive and computationally and mechanically complex. Application of AO technology to space and power-constrained platforms is a rich area of research that

will bear fruit in the coming decades. In the meantime, there is a growing need for post-processing algorithms that can effectively mitigate the effects of turbulence on images formed over long distances through large volumes of the atmosphere. To further complicate the problem, the FOV of candidate tactical systems is relatively wide, especially compared to those of the astronomical research community, where much of the research in image restoration algorithms has been conducted over the past several decades. Effective image restoration algorithms must deal with the high levels of anisoplanatism that occur in these systems, even in conditions where the turbulence is relatively moderate.

Chapters III and IV built upon the frameworks presented in Chap. II to build maximum *a posteriori* estimators for cases where the imaging system was considered spatially-invariant and spatially-variant respectively. Several sources of blur conspire to reduce high spatial frequency detail in the final detected image. For moderately turbulent conditions over long horizontal or slant paths, the atmospheric seeing condition, parameterized by Fried's seeing parameter r_0, becomes much more of a limiting system factor than the limits imposed by the physical aperture. Tip and tilt components of the atmospheric random phase delays cause significant blur due to linear translation in the orthogonal axes of the image. Fortunately, by the judicious use of robust registration algorithms, most if not all of this motion blur may be effectively removed from the resulting ensemble average image. A more difficult problem is encountered when attempting to remove the blur caused by the uncorrelated motion of the many isoplanatic sub-image patches that occur due to the shift-variant nature of wide FOV optical systems operating through even moderate levels of atmospheric turbulence. AO systems with multiple points of reference or "guide stars" are effective tools to estimate and deconvolve the spatially variant OTF that describe this process. The simpler approach described in Chap. IV provides a means to estimate the additional average blur created in the average image due to the spatially variant imaging system. Given such a parameterized model for anisoplanatic blur, the deconvolution

kernel of the MAP estimator presented in Chap. III is improved to better process imagery collected through a wide FOV system.

Chapter V explored the additional benefit gained in effective seeing condition enhancement by the selective removal of ensemble image frames from the averaged image introduced to the deconvolution algorithm. Although such processing introduces a bias in the estimation of the actual seeing condition parameter, the goal of obtaining higher spatial frequency content within the deconvolved image was attained. Identification and removal of suspect ensemble images is a convenient way to enhance imagery collected from a system with relatively high frame sample periods. As an example, a system with a moderately fast frame rate might discard 25 of 50 frames in an ensemble. If 50 frames are deemed necessary to satisfy image SNR requirements due to low photon counts resulting from long range imaging scenarios, an additional 50 frames might be collected during some acceptably short dwell period.

6.2 Research Contribution Summary

Several specific and significant research contributions result from the work discussed in this document. These contributions are intended for application to the field of coherent image restoration, but may be extended to the broader field of incoherent illumination in many circumstances.

6.2.1 Restoration of Remote Scene Imagery Illuminated by Partially Coherent Light. The accurate restoration of imagery captured by a partially coherent laser vision system is hampered by the speckle that is caused by the physical interaction of the illuminating beam with the target surface, as well as the speckle created by the random delays imposed by the turbulent atmosphere between the optical system and the target. The physically based propagation model of Chap. II provides a statistical means by which the detected intensity of a coherently illuminated target may be reconstructed via maximum likelihood estimation techniques. This research led to the development of such an estimator in Chap. III to jointly estimate the remote

scene together with the actual seeing conditions under which the scene was imaged, parameterized by r_0. The utility of such an estimator is quite general. In the limit as the speckle parameter is allowed to grow large, the imaging situation closely resembles incoherent imaging. In such cases, the blind deconvolution MAP estimation technique might allow the accurate estimation of atmospheric seeing conditions over long optical paths without the use of expensive scintillometry equipment or special illuminator sources. A simple experimental observation of a scene with sufficiently high spatial detail might be all that is required to yield accurate estimates of the composite horizontal or slant-path integrated turbulence between the target and optical system.

6.2.2 Anisoplanatic OTF Describing Wide FOV Imaging Systems. For wide FOV systems, the absolute level of turbulence typical of terrestrial operating scenarios causes highly anisoplanatic viewing conditions. The additional blur that arises due to the spatially variant OTF must be properly accounted for. The research of Chap. IV provided a concise and effective description of the quantitative effects of this type of optical degradation, and presented a compact model for the parameterization of these effects. When incorporated into the MAP blind deconvolution algorithm described initially in Chap. III, the model was found to better represent the true atmospheric conditions used to image the remote scene. The extension to anisoplanatic seeing conditions enhances the utility of a calibrated seeing condition estimator. For turbulence levels that cause wide FOV optical systems to exceed the isoplanatic angle, the monitor remains effective in presenting seeing condition estimates not appreciably biased by the introduction of spatially variant blur into the ensemble images collected by the system.

6.2.3 Seeing Condition Monitor. Although much of the motivation for the development of the algorithms presented in this research lies in the ability of the image restoration process to enhance spatial resolution and image detail, an important side-effect is the accurate estimation of the atmospheric conditions under which the

images were collected. A distinct contribution is made to those researchers who seek new methods to accurately estimate seeing conditions through a variety of different and evolving atmospheres. As an example, a compact seeing monitor may be constructed whereby a remote scene is illuminated by partially coherent light, and the techniques and algorithms described in Chapters III and IV are used to provide accurate estimates for Fried's seeing parameter. The new method is valuable due to non-reliance on particular target scenery, as might be required by competing systems. As will be discussed in Sec. 6.3.3, the estimation algorithms may be extended to process incoherently illuminated scenes, such as those illuminated by ambient light. Such extension is due to the generality of the model used to quantify the statistics of the detected light of the imaging device.

6.2.4 Outlier Detection and Binary Weighted Frame Averaging of Ensembles of Coherently Detected Imagery.   Chapter V introduced the utility of an algorithm that seeks improved spatial resolution by the automatic selection of particular frames within an ensemble of images collected through a random atmosphere. The sources of image corruption included the basic speckle mechanism described above, but also the random turbulence and mis-registration between images within the ensemble. Of course, such a system would tend to produce optimistically biased estimates of the seeing condition when employed as a seeing condition monitor, however, the system is of great value to communities that wish to regain high spatial frequency information from a series of averaged images. For example, given a laser vision system with sufficiently high frame rate, large numbers of speckle images may be collected over acceptably brief dwell periods. Under these circumstances, it may be more efficient to simply discard frames that are heavily corrupted by turbulence, or difficult to accurately register due to anisoplanatic warping, rather than spend inordinately large amounts of computing resources in an attempt to repair the corrupted images by using image de-warping techniques or alternate registration algorithms.

6.2.5 Speckle Parameter Estimator.   The application of the MAP estimation techniques discussed above rely on fairly accurate estimation of the laser speckle parameter $\mathcal{M}$ that characterizes the NB distribution of the detected image intensity. The speckle parameter is not fixed, and depends on complex relationships between the laser coherence time, the detector gating period, the amount of laser beam scintillation, and perhaps other variables that are difficult to measure directly. Accurate estimation of $\mathcal{M}$ as described in Sec. 2.5 provides an information theoretic approach to the calculation of the effective speckle parameter that parameterizes the random process assumed to govern the MAP estimators of Chapters III and IV.

6.2.6 Effects of Image Quantization and Scaling.   The effects of image intensity quantization and scaling were recognized in the early stages of this research and caused some difficulty in the interpretation of the simulated and measured results. Section 2.7 discussed the investigation and effects produced by these phenomena. Fielded image processing systems will likely involve compromises involving image quantization. In most cases, accurate image scaling must be performed to relate the recorded image intensities to the number of photons received. This relationship is important because the MAP estimators were constructed using statistical models of photon arrival at the detector. Without attention to image scaling and quantization, the measured data will not follow the expected statistics of the imaging system. This research presents the tools necessary by which the effects of image quantization and scaling may be understood in the context of coherent image restoration using MAP estimation, and raw image data may be accurately calibrated for introduction into these and similar algorithms.

6.3 Future Research Considerations

Although the research described in this document represents a fairly complete treatment of image restoration of partially coherent remote imagery, several research efforts might extend the utility of the described methods.

6.3.1 Speed Improvement of Blind Deconvolution Algorithm for Real-Time Applications. Although the blind deconvolution algorithm described in Chap. III converges fairly rapidly to approach the maximum likelihood estimate of the scene for a particular value of r_0, the space of values for r_0 is fairly large, requiring a search over the entire space. Due to the apparent monotonicity of the likelihood curve for each value of r_0, it may prove feasible to obtain a coarse estimate of the seeing condition using only several iterations at each value in r_0-space. The likelihood of the scene may then be maximized only for neighboring values of r_0.

Although this approach appears promising, a much faster algorithm might be realized if all calculations could be performed in the frequency domain, where convolutions are simply evaluated using circular convolution by way of fast-Fourier transform techniques. Referring to Eqn. 3.15, repeated here for convenience,

$$\mathbf{o}^{new}(r_0') = \mathbf{o}^{old}(r_0') \frac{\sum_{x=1}^{N} \sum_{y=1}^{N} \left(\frac{d(x,y)}{i^{old}(x,y)} \bar{h}_{sys}(x - \xi, y - \eta) \right)}{\sum_{x=1}^{N} \sum_{y=1}^{N} \left(\frac{d(x,y)+\mathcal{M}}{\mathcal{M}+i^{old}(x,y)} \bar{h}_{sys}(x - \xi, y - \eta) \right)},$$

it is clear that both the numerator and the denominator of the right-hand side may be evaluated using Fourier domain convolution. However, at each iteration step, the right-hand side fraction must be transformed back to the spatial domain in order to pointwise multiply by the previous scene estimate. This process requires the 2-dimensional Fourier transformation of a fairly large matrix. A more efficient implementation would be realized if the entire operation could be cast into the Fourier domain, with the requirement to return to the spatial domain only twice, at the initialization and end of the iterative process. However, the negative binomial statistics of the detected intensity presents a difficult analytical problem. A tempting approach would be to represent the negative binomial statistics into a more easily transformable distribution, such as the Gaussian PDF.

The study of Gaussian mixture models (GMM) provides a highly useful tool that has been applied to many statistical modeling applications [5]. GMMs allow the

fairly arbitrary representation of virtually any statistical distribution with one or more Gaussian basis functions. Since the Fourier operator is linear, the negative binomial statistics of the coherent photodetection process might be well approximated by some number of Gaussian basis functions, and easily recast into the Fourier domain to allow complete reconstruction of the image without alternating between both domains.

This course of research might lead to an extremely fast, reliable and robust algorithm with significant practical value to researchers and system designers requiring fast, accurate deconvolution of a wide range of coherently imaged, turbulence degraded wide FOV scene data.

6.3.2 Proof of Convergence of the Iterative Algorithms. A further benefit of the application of GMMs to this problem might yield a formulation of the deconvolution algorithm in light of the optimality of the expectation-maximization (EM) algorithm [5, 50]. Although the coherent blind deconvolution algorithm is derived in a maximum *a posteriori* framework, it has not been proven that the algorithm increases the likelihood as iterations progress, despite all indications that support this conclusion. One of the exciting properties of the application of the EM algorithm is that "it has proved to be a valuable tool for many problems, since it provides an elegant approach to bypass difficult optimization and integrations required in Bayesian estimation problems" [50]. The difficulty of applying the EM algorithm frequently occurs during the formulation of the E-step, where the conditional densities of the hidden variables must be determined. The transformation of statistics from negative binomial to Gaussian using GMMs may make such an approach tractable.

6.3.3 Extension to Incoherently Collected Imagery. The techniques described in the research may be extended from partially coherent to relatively incoherent illumination, as is encountered in the vast majority of imaging scenarios. The extension is a natural result of the degree-of-freedom introduced by the speckle parameter $\mathcal{M}$ in the negative binomial distribution that describes the photon count of partially coherent illumination at the imaging detector. As an example of a diverse

application of this research, smaller astronomical observatories might restore images of remote objects that are subject to the same ill effects of terrestrial objects when viewed through large aperture systems limited by the atmospheric coherence diameter. A common example is the observation of the Earth's Moon or the surface of the Sun. Both objects have relatively large angular extent and often require image restoration techniques that effectively cope with anisoplanatic imaging conditions. Automatic frame selection of such images provides further spatial detail that would otherwise be difficult to cull from a large set of speckle imagery. Although larger, better equipped observatories might have AO image enhancement capability, such systems often require a portion of the illumination to be used for wavefront estimation, thus reducing the final photon count at the imaging detector. In addition, the added expense and complexity of a full AO system might not be justified for smaller observatory missions.

6.3.4 Fusion of Imaging Correlography Information with Imaged Data.
Imaging correlography is an interesting field of research that seeks to reconstruct an image from the Fourier modulus of the fields collected at the aperture plane, without the requirement of focusing the field on an imaging detector array. Fienup and others have reported good results in the synthesis of images obtained by the coherent illumination of reflected laser-speckle intensitity patterns [36, 74].

As presented, the recovery of high-resolution images from the Fourier modulus collected at the aperture is a computationally intense process that requires many data frames to achieve suitably high SNR. However, the collection of only Fourier modulus data at the aperture discards phase-dominated atmospheric distortion as evidenced by the model presented in Sec. 2.3. A potential research avenue would be the exploration of the advantages of fusing these data with the imaged data collected by the detector behind the aperture lens. Since the Fourier modulus data are relatively unaffected by the phase-dominated turbulence variations, it is expected that high

frequency information available in the correlography data would complement the low-pass filtered data that results at the image plane due to the atmospheric turbulence.

The difficulty of this fusion effort lies in the ability to cast the coherent illumination statistics into the aperture domain. Since the negative binomial distribution applies only to the intensity detection at the imaging detector plane, this distribution is not necessarily valid at the aperture plane. As discussed in Sec. 6.3.1, the recast of the negative binomial distribution into the Fourier domain is not trivial. However, research might be conducted to arrive at a direct physical model of the statistics of the Fourier modulus of a scene illuminated by partially coherent light backscattered from a target scene. Armed with this statistic, the additional information would be added to the likelihood equation and maximized using a similar iterative blind deconvolution algorithm. It is expected that the fusion of the aperture derived correlography data with detected imagery will improve the MAP estimator algorithm performance.

6.4   Final Thoughts

Active illumination of remote targets using partially coherent laser illumination provides system designers unprecedented levels of operational freedom. Accurate restoration of the detected imagery is essential to the success of such systems. Although adaptive optics provide an attractive methodology by which imagery may be effectively enhanced, the fielding of robust, compact and reliable systems is still many years in the future. Image post-processing techniques provide an immediate solution to a difficult and rewarding problem. The techniques described in this research are presented as stepping stones toward the goal of realizing useful and robust image reconstruction systems for terrestrial imaging scenarios of interest to a diverse range of system operators.

Appendix A. Direct Solution of Frame Average Weights

T he iterative solution derived in Sec. 5.3.1 is computationally expensive for large ensembles of large images. Additionally, stopping criteria for the iterative algorithm is difficult to establish. For these reasons, a direct solution to the likelihood maximization process is attractive. However, direct maximization of Eqn. 5.5 appears mathematically intractable. An alternative solution is offered by taking several liberties with the underlying probability mass function. The derivation begins with several simplifying assumptions about the detected intensity distribution that admit Gaussian statistics rather than the negative binomial distribution of Eqn. 5.1. The Gaussian model provides a log-likelihood function that is easily maximized by the solution of a system of linear equations. Due to the construction of the likelihood function, it becomes apparent that the linear system provides a least-squares solution to the problem.

A.1 Maximizing the Likelihood of the Weighted Average Ensemble

Recall the log-likelihood equation developed using the negative binomial statistics of the detected intensity at the focal plane array,

$$
L\left(\mathbf{d}\right) = \sum_{j=1}^{J}\sum_{x=1}^{N}\sum_{y=1}^{N}\left\{\frac{\Gamma\left(d_j\left(x-\hat{\alpha}_j, y-\hat{\beta}_j\right)+\mathcal{M}\right)}{\Gamma\left(d_j\left(x-\hat{\alpha}_j, y-\hat{\beta}_j\right)+1\right)\Gamma\left(\mathcal{M}\right)}\right.
$$
$$
\left. - d_j\left(x-\hat{\alpha}_j, y-\hat{\beta}_j\right)\ln\left[1+\frac{\mathcal{M}}{i\left(x,y\right)}\right] -\mathcal{M}\ln\left[1+\frac{i\left(x,y\right)}{\mathcal{M}}\right]\right\}. \quad \text{(A.1)}
$$

where the mean intensity $i(x,y)$ is formed by

$$
i\left(x,y\right) = \frac{1}{J}\sum_{n=1}^{J} A_n d_n\left(x-\hat{\alpha}_n, y-\hat{\beta}_n\right). \quad \text{(A.2)}
$$

Maximization of the likelihood is taken with respect to the individual frame weights A_n, $n = 1, 2, ..., J$ where J is the total number of frames in the ensemble. The maximization is difficult due to the combination of $i(x,y)$ and $\mathcal{M}$ in the logarithms of the second and third terms of Eqn. A.1. On possible approach is to assume

A-1

$\mathcal{M}$ small compared to $i(x,y)$ in order to simplify the likelihood function. Unfortunately, such an approximation is not well justified from a systems approach, and still yields an expression with a large summation within the logarithm due to the relationship of Eqn. A.2. A more practical approach may be undertaken by returning to the negative binomial distribution of Eqn. 5.1. Under conditions where the speckle parameter is fairly high, for example, $\mathcal{M} = 50$ or more, the negative binomial distribution approaches that of a Poisson distribution, as illustrated in Fig. 2.6. Under moderately high photon count conditions, the Poisson distribution is well approximated by a Gaussian distribution, although the latter admits the non-physical possibility of negative intensity values under low photon conditions. Using such an approximation, the probability of a pixel of the image data given a pixel of the average intensity may be expressed as

$$P_{d(x,y)|i(x,y)}\left(d\left(x,y\right)|i\left(x,y\right)\right) = \frac{1}{\sqrt{2\pi}\sigma}\exp\left(-\frac{\left(d_j\left(x-\hat{\alpha}_j,y-\hat{\beta}_j\right)-i\left(x,y\right)\right)^2}{2\sigma^2}\right), \quad \text{(A.3)}$$

where σ is the unspecified standard deviation of the noise process, and the mean of the Gaussian distribution is simply the mean intensity formed by the weighted average according to Eqn. A.2 with undetermined weight vector $\vec{A}$.

For a particular image in the J frame ensemble, the probability of a detected image given the weighted frame average is

$$P_{\mathbf{d}|i}(\mathbf{d}|i) = \prod_{x=1}^{N}\prod_{y=1}^{N}\frac{1}{\sqrt{2\pi}\sigma}\exp\left(-\frac{\left(d_j\left(x-\hat{\alpha}_j,y-\hat{\beta}_j\right)-i\left(x,y\right)\right)^2}{2\sigma^2}\right), \quad \text{(A.4)}$$

and by assumption of independence between image frames within the ensemble, the probability distribution for the entire ensemble becomes

$$P_{\mathbf{d}|i}(\mathbf{d}|i) = \prod_{j=1}^{J}\prod_{x=1}^{N}\prod_{y=1}^{N}\frac{1}{\sqrt{2\pi}\sigma}\exp\left(-\frac{\left(d_j\left(x-\hat{\alpha}_j,y-\hat{\beta}_j\right)-i\left(x,y\right)\right)^2}{2\sigma^2}\right), \quad \text{(A.5)}$$

where $\mathbf{d}$ represents the ensemble of detected images.

Maximization of the log-likelihood is mathematically convenient, and Eqn. A.5 may be expressed in logarithmic format as

$$L_g\left(\mathbf{d}\right) = \sum_{j=1}^{J}\sum_{x=1}^{N}\sum_{y=1}^{N}\left\{-\ln\left(\sqrt{2\pi}\sigma\right) - \frac{\left(d_j\left(x-\hat{\alpha}_j, y-\hat{\beta}_j\right) - i\left(x,y\right)\right)^2}{2\sigma^2}\right\}. \quad \text{(A.6)}$$

Since each maximization of Eqn. A.6 must be calculated with respect to an arbitrary frame weight A_{j_0}, the first term within the summation may be disregarded and a new log-likelihood may be written as

$$\tilde{L}_g\left(\mathbf{d}\right) = \sum_{j=1}^{J}\sum_{x=1}^{N}\sum_{y=1}^{N}\left\{-\frac{\left(d_j\left(x-\hat{\alpha}_j, y-\hat{\beta}_j\right) - i\left(x,y\right)\right)^2}{2\sigma^2}\right\}. \quad \text{(A.7)}$$

To maximize this expression, the derivative with respect to A_{j_0} may be calculated and set to zero. As derived in Sec. 5.3.1, the derivative of the weighted intensity with respect to an arbitrary weight in the ensemble can be expressed as

$$i'(x,y) = \frac{d}{dA_{j_0}}i\left(x,y\right) = \frac{1}{J}d_{j_0}\left(x-\alpha_{j_0}, y-\beta_{j_0}\right), \quad \text{(A.8)}$$

which allows differentiation of Eqn. A.7 to yield

$$\frac{d\tilde{L}_g\left(\mathbf{d}\right)}{dA_{j_0}} = -\sum_{j=1}^{J}\sum_{x=1}^{N}\sum_{y=1}^{N}\left\{\frac{1}{J\sigma^2}\left[d_j\left(x-\hat{\alpha}_j, y-\hat{\beta}_j\right) - i\left(x,y\right)\right]d_{j_0}\left(x-\hat{\alpha}_{j_0}, y-\hat{\beta}_{j_0}\right)\right\}. \quad \text{(A.9)}$$

By setting the derivative to zero and rearranging the order of summation,

$$\sum_{x=1}^{N}\sum_{y=1}^{N}\sum_{j=1}^{J}d_j\left(x-\hat{\alpha}_j, y-\hat{\beta}_j\right)d_{j_0}\left(x-\hat{\alpha}_{j_0}, y-\hat{\beta}_{j_0}\right) = \sum_{x=1}^{N}\sum_{y=1}^{N}\sum_{j=1}^{J}i\left(x,y\right)d_{j_0}\left(x-\hat{\alpha}_{j_0}, y-\hat{\beta}_{j_0}\right), \quad \text{(A.10)}$$

and since $d_{j_0}\left(x - \hat{\alpha}_{j_0}, y - \hat{\beta}_{j_0}\right)$ is not a function of j in the ensemble summation, the relationship may be rewritten as

$$\sum_{x=1}^{N}\sum_{y=1}^{N}\left[d_{j_0}\left(x - \hat{\alpha}_{j_0}, y - \hat{\beta}_{j_0}\right)\sum_{j=1}^{J}d_j\left(x - \hat{\alpha}_j, y - \hat{\beta}_j\right)\right] = \sum_{x=1}^{N}\sum_{y=1}^{N}\left[d_{j_0}\left(x - \hat{\alpha}_{j_0}, y - \hat{\beta}_{j_0}\right)\sum_{j=1}^{J}i\left(x, y\right)\right]. \quad \text{(A.11)}$$

Although Eqn. A.11 appears to be an unlikely candidate for direct solution, expressing the relationship as a system of linear equations for each particular image frame in the ensemble admits solution by way of linear algebra techniques. The left-hand-side of Eqn. A.11 is constant given a particular choice for the frame under consideration, d_{j_0}. Let this constant be C_{j_0},

$$C_{j_0} = \sum_{x=1}^{N}\sum_{y=1}^{N}\left[d_{j_0}\left(x - \hat{\alpha}_{j_0}, y - \hat{\beta}_{j_0}\right)\sum_{j=1}^{J}d_j\left(x - \hat{\alpha}_j, y - \hat{\beta}_j\right)\right]. \quad \text{(A.12)}$$

The expression for the weighted average intensity of Eqn. A.2 may be substituted into the right-hand-side of Eqn. A.11 to yield

$$C_{j_0} = \sum_{x=1}^{N}\sum_{y=1}^{N}\left[d_{j_0}\left(x - \hat{\alpha}_{j_0}, y - \hat{\beta}_{j_0}\right)\sum_{j=1}^{J}\frac{1}{J}\sum_{n=1}^{J}A_n d_n\left(x - \hat{\alpha}_n, y - \hat{\beta}_n\right)\right], \quad \text{(A.13)}$$

or equivalently,

$$C_{j_0} = \sum_{j=1}^{J}A_j\sum_{x=1}^{N}\sum_{y=1}^{N}\left[d_{j_0}\left(x - \hat{\alpha}_{j_0}, y - \hat{\beta}_{j_0}\right)d_j\left(x - \hat{\alpha}_j, y - \hat{\beta}_j\right)\right]. \quad \text{(A.14)}$$

Let the double summation over x and y of Eqn. A.14 represent a vector of coefficients $\vec{K}_{j_0}$ for each image frame in the ensemble d_j. Under this framework, the linear equation for a particular frame d_{j_0} can be written as

$$C_{j_0} = \sum_{j=1}^{J}A_j K_{j_0,j} \quad \text{(A.15)}$$

.

The entire set of coefficients for all frames in the the ensemble may be compactly described by a square $J \times J$ matrix $\mathbf{K}$, where each row holds a vector of such coefficients for each selected image in the ensemble. Thus

$$K_{a,b} = \sum_{x=1}^{N} \sum_{y=1}^{N} \left[d_a \left(x - \hat{\alpha}_a, y - \hat{\beta}_a \right) d_b \left(x - \hat{\alpha}_b, y - \hat{\beta}_b \right) \right], \qquad \text{(A.16)}$$

where a indexes the row position, and b indexes the column position of the matrix $\mathbf{K}$. In effect, $\mathbf{K}$ is analogous to a correlation matrix formed by the pointwise multiplication of each frame in the ensemble with every other frame in the ensemble. Unlike a correlation matrix, however, $\mathbf{K}$ is not normalized.

Under this representation, Eqn. A.11 may be expressed using vector notation as $\vec{C} = \mathbf{K}\vec{A}$ where $\vec{A}$ and $\vec{C}$ are J element vectors. If $\mathbf{K}$ is invertible, then the direct solution to the frame weights may be found using the relationship $\vec{A} = \mathbf{K}^{-1}\vec{C}$. The random variation of the images in the ensemble permit the inversion of $\mathbf{K}$. With little or no variation between each image in the ensemble, the rank of $\mathbf{K}$ would clearly be less than J. Low variance between imagery will increase the matrix condition and cause difficulty in the inversion process. However, for realistic imaging scenarios, the elevated image variance will increase the rank of $\mathbf{K}$ to J. Furthermore, the element of $\mathbf{K}$ are always positive due to the physical detection of the photon intensity, and the matrix is real symmetric. Under these conditions, a unique solution for the weights may be determined by calculation of $\vec{A} = \mathbf{K}^{-1}\vec{C}$ using Equations. A.12 and A.16.

A.2 Implementation of the Direct Solution

The direct solution provided by the analysis of Sec. A.1 minimizes the square error between the weighted average intensity and the ensemble imagery. It is not clear that such an estimator for the weights of the frame imagery should improve the resolution of the estimated average image by increasing the high spatial frequency content. In practice, it was found that despite the invertibility of the coefficient matrix $\mathbf{K}$, the weights calculated using $\vec{A} = \mathbf{K}^{-1}\vec{C}$ had only minor effect on the weights applied

to the ensemble imagery. Several simulated and experimental datasets were analyzed using the direct approach, however, the resulting weighed average images did not substantially differ from the unweighted imagery in terms of spatial frequency content or resolution. While the direct solution is slightly less computationally involved in comparison to the binary frame weighting technique discussed in Chap. V, the lack of image improvement suggests that the application of a least-squares solution lacks significant merit when applied to this particular problem.

Bibliography

1. Andrews, L. C. *Field Guide to Atmospheric Optics*. Washington DC: SPIE Press, 2004.

2. Ayers, G. R. "Iterative Blind Deconvolution Method and its Applications," *Optics Letters*, *13*(7):547–549 (July 1988).

3. Belen'kii, M. S. "Tilt angular anisoplanatism and a full-aperture tilt-measurement technique with a laser guide star," *Applied Optics*, *39*(33):6097–6108 (November 2000).

4. Biggs, D. S. and Andrews, M. "Asymmetric Iterative Blind Deconvolution of Multiframe Images." *SPIE Conference on Advanced Signal Processing Algorithms, Architectures and Implementations VIII 3461*. July 1998.

5. Bishop, C. M. *Neural Networks for Pattern Recognition*. New York, NY: Oxford University Press, Inc., 1995.

6. Bondeau, C., Bourennane, E., and Paindavoine, M. "Restoration of a Short-Exposure Image Sequence Degraded by Atmospheric Turbulence." *SPIE Conference on Propagation and Imaging through the Atmosphere IV 4125*. July 2000.

7. Cain, S. C., Hayat, M. M., and Armstrong, E. A. "Projection-based image registration in the presence of fixed-pattern noise," *IEEE Transactions on Image Processing*, *10*(12):1860–1872 (December 2001).

8. Cain, S. C. "Three-dimensional laser radar sensor modeling and validation via a monte-carlo Rayleigh-Sommerfeld wave optics approach." *SPIE Conference on Laser Radar Technology and Applications IX 5412*. 360–368. September 2004.

9. Carrano, C. J. "Anisoplanatic Performance of Horizontal-Path Speckle Imaging." *SPIE Conference on Advanced Wavefront Control: Methods, Devices, and Applications 5162*. December 2003.

10. Castleman, K. R. *Digital Image Processing*. Englewood Cliffs, NJ: Prentice Hall, Inc., 1996.

11. Chan, C. L. and Katsaggelos, A. K. "Iterative Maximum Likelihood Displacement Field Estimation in Quantum-Limited Image Sequences," *IEEE Transactions on Image Processing*, *4*(6):743–751 (June 1995).

12. Charnotskii, M., Myakinin, V., and Zavorotnyy, V. "Observation of Superresolution in Nonisoplanatic Imaging through Turbulence," *Journal of the Optical Society of America, A.*, *7*(8):1345–1350 (August 1990).

13. Chen, L. and Yap, K.-H. "Identification of Blur Support Size in Blind Image Deconvolution." *IEEE Joint Conference of the Fourth International Conference*

7

on Information, Communications and Signal Processing 1. 503–507. December 2003.

14. Christou, J. C., Jefferies, S. M., and Hege, E. K. "Object Independent Point Spread Function and Waveforn Phase Estimation." *SPIE Conference on Adaptive Optics Systems and Technology 3762*. July 1999.

15. Clyde, D., Fleming, I. S., and Lambert, A. "Application of Optical Flow Techniques in the Restoration of Non-uniformly Warped Images." *IEE Conference on Digital Image Computing - Techniques and Applications 7677220*. January 2002.

16. Conover, W. J. *Practical Nonparametric Statistics*. New York, NY: John Wiley and Sons, Inc., 1971.

17. Costa, W. L. S., Haynor, D. R., Haralick, R. M., Lewellen, T. K., and Graham, M. M. "A Maximum-Likelihood Approach to PET Emission/Attenuation Image Registration." *IEEE Nuclear Science Symposium and Medical Imaging Conference*. 1139–1143. October 1993.

18. Dainty, J. C. *Laser Speckle*. New York, NY: Springer-Verlag, 1975.

19. Dayton, D., Brownea, S., Gonglewski, J., Sandven, S., Gallegos, J., and Shilko, M. "Long-range laser illuminated imaging: analysis and experimental demonstrations," *Optical Engineering*, *40*(6):1001–1009 (June 1996).

20. Dayton, D. and Gonglewski, J. "Deconvolution from Wavefron Sensing Enhanced with Blind Deconvolution." *SPIE Conference on Optics in Atmospheric Propagation, Adaptive Systems, and Lidar Techniques for Remote Sensing 2956*. 218–226. Jan 1997.

21. Fish, D., Brinicombe, A., and Pike, E. "Blind Deconvolution by means of the Richardson-Lucy Algorithm," *Journal of the Optical Society of America*, *12*(1):58–65 (January 1995).

22. Ford, S. D., Roggemann, M. C., and Welsh, B. M. "Frame Selection Performance Limits for Statistical Image Reconstruction of Adaptive Optics Compensated Images," *Optical Engineering*, *35*(4):1025–1034 (April 1996).

23. Fraser, D., Thrope, G., and Lambert, A. "Atmospheric Turbulence Visualization with Wide-Area Motion-Blur Restoration," *Journal of the Optical Society of America*, *16*(7):1751–1758 (July 1999).

24. Fried, D. "Analysis of the CLEAN Algorithm and Implications for Superresolution," *Journal of the Optical Society of America, A*, *12*:853–860 (November 1995).

25. Fried, D. L. "Probability of Getting a Lucky short-exposure Image Through Turbulence," *Journal of the Optical Society of America, A*, *68*(12):1651–1658 (December 1978).

26. Gardner, C. S., Welsh, B. M., and Thompson, L. A. "Design and performance analysis of adaptive optical telescopes using laser guide stars." *Proceedings of the IEEE 78*. 1721–1743. November 1990.

27. Geiger, D. and Pereira, R. A. M. "The Outlier process." *IEEE Workshop Proceedings: Neural Networks for Signal Processing*. 60–69. October 1991.

28. Gerwe, D. R., Lee, D. J., and Barchers, J. D. "Supersampling Multiframe Blind Deconvolution Resolution Enhancement of Adaptive Optics Compensated Imagery of Low Earth Orbit Satellites," *Optical Engineering*, *41*(9):2238–2251 (September 2002).

29. Gerwe, D. and Plonus, M. "Superresolved Image Reconstruction of Images taken through the Turbulent Atmosphere," *Journal of the Optical Society of America, A.*, *15*(10):2620–2628 (October 1998).

30. Goodman, J. W. *Introduction to Fourier Optics*. New York, NY: McGraw-Hill, Inc., 1968.

31. Goodman, J. W. *Statistical Optics*. New York, NY: John Wiley and Sons, Inc., 1985.

32. Hardie, R., Barnard, K. J., and Armstrong, E. E. "Joint MAP Registration and High-Resolution Image Estimation using a Sequence of Undersampled Images," *IEEE Transactions on Image Processing*, *6*(12):1621–1633 (December 1997).

33. Hardy, J. W. *Adaptive Optics for Astronomical Telescopes*. New York, NY: Oxford University Press, Inc., 1998.

34. Hasler, D., Sbaiz, L., Susstrunk, S., and Vetterli, M. "Outlier Modeling in Image Matching," *IEEE Transactions on Pattern Analysis and Machine Intelligence*, *25*(3):301–315 (March 2003).

35. Herman, B. J. and Strugala, L. A. "Method for inclusion of low-frequency contributions in numerical representation of atmospheric turbulence." *SPIE Conference on Propagation of High-Energy Laser Beams Through the Earth's Atmosphere 1221*. 183–192. May 1990.

36. Idell, P. S., Fienup, J., and Goodman, R. S. "Image Synthesis from Nonimaged Laser-Speckle Pattern," *Optics Letters*, *12*(11):858–860 (November 1987).

37. Jefferies, S. M., Schulze, K. J., Matson, C. L., Hege, E. K., and Stoltenberg, K. "Imaging Through Turbid Media: Post Processing using Blind Deconvolution." *SPIE Conference on Multifrequency Electronic/Photonic Devices and Systems for Dual-Use Applications 4490*. 282–289. 2001.

38. Johansson, E. M. and Gavel, D. T. "Simulation of stellar speckle imaging." *SPIE Conference on Amplitude and Intensity Spatial Interferometry II 2200*. 372–383. June 1994.

39. Kim, J. and Fessler, J. A. "Intensity-Based Image Registration Using Robust Correlation Coefficients," *IEEE Transactions on Medical Imaging*, *23*(11):1430–1444 (November 2004).

40. Kopeika, N. S. *A System Engineering Approach to Imaging*. Bellingham, WA: SPIE Optical Engineering Press, 1998.

41. Kundur, D. and Hatzinakos, D. "Blind Image Deconvolution," *IEEE Signal Processing Magazine*, *13*(3):43–64 (May 1996).

42. Kundur, D. and Hatzinakos, D. "Blind Image Deconvolution Revisited," *IEEE Signal Processing Magazine*, *13*(6):61–63 (November 1996).

43. Lam, E. Y. and Goodman, J. W. "Iterative Blind Image Deconvolution in space and Frequency Domains." *IST/SPIE Conference on Sensors, Cameras, and Applications for Digital Photography 3650*. January 1999.

44. Lambert, A. and Fraser, D. "Super-Resolution in Imagery Arising from Observation through Anisoplanatic Distortion." *SPIE Conference on Image Reconstruction from Incomplete Data II 5562*. July 2002.

45. Lambert, A., Fraser, D., Jahromi, M. R. S., and Hunt, B. "Super-Resolution in Image Restoration of Wide Area Images Viewed Through Atmospheric Turbulence." *SPIE Conference on Image Reconstruction from Incomplete Data II 4792*. July 2002.

46. Lane, R. "Blind Deconvolution of Speckle Images," *Journal of the Optical Society of America*, *9*(9):1508–1514 (September 2002).

47. Lapp, H., Zumrick, R., Mikula, C., and Kile, F. "Advances in Gated Laser Imaging using a Electron-Bombarded Charge-Coupled Device Camera - Update and Plans." Air Force Research Laboratories AFRL/SNJT Internal Report, August 2001.

48. Leung, W.-Y., Clare, R., and Lane, R. "Blind Deconvolution of Speckle Images Constrained by Wavefront Sensing Data." *SPIE Conference on Image Reconstruction from Incomplete Data II 4792*. July 2002.

49. Leung, W.-Y. and Lane, R. "Blind Deconvolution of Images Blurred by Atmospheric Speckle." *SPIE Conference on Image Reconstruction from Incomplete Data 4123*. July 2000.

50. Likas, A. C. and Galatsanos, N. P. "A Variational Approach for Bayseian Blind Image Deconvolution," *IEEE Transactions on Signal Processing*, *52*(8):2222–2233 (August 2004).

51. Lofdahl, M. G. "Multi-Frame Blind Deconvolution with Linear Equality Constraints." *SPIE Conference on Image Reconstruction from Incomplete Data II 4792*. July 2002.

52. MacDonald, A. and Cain, S. C. "Derivation and application of an anisoplanatic optical transfer function for blind deconvolution for laser radar imagery." *SPIE Conference on Unconventional Imaging 5896*. September 2005.

53. MacDonald, A., Cain, S. C., and Armstrong, E. E. "Comparison of registration techniques for speckle suppression in 2-D LIDAR image sequences." *SPIE Conference on Image Reconstruction from Incomplete Data III 5558*. 202–213. November 2004.

54. MacDonald, A., Cain, S. C., and Armstrong, E. E. "Image Restoration Techniques for Partially Coherent 2-D ladar Imaging Systems." *SPIE Conference on Image Reconstruction from Incomplete Data III 5562*. 10–18. November 2004.

55. Magee, E. P., Whiteley, M. R., Das, S. T., and Welsh, B. M. "Tilt anisoplanatism in extended turbulence propagation." *SPIE Conference on Atmospheric Propagation 4976*. 13–21. April 2003.

56. Matson, C. L., Schulze, K. J., Billings, P., and Tyler, D. W. "Multi-Frame Blind Deconvolution and Bispectrum Processing of Atmospherically-Degraded Data: a Comparison." *SPIE Conference on Image Reconstruction from Incomplete Data II 4792*. July 2002.

57. Richardson, B. "Bayesian-Based Iterative Method of Image Restoration," *Journal of the Optical Society of America*, *62*:55–59 (August 1972).

58. Robinson, D. and Milanfar, P. "Fundamental Performance Limits in Image Registration," *IEEE Transactions on Image Processing*, *13*(9):1185–1199 (September 2004).

59. Roggemann, M. C., Stoudt, C. A., and Welsh, B. M. "Image-Spectrum Signal-to-Noise-Ratio Improvements by Statistical Frame Selection for Adaptive-Optics Imaging Through Turbulence," *Optical Engineering*, *33*(10):3254–3263 (October 1994).

60. Roggemann, M. C. and Welsh, B. *Imaging Through Turbulence*. Boca Raton, FL: CRC Press, Inc., 1996.

61. Roggemann, M. C., Welsh, B. M., and Klein, T. L. "Algorithm to Reduce Anisoplanatism Effects on Infrared Images." *SPIE Conference on Propagation and Imaging through the Atmosphere IV 4125*. July 2000.

62. Sabo, D. R. and Cain, S. C. "Registration techniques for speckle suppression in 2-D LIDAR image sequences." *SPIE Conference on Algorithms and Systems IV 5672*. 82–93. March 2005.

63. Sasiela, R. J. *Electromagnetic Wave Propagation in Turbulence*. New York, NY: Springer-Verlag, 1994.

64. Schulz, T. J. "Multiframe Blind Deconvolution of Astronomical Images," *Journal of the Optical Society of America*, *10*(5):1064–1073 (May 1993).

65. Seldin, J. and Fienup, J. "Iterative Blind Deconvolution Algorithm Applied to Phase Retreival," *Journal of the Optical Society of America*, *7*(3):428–433 (March 1990).

66. Shan, Z. and Zhenkang, S. "Blind Deconvolution of Infrared Image." *SPIE Conference on Multispectral and Hyperspectral Image Acquistition and Processing4548*. July 2001.

67. Sheppard, D., Hynt, B., and Marcellin, M. W. "Super-Resolution of Imagery Acquired through Turbulent Atmosphere." *IEEE Conference Record of the Thirtieth Asilomar Conference on Signals, Systems and Computers1*. November 1996.

68. Sheppard, D., Hynt, B., and Marcellin, M. W. "Super-Resolution of Imagery Acquired through Turbulent Atmosphere." *IEEE Conference Record of the Thirty-Second Asilomar Conference on Signals, Systems and Computers2*. November 1998.

69. T.Fusco, , Conan, J. M., Mugnier, L. M., Michau, V., and Rousset, G. "Post-processing for anisoplanatic AO corrected images." *SPIE Conference on Propagation and Imaging through the Atmosphere IV 4125*. 108–119. September 2000.

70. Thelen, B. J., Carrara, D. A., and Paxman, R. G. "Fine-Resolution Imagery of Extended Objects Observed Through Volume Turbulence using Phase-Diverse Speckle." *SPIE Conference on Propagation and Imaging through the Atmosphere III 3763*. July 1999.

71. Trees, H. L. V. *Detection, Estimation and Modulation Theory*. New York, NY: John Wiley and Sons, Inc., 2001.

72. Valley, G. C. "Isoplanatic degradation of tilt correction and short-term imagaing systems," *Applied Optics*, *19*(4):574–577 (February 1980).

73. van Kampen, W. and Paxman, R. "Multi-Frame Blind Deconvolution of Infinite-Extent Objects." *SPIE Conference on Propagation and Imaging through the Atmosphere II 3433*. 296–307. July 1998.

74. Voelz, D. G., Gonglewski, J. D., and Idell, P. S. "Image Synthesis from Nonimaged Laser-Speckle Patterns: Comparison of Theory, Computer Simulation, and Laboratory Results," *Applied Optics*, *30*(23):3333–3344 (August 1991).

75. Vorontsov, M. A. and Carhart, G. W. "Anisoplanatic Imaging through Turbulent Media: Image Recovery by Local Information Fusion from a Set of Short-Exposure Images," *Journal of the Optical Society of America*, *18*(6):1312–1324 (June 2001).

76. Vural, C. and Sethares, W. A. "Blind Deconvolution of Noisy Blurred Images via Dispersion Minimization," *IEEE Signal Processing Magazine*, *2*(2):787–790 (July 2002).

77. Welsh, B. M. and hester S. Gardner, . "Effects of Turbulence-Induced Anisoplanatism on the Imaging Performance fo Adaptive-Astronomical Telescopes using

Laser Guide Stars," *Journal of the Optical Society of America*, *8*(1):69–80 (January 1991).

78. Wernick, M. N. and Morris, G. M. "Effect of spatial coherence on knife-edge measurements of detector modulation transfer function," *Applied Optics*, *33*(25):5906–5913 (September 1994).

79. Whitely, M., Magee, E., and Roggemann, M. *Tracking Through Laser-Induced Clutter for Air-to-Ground Directed Energy Systems*. Final Report AFRL-DE-TR-2003-1056, 3975 Research Boulevard, Dayton, OH 45430-2108: Mission Research Corporation, June 2003.

80. Wolfe, W. L. *The Infrared Handbook*. Washington DC: Environmental Research Institute of Michigan, 1993.

81. Woods, N. A., Galatsanos, N. P., and Katsaggelos, A. K. "EM-Based Simultaneous Registration, Restoration and Interpolation of Super-Resolved images." *International Conference on Image Processing (ICIP 2003)3*. 303–306. September 2003.

82. Zhu, Z.-M. and Cochoff, S. M. "Likelihood Maximization Approach to Image Registration," *IEEE Transactions on Image Processing*, *11*(12):1417–1426 (December 2002).

REPORT DOCUMENTATION PAGE

Form Approved
OMB No. 0704–0188

1. REPORT DATE *(DD–MM–YYYY)*	2. REPORT TYPE	3. DATES COVERED *(From — To)*
01–06–2006	Doctoral Dissertation	Sept 2004 — Jun 2006

4. TITLE AND SUBTITLE

Blind Deconvolution of Anisoplanatic Images
Collected by a Partially Coherent Imaging System

5a. CONTRACT NUMBER

5b. GRANT NUMBER

5c. PROGRAM ELEMENT NUMBER

6. AUTHOR(S)

MacDonald, Adam, Lt Col, USAF

5d. PROJECT NUMBER

ENG06355

5e. TASK NUMBER

5f. WORK UNIT NUMBER

7. PERFORMING ORGANIZATION NAME(S) AND ADDRESS(ES)

Air Force Institute of Technology
Graduate School of Engineering and Management AFIT/EN
2950 Hobson Way, Building 640
WPAFB OH 45433-7765

8. PERFORMING ORGANIZATION REPORT NUMBER

AFIT/DS/ENG/06-04

9. SPONSORING / MONITORING AGENCY NAME(S) AND ADDRESS(ES)

Air Force Research Laboratory, Sensors Division
Dr. Edward A. Watson AFRL/SNJ, 255-7859 x4030
2241 Avionics Circle, Building 620
Wright-Patterson Air Force Base, OH 45433

10. SPONSOR/MONITOR'S ACRONYM(S)

AFRL/SNJ

11. SPONSOR/MONITOR'S REPORT NUMBER(S)

12. DISTRIBUTION / AVAILABILITY STATEMENT

Approved for public release; distribution unlimited

13. SUPPLEMENTARY NOTES

14. ABSTRACT

Coherent imaging systems offer unique benefits to system operators in terms of resolving power, range gating, selective illumination and utility for applications where passively illuminated targets have limited emissivity or reflectivity. This research proposes a novel blind deconvolution algorithm that is based on a maximum *a posteriori* Bayesian estimator constructed upon a physically based statistical model for the intensity of the partially coherent light at the imaging detector. The estimator is initially constructed using a shift-invariant system model, and is later extended to the case of a shift-variant optical system by the addition of a transfer function term that quantifies optical blur for wide fields-of-view and atmospheric conditions. The estimators are evaluated using both synthetically generated imagery, as well as experimentally collected image data from an outdoor optical range. The research is extended to consider the effects of weighted frame averaging for the individual short-exposure frames collected by the imaging system. It was found that binary weighting of ensemble frames significantly increases spatial resolution.

15. SUBJECT TERMS

blind deconvolution, image restoration, LIDAR, LADAR, laser radar, anisoplanatic, weighted frame averaging

16. SECURITY CLASSIFICATION OF:

a. REPORT	b. ABSTRACT	c. THIS PAGE
U	U	U

17. LIMITATION OF ABSTRACT

UU

18. NUMBER OF PAGES

170

19a. NAME OF RESPONSIBLE PERSON
Dr. Stephen C. Cain, Civ, USAF (ENG)

19b. TELEPHONE NUMBER *(include area code)*
(937) 255–3636, ext 4716

Standard Form 298 (Rev. 8–98)
Prescribed by ANSI Std. Z39.18